University of Alberta

Bench-top Megavoltage Computed Tomography Scanner with Cadmium Tungstate - Photodiode Detectors

By

Deluan Tu ©

A thesis submitted to the Faculty of Graduate Studies and Research in Partial fulfillment of the requirement for the degree of Master of Science

in

Medical Physics

Department of Physics

Edmonton, Alberta

Fall 2005

Library and
Archives Canada

Published Heritage
Branch

395 Wellington Street
Ottawa ON K1A 0N4
Canada

Bibliothèque et
Archives Canada

Direction du
Patrimoine de l'édition

395, rue Wellington
Ottawa ON K1A 0N4
Canada

Your file Votre référence
ISBN: 0-494-09304-8
Our file Notre référence
ISBN: 0-494-09304-8

NOTICE:
The author has granted a non-exclusive license allowing Library and Archives Canada to reproduce, publish, archive, preserve, conserve, communicate to the public by telecommunication or on the Internet, loan, distribute and sell theses worldwide, for commercial or non-commercial purposes, in microform, paper, electronic and/or any other formats.

The author retains copyright ownership and moral rights in this thesis. Neither the thesis nor substantial extracts from it may be printed or otherwise reproduced without the author's permission.

AVIS:
L'auteur a accordé une licence non exclusive permettant à la Bibliothèque et Archives Canada de reproduire, publier, archiver, sauvegarder, conserver, transmettre au public par télécommunication ou par l'Internet, prêter, distribuer et vendre des thèses partout dans le monde, à des fins commerciales ou autres, sur support microforme, papier, électronique et/ou autres formats.

L'auteur conserve la propriété du droit d'auteur et des droits moraux qui protège cette thèse. Ni la thèse ni des extraits substantiels de celle-ci ne doivent être imprimés ou autrement reproduits sans son autorisation.

In compliance with the Canadian Privacy Act some supporting forms may have been removed from this thesis.

While these forms may be included in the document page count, their removal does not represent any loss of content from the thesis.

Conformément à la loi canadienne sur la protection de la vie privée, quelques formulaires secondaires ont été enlevés de cette thèse.

Bien que ces formulaires aient inclus dans la pagination, il n'y aura aucun contenu manquant.

Canada

Reproduced with permission of the copyright owner. Further reproduction prohibited without permission.

To my Family

Abstract

A bench-top MVCT scanner with $CdWO_4$-photodiode detectors was designed and fabricated. The detector is composed of an array of eighty $CdWO_4$ crystals in contact with photodiodes. The linear response and imaging characteristics of the detector system were investigated. The detector's response with respect to dose rate was found to be linear. A small amount of spectral hardening was observed in the attenuation measurements of a 6 MV beam through solid water. The imaging characteristics include the frequency dependent modulation transfer function, MTF (f), noise power spectrum, NPS (f), and detective quantum efficiency, DQE (f). The DQE (f) is 21% at zero frequency in a 6 MV beam. The ability of the experimental system to collect the fan-beam sinogram data was demonstrated. For a 2 cGy radiation dose in a Co^{60} beam, small targets at 1.5% contrast level can be visualized in the reconstructed image.

Acknowledgements

I would like to thank all people who have helped me during my studies at the University of Alberta. First of all, I would like to thank my supervisor, Dr. S. Rathee, for his kindness, patience, and knowledge in guiding me during the entire project; for his hard work in helping me to solve any problems risen up during the research; for his allowing me have the opportunity to participate in this project, which turned out to be very interesting and rewarding; and for his careful editing my thesis, which turned out to be a difficult job. Without his help, this project would not have been possible.

I would also like to thank my committee -- Dr. Fallone, Dr. Hooper, and Dr. Moore for their advice. Special thanks to Dr. Fallone for being one of my advisors, for giving me the freedom to chose this project, and for his leadership that made to make this Medical Physics program an excellent one.

I would also like to thank Gary in the machine shop for building the detector and Mux boxes and the translate stage. I thank Len in TMG for making some nice cables for us. Thanks also to the TMG people for letting me use their tools freely.

I would like to thank people in the physics department, especially David Austen, for allowing me to be a teaching assistant for all these years so that I did not have to worry about economic problems during my school years. I would also like to thank CIHR for funding this project.

Special thanks to Tara Monajemi for her great help, kindness, and encouragement during my studies. I benefited immeasurably from my work with Tara, both in data collecting and image reconstruction programming. Thanks also to Dr. Brad Warkentin for his great friendship throughout these years. No matter when I wanted help, Brad always gave me the best he could offer. Thank to Steven for his willing to help me all time. I would also like to thank all my good friends in CCI: Stephen, Heather, Charlie, Anna, Keith, Michael, Erin, Alasdair, etc. Because of you all, my life at CCI has been very enjoyable and colorful and sometimes I have felt that we have been one big family.

And finally I would like to thank my family for their unlimited love, support, patience, and understanding throughout this project.

Table of Contents

List of Tables

List of Figures

List of Abbreviations

ADC	Analogue to Digital Converter
A-to-D	Analogue - to – Digital
BGO	Bismuth Germanate
CAD	Compute Aided Design
CCD	Charge Coupled Device
$CdWO_4$	Cadmium Tungstate
CMDF	Contrast Maintaining Dose Factor
CsI(Tl)	Cesium Iodide (Thallium doped)
CT	Computed Tomography
DQE(f)	Detective Quantum Efficiency (Frequency dependent)
EPID	Electronic Portal Imaging Device
IMRT	Intensity Modulated Radiotherapy
kV	Kilo-Voltage
kVCT	Kilo-Voltage Computed Tomography
LabVIEW	Laboratory Virtual Instrument Engineering Workbench
LSF	Line Spread Function
MTF(f)	Modulation Transfer Function (Frequency dependent)
MU	Monitor Unit
MV	Mega-Voltage
MVCT	Mega-Voltage Computed Tomography
NPS(f)	Noise Power Spectrum (Frequency dependent)
PC	Photo-Conductive
PTV	Planning Target Volume
PV	Photo-Voltaic
QE	Quantum Efficiency
SDD	Source to Detector Distance
SNR	Signal to Noise Ratio

Chapter 1: Thesis Overview

In fractionated radiotherapy, it is important to verify the position of tumor volume in the treatment beam for each fraction [Mohan, 1996]. Currently, portal films and electronic portal imaging devices (EPIDs) are the routine tools for radiotherapy verification. However, portal films and EPIDs are 2-D projection techniques, and thus features in different planes are superimposed into the resulting image [Boyer, et al. 1992, Munro, 1995, Shalev, 1996]. Megavoltage computed tomography (MVCT) is a 3-D imaging technique for verifying the patient's position during fractionated radiotherapy using the same megavoltage photon beam as used for the treatment [Simpson, et al. 1982]. Through the use of a MVCT scanner, information complementary to the 2-D projection image is obtained, thus increasing the amount of information available for the treatment. Therefore, a MVCT scanner is a very promising tool for radiotherapy verification [Mackie, et al. 2003]. Due to the interaction and dose deposition properties of MV photons, the MVCT has drawbacks such as its poor low contrast resolution, high image noise and the large dose of radiation delivered to patients [Rachala, et al. 1999]. Therefore, a careful design of the detectors for a MVCT scanner is required to obtain CT images with good low contrast resolution using small radiation dose. The detective quantum efficiency (DQE) is the gold standard to evaluate the performance of the imaging detectors. Higher DQE results in better contrast in CT images at a reasonable dose [I.A. Cunningham, 2000]. In a previous study, our laboratory modeled and measured the imaging characteristics of a prototype 8-element detector using cadmium tungstate ($CdWO_4$) scintillation crystals and photodiodes. This study showed that the DQE of this detector at zero frequency is 26% and 19% respectively in Co^{60} and 6 MV photon beams [Monajemi et al. 2004]. Therefore, this detector can be used to obtain MVCT images with clinically useful low contrast resolution with a low radiation dose. The design and fabrication of a bench-top MVCT scanner with $CdWO_4$-photodiode detectors was carried out in the present work. The whole scanner system consists of a detector board, timing board, multiplexing board, data acquisition board, and a motor control driving a rotary stage. The detector is an array of eighty $CdWO_4$ crystals in contact with photodiodes. The purpose of this work is to integrate the sub-systems for this prototype scanner, to study the linear response and imaging characteristics of the detector system, and to collect the fan-beam data to reconstruct the image. This thesis is organized into the following chapters.

Chapter 2: Background

An overview of the relevant background material to the thesis is given in Chapter 2. First, the importance of MVCT in precision conformal radiotherapy is briefly described. The various MVCT systems previously studied and fabricated are described next. These MVCT scanners include the fan-beam and cone-beam systems using various scintillation crystals and devices, the MVCT on helical tomotherapy unit, and the MVCT used in other fields, especially industrial applications. The problems associated with the MVCT, including the poor soft tissue contrast, the high dose deposited to the patient and the low DQE of the detector are discussed.

Chapter 3: Materials and Methods

Chapter 3 provides a description of the materials, methods, and theory related to building the bench-top MVCT scanner, and measuring the linearity and the imaging characteristics of the detector. A block diagram and signal flow chart of the MVCT scanner are described, followed by the important characteristics of scintillation crystals. A detailed description of the various sub-systems is given, including their functions and electronic design. The LabVIEW graphic programming language that was used to design the user interface, to collect the data, and to control the motor movement is also presented. The experimental set up for testing the detector's response to the radiation dose and its ability to linearly measure the attenuation of the photon beam is then briefly described. Subsequently, the experimental set up to measure the important imaging characteristics of the multi-element detector array is described. These characteristics include the spatial frequency dependent modulation transfer function (MTF (f)), noise power spectrum (NPS (f)) and detective quantum efficiency (DQE (f)). The last part of this chapter describes the experiment set up to collect the fan-beam data for reconstructing the CT image.

Chapter 4: Results and Discussion

In Chapter 4, the experimental results obtained by following the methods described in Chapter 3 are presented and discussed. In the first part of Chapter 4, the detector's response to the dose and its ability to linearly measure the beam attenuation by solid water is presented. In the second part of Chapter 4, we present the experimental results of the imaging characteristics of the detector array including the measured aliased and pre-sampled line spread functions (LSF). The last section of Chapter 4 presents the measured sinograms of various phantoms and the reconstructed CT images of low contrast phantom in 6 MV and Co^{60} photon beams.

Chapter 5: Conclusions

The major results of this study are summarized in this chapter.

References

Boyer A. L., Antonuk L., and Frenster A., van Herk M., Meertens H., Munro P., Reinstein L. E., and Wong J., " A review of electronic portal imaging devices (EPIDs)," *Med. Phys.* 19: 1-16 (1992).

Cunningham I. A., *Applied Linear-Systems Theory*, Chapter 2, Handbook of Medical Imaging Vol. 1, edited by Van Metter R. L. (SPIE Publications 2000).

Mackie T. R., Kapatoes J., Ruchala K., Lu W., Wu C., Olivera G., Forrest L., Tome W., Welsh J., Jeraj R., Harari P., Reckwerdt P., Paliwal B., Ritter M., Keller H., Fowler J., and Mehta M., "Image guidance for precise conformal radiotherapy," *Int. J. Radiation Oncology Biol. Phys.* 56: 89-105 (2003).

Mohan R., "Intensity modulated radiotherapy", in *Teletherapy: Present and Future*, edited by Mackie T. R and Palta J. R. (Advanced Medical Publishing, Madison, WI, 1996), pp.761-793.

Monajemi T. T., Steciw S., Fallone B. G., and Rathee S., "Modeling scintillator-photodiodes as detectors for megavoltage CT," *Med. Phy.* 31: 1225-1234 (2004).

Munro P., "Portal imaging technology: Past, present, and future," *Semin. Radiat. Oncol.* 5: 115-133 (1995).

Ruchala K. J., Olivera G. H., Schloesser E. A., and Mackie T. R., "Megavoltage CT on a tomotherapy system," *Phys. Med. Biol.* 44: 2597-2621 (1999).

Shalev S., "Megavoltage portal imaging", in *Teletherapy: Present and Future*, edited by Mackie T. R and Palta J. R. (Advanced Medical Publishing, Madison, WI, 1996), pp.445-469.

Simpson R. G., Chen C. T., Grubbs E. A, and Swindell W., "A 4-MV CT scanner for radiation therapy: the prototype system," *Med. Phys.* 9: 574-579 (1982).

Chapter 2: Background

2.1 Why MVCT

The main goal in radiation therapy is to deliver a very accurate dose of radiation to a well-defined target volume with minimal damage to surrounding healthy tissues, resulting in the eradication of the disease, the prolongation of life, and/or the improvement in the quality of life [Van Dyk, 1999]. In order to achieve this goal, conformal radiotherapy has been developed [Mohan, 1996]. This radiotherapy technique is an attempt to conform the shape of the treatment beams in all three dimensions to the exact shape of the tumor and at the same time to minimize the dose to the surrounding normal tissue [Mohan, 1996]. In many cases, the use of conformal radiotherapy alone is not sufficient to deliver the desired tumor and normal tissue doses, especially when a critical organ is located close to a concave shaped planning target volume (PTV) such as in head and neck and prostate cancers [Mohan, 1996].

In order to overcome some of the shortcomings of conformal radiotherapy, intensity modulated radiotherapy (IMRT) has been developed. In conformal therapy, while the beams are conformed to the shape of the PTV, the beam intensity is uniform within the unblocked part of the field. In IMRT, the intensity of the beam within the conformed portion of the field is modulated to provide even greater conformance of the dose to the PTV [Mohan, 1996]. Thus, IMRT results in a high dose gradient around the target volume. The situation is complicated due to daily set up variations, tumor shape changes, and organ motion in multi-fractionation. Therefore, it is important to verify the position of the target volume in the treatment beam and the delivered dose during fractionated radiotherapy.

Conventionally, the clinical set-up is monitored retrospectively using projection radiographs, which are formed using either x-ray film or digital imaging devices. Indeed, digital portal imaging systems have become a routine tool in many radiotherapy departments [Lewis, et al. 1992]. Despite the fact that significant information is contained in the projection radiograph, soft tissue detail and thus the tumor sites themselves typically cannot be seen. Furthermore, because the radiograph is a projection image, features in different planes will all be superimposed. MVCT is an imaging technique for verifying the patient's position during fractionated radiotherapy using the same megavoltage (MV) photon beam as used for the treatment. By using a CT scanner, information complementary to the two-dimensional projection image is obtained, thus increasing the amount of information available about the treatment [Lewis, et al. 1992].

2.2 Various types of MVCT

According to Swindell et al. [1983], the requirements for a MVCT system to provide data suitable for treatment planning and patient setup verification are 2 mm voxel sizes and a 1% contrast resolution to differentiate the soft tissue. Toward this end, a number of MVCT systems have been previously designed and developed [Simpson, et al. 1982, Swindell, et al. 1983, Brahme, et al. 1987, Lewis, et al. 1992, Nakagawa, et al.1994, Guan, et al. 1998, Hesse, at el. 1998, Mosleh-Shirazi, et al. 1998, Mildgley, et al. 1998, Ruchala, et al. 1999, Jaffray, et al. 2002, Ford, et al. 2002, Groh, et al. 2002, Seppi, et al. 2003]. These MVCT systems can be categorized either by geometry such as fan-beam MVCT and cone-beam MVCT or by the type of detectors such as MVCT with solid-state detectors, liquid ionization chambers and gas detectors.

2.2.1 Fan-beam MVCT with Solid-state Detectors

2.2.1.1 Plastic scintillator and silicon photodiode detectors

The MVCT was originally developed at the University of Arizona [Simpson, et al. 1982, Swindell, et al. 1983]. The system was constructed by attaching a plastic scintillation and silicon photodiode detector system opposite to the treatment head of a 4 MV Varian conventional C-arm Clinac-4 linear accelerator (Varian Medical Associates, Palo Alto, California) to create a third generation CT scanner. There were 80 plastic scintillation detectors arranged in an arc at a distance of 140 cm from the source. Each detector was composed of a block of plastic scintillator material (Pilot-B with a density of 1.1 g/cm^3) optically coupled to a pair of photodiodes. The scintillator dimensions were 7.4 x 20 x 50 mm^3, the incident x-rays being perpendicular to the 7.4 x 20 mm^2 face. The detector elements were optically isolated from each other. The output from each photo-detector pair was fed into a leaky integrator, and a sample and hold (S/H) circuit in each of the eighty detector channels read the peak output from each integrator. Then the eighty S/H outputs were multiplexed into one sequential output by a two-stage multiplexer. Finally the sequential output was digitized by a 12-bit A-D converter and stored in a microcomputer memory. The goals of this system were to provide 2D or 3D maps of electron density distribution for treatment planning, to verify patient set up, and to provide a 3D means of checking the treatment conformation according to the plan.

The objects were scanned using a 220° rotation by measuring projection data at 2° intervals. The *estimated* dose delivered to the phantom in 100 second scan was 53 cGy and it was higher than that utilized in the image-forming projection data (12 cGy) since the system was not able to measure every radiation pulse. An electron density resolution of 1% was estimated from signal to noise ratio (SNR) of 100 calculated as the ratio of mean CT number and its standard deviation for water. An experimental demonstration of the system's capability to resolve 1% density differences was not provided.

2.2.1.2 BGO scintillation crystals and silicon photodiode detectors

The Arizona MVCT system had been upgraded several times. The first upgrade version was to change the 80 plastic scintillation detectors to 96 Bismuth Germanate ($Bi_4Ge_3O_{12}$ or BGO) scintillation detectors at a distance of 180 cm from the source [Swindell, et al. 1983]. A threefold reduction in the scattered radiation reaching each detector resulted from increasing the distance from 140 cm to 180 cm. The angle subtended at the source by adjacent detectors was resultantly decreased from 5.3 to 3.5 m radians; thus the sampling frequency was increased. As a result, using this MVCT system and a 4MV linac (Varian conventional c-arm Clinac-4 linear accelerator, Varian Medical Associates, Palo Alto, California), the limiting spatial resolution improved from 4 mm to 3 mm. The large circular discs of electron densities of about 1% different from the background might have been barely visible using an image-forming radiation dose of 10 cGy. The actual dose delivered to the phantom was around 53 cGy since only a fraction of radiation pulses were utilized in the projection data. More important improvement was that the BGO has a much higher density (7.13 g/cm^3) compared to the plastic detectors (1.1 g/cm^3). The absorption efficiency of the BGO detectors (for 50 mm thickness) is about 83% compared to the 25% of the plastic detectors (same 50 mm thickness), therefore the BGO detectors may have much higher detective quantum efficiency (DQE) than plastic detectors.

This system at last became a prototype MVCT scanner at Royal Marsden Hospital [Lewis, et al. 1992]. This MVCT scanner was comprised of an array of 124 BGO scintillation crystals, with each crystal optically coupled to a silicon photodiode. The scintillation crystal dimensions were 5 x 20 x 50 mm^3, with a quantum efficiency (QE) for 2 MeV photons of about 80%. Each scintillation crystal was connected to its own channel of leaky electronic integrator whose output was multiplexed to a single analog-to-digital converter (ADC) interfaced to an IBM_AT microcomputer. The scintillation crystal-photodiode array was mounted in a light-tight Perspex container, which was curved in such way that the detector elements were arranged on the circumference of a circle of diameter 200 cm with the x-ray source at the center. This results in a 10 mm slice width at the isocenter (100 cm from the source). The signals from the detector elements were carried to 8 separate circuit boards by ribbon cables. Each circuit board was composed of 16 channels of electronics and a 16:1 analogue multiplexer. Then the outputs from the eight circuit boards were transmitted to a microcomputer and were multiplexed into one sequential output by the remaining 8:1 multiplexer located in the microcomputer. Finally, the output was digitized by a 12-bit ADC converter and saved in the microcomputer memory. The system is reported to provide a low contrast of 5% and a limiting spatial resolution of 3 mm for an image-forming dose of 1 cGy. The estimated dose delivered to the 30 cm diameter phantom per slice was 12 cGy since $1/12^{th}$ of the delivered radiation pulses were measured in the projection data. The electron density resolution of this system was probably poorer compared to previous system due to lower dose and higher photon beam energy.

Brahme at the University of Stockholm [Brahme, et al. 1987] acquired the MVCT images with the 50 MV racetrack microtron using the BGO detector. The system consisted of a single BGO scientillation crystal, which was mounted on the axis of a stationary Bremsstrahlung beam. The investigated objects were translated and rotated as in a first generation CT scanner. The radiation was produced by a 50 MV racetrack microtron, and the extracted electrons were focussed on to a 1 mm diameter spot on a 1.5 mm thick tantalum target. An 8 cm Al and 0.1 mm Pb were used as the electron stoppers.

In this way, the mean photon energy was around 20 MeV. The desired spatial resolution can be achieved from 6 - 3 mm through adjusting the SDD from 140 – 180 cm respectively. Due to the large number of Compton and pair electrons, and pair positrons produced in the investigated object, a lepton filter made of a 2 mm thick Pb sheet was used to surround the detector crystal. In this way, only secondary electrons produced in the Pb foil were able to reach the detector; thus the number of secondary electrons was proportional to the photon fluence on the crystal. This allowed for an excellent scatter rejection and improved resolution. The authors presented the first tomographic images of a thorax phantom. The spatial resolution is of the order of 2 mm using a crystal thickness of 5 mm. The image contrast is similar to that generated with 300 kV x-rays primarily due to the considerable influence of pair production at 50 MV. The authors didn't report the deposited dose to get one image probably because of the experimental first generation geometry.

2.2.1.3 Cadmium tungstate ($CdWO_4$) photodiode detectors

The Nakagawa group in the University of Tokyo [Nakagawa, et al. 1994] developed a MVCT system similar to the Arizona system. Their MVCT detector system was made up of 120 detectors, each containing a $CdWO_4$ scintillation crystal coupled to photodiodes. The detector system is mounted on a linear accelerator at a distance of 160 cm from the beam source. According to the authors, each crystal is sandwiched between two 0.85 mm heavy metal collimators to eliminate scattered dose; however, the authors were probably attempting to reduce cross-talk due to Compton scattering among crystals since such a thin septa plate is inadequate to remove the high energy scattered radiation produced in the patient. CT scanning was performed in a third generation geometry. The source and detectors were rotated around the object over 210° (half scan + fan angle) in 38 seconds. They used Mitsubishi linac (MITSUBISHI LINAC ML-20M, Japan) beam at 4 MV and 6 MV energies collimated to 0.5 cm x 40 cm narrow slit. The estimated dose delivered per scan in 4 MV and 6 MV beams was 1.4 cGy and 2.8 cGy respectively; experimental measurement of the dose delivered in the MVCT experiments was not reported. Moreover, a polystyrene pin of -41 HU was not visible in the image amounting to a poorer than 4.1% contrast resolution.

2.2.1.4 MVCT Using Electronic Portal Imaging Devices (EPID) Devices

Guan and Zhu [Guan, et al. 1998] used an EPID device to get MVCT images. These authors used the SRI – 100 EPID (Philips Medical Systems, Crawley, UK) as the MVCT detector. This system was composed of a fluorescent screen, a flat mirrors optical system and a charge-coupled-device (CCD) camera (256 x 256 pixels). In the isocentre plane (100 cm from the source), the maximum image size for this detector was 19 cm x 25 cm with each pixel of 0.48 mm x 0.77 mm. The photon beam from the 6 MV accelerator (Primus, Siemens Medical Systems, Concord, CA) was collimated to narrow 1 cm x 25 cm slit to reduce the effect of scattered radiation. Therefore, a 2D detector was effectively reduced to a 1D detector in a third-generation geometry. The objects to be imaged were centered at the isocenter (100 cm from the source) and the detector was placed at 160 cm from the source. The authors used a novel multi-level scheme algebraic reconstruction technique (MLS-ART) to study the portal computed tomography reconstruction. For the 200 monitor units (MUs) delivered during each scan, the dose at the isocentre was around 50 cGy. They achieved a contrast detectability of ~2.5% (object size 5 mm x 5 mm) and a spatial resolution of 2.5 mm.

Hesse [Hesse, at el. 1998] in Germany used a video-based EPID (BIS 700, Wellhofer Dosimetrie, Schwarzenbruck, Germany), as their MVCT detector. The BIS 700 was developed especially for quantitative dose measurements and belonged to the group of video-based EPIDs. The BIS 700 system was composed of a 1 mm thick copper plate coated with a 134 mg/cm^2 GD_2O_2S:Tb phosphor foil. The phosphorescent light produced inside the foil is viewed by a slow-scan CCD camera via a front-surface 45^0 mirror. The system provides images of 512 x 512 pixels with a pixel size of 0.6 mm in both lateral directions. Thus the maximum sensitive area of the system is 30.7 x 30.7 cm^2. The source was the 6 MV photon beam of Siemens KD-2 operated at a dose rate of 200 MU per minute with the field size of 1 x 25 cm^2. The limiting spatial resolution is about 3 mm and a contrast resolution of 9% in the reconstructed images. The measure energy fluence distribution was shown by the BIS signal. The reconstructed images depicted spatial and contrast resolutions sufficient for imaging of the gross patient anatomy, needed for treatment verification in many clinical cases. The dose to the patient is too high at the moment. But they believed they could reduce the dose to 15.8 cGy after optimizing the detector system [Hesse, at el. 1998].

2.2.2 Cone-beam MVCT with solid detectors

2.2.2.1 MVCT with CsI(Tl) crystals and a CCD camera

Mosleh-Shirazi et al. [Mosleh-Shirazi, et al. 1998] developed a cone-beam MVCT using a two dimensional (2-D) array of optically isolated CsI(Tl) crystals. A lens and CCD camera system digitizes the optical image produced by the 2-D crystal array. The size of each crystal in the array is 3 x 3 x 10 mm^3. The detector system is attached to the gantry of a Philips SL25 accelerator. The scintillation detector is located 150 cm away from the X-ray source. The detector area projects to 30 x 40 cm^2 at the plane of the isocentre (100 cm from source). The quantum efficiency (QE) of this detector is about 18% for a 6 MV x-ray beam. This detector allows a low contrast resolution of 2% in phantom images with a dose of 40 cGy, and a high contrast spatial resolution of about 2.5 mm. Perhaps, the main drawback of this system, including the other video-based systems mentioned in the previous section, is that there is a significant loss of optical photons in the optical chain connecting the scintillation detector array to the CCD camera.

2.2.2.2 MVCT with a commercial EPID

Midgley [Midgley, et al. 1998] used a standard commercial EPID attached to an isocentric linac (Varian 2100C, Varian Medical Associates, Palo Alto, California) and the Feldkamp cone beam reconstruction algorithm [Feldkamp, et al. 1984] to produce cone beam tomographic reconstruction. The EPID was a liquid-filled matrix ionization chamber (Varian Portal Vision V3.1, Varian Medical Associates, Palo Alto, California) with sensitive area 32.5 x 32.5 cm^2 and may be sampled to a 256 x 256 matrix producing 1.27 x 1.27 mm^2 size pixels. The measurements were performed in a 6 MV Bremsstrahlung photon beam with the EPID operating in fast acquisition mode. A source to detector distance (SDD) of 145 cm with a 22.5 x 22.5 cm^2 field (defined at 100 cm) was used to completely irradiate the sensitive area of the EPID. Using 90 views, the system delivered a central dose of 90 cGy, and depicted a density resolution of 4%.

2.2.2.3 MVCT with an amorphous silicon EPID

Ford, et al. [2002] have made an attempt to perform dose reconstruction using the Varian aS500 amorphous silicon (aSi) EPID (Varian Medical Associates, Palo Alto, California) and cone-beam CT imaging with 6 MV photons from a linear accelerator (Varian Clinac 2100EX, Varian Medical Associates, Palo Alto, California). The detector used in this system is an indirect detection active matrix flat panel imager using 340 micron thick gadolinium oxysulfide scintillation screen illuminating a 2-D array of amorphous-silicon photo-diodes. The scattered radiation, that is produced in the patient, is reduced by using 1 mm thick copper plate on top of the scintillation screen. The pixel size was 0.76 x 0.76 mm^2 with total 512 x 384 pixels. A low contrast resolution of 2% at 200 cGy with 100 cone beam projections was reported.

Groh, et al. [2002] also utilized a flat panel imager (FPI) and medical linear accelerator (SL20, Eleckta Oncology Systems, Norcross, GA) to study the cone beam CT at MV photons. An aluminum arm was constructed to support the FPI opposite the MV source. The FPI (PerkinElmer Optoelectronics RID 256-L) incorporates a x-ray converter which comprises a 1 mm Cu plate and a Kodak Lanex Fast-B 133 mg/cm^2 GD_2O_2S:Tb phosphor. A 256 x 256 active matrix array of a-Si:H photodiodes and TFTs with a pixel pitch of 0.8 mm were directly coupled to the converter. The FPI was mounted to the drum of the accelerator at a SDD = 159 cm, and a cylindrical phantom was placed at isocenter (source to axis distance = 100 cm). For the 12 x 12 cm^2 field used in this study, the dose to the center of the phantom was computed to be 0.015 cGy per x-ray pulse. The gantry angle was recorded with a precision of 0.04^0 by digitizing the gantry angle readout voltage for each projection image. The electron density difference is about 5% and 2% respectively for 6 cGy and 32 cGy dose per scan.

In order to develop an image receptor capable of forming high-quality MVCT images using modest radiation doses, Seppi, et al. [2003] constructed a 2-D array of optically isolated, thick CsI scintillation crystals that was attached to flat panel sensor (PaxScan 4030A, Varian Medical Associates, Palo Alto, California). The image data was collected in cone-beam geometry using a 6 MV beam from a conventional linear accelerator. The FPI has a pixel matrix of 2048 x 1536 with 194 micron pixel pitch resulting an active area of 39.7 x 29.8 cm^2. The detector comprises of a CsI(Tl) crystal matrix 38.8 x 28.5 cm^2 in area with crystal dimension of 0.38 x 0.38 x 8 mm^3. Five sides of each crystal are coated with a reflective powder/epoxy mixture, and the un-coated faces of the crystals in the array assembly faced the flat-panel sensor. A timing interface system generated a "master clock" that controlled both the image acquisitions by the imager and the pulsing of the linear accelerator. With this timing interface, as little as one accelerator pulse (0.023 cGy at the isocenter) could be used to form projection images. Different CT phantoms irradiated by a 6-MV X-ray beam (Varian Medical Systems 2100C/D linear accelerator–S/N 207, Varian Associates, Palo Alto, CA) were imaged to evaluate the performance of the imaging system. The phantoms were mounted on a rotating stage and 360 projection images were acquired in 48 s. These projections were reconstructed into CT images using the Feldkamp cone-beam CT reconstruction algorithm [Seppi, et al. 2003].

Using an irradiation dose of 16 cGy (360 projection x 0.046 cGy/projection), the obtained contrast resolution was ~1% for large objects. High-contrast structures as small as 1.2 mm are clearly visible. The reconstructed CT values are linear ($R^2 = 0.98$) with electron density between 0.001 and 2.6 g/cm^3. The reconstructed images of an anthropomorphic phantom showed that soft-tissue structures such as the heart, lung, kidneys, and the liver are visible.

Although cone-beam can offer higher resolution and larger field of view, the increased field of view also requires larger detector array and correction for scatter artifacts.

2.2.3 MVCT on Helical Tomotherapy unit

As the gas detectors have much lower density compared to solid state detectors, thus they usually have very poor QE at MV photon energy. Presently, the main gas detector used for MVCT is the xenon gas detector in helical tomotherapy unit [Ruchala, et al. 1999]. In order to compensate for poorer detector efficiency, the detectors are made longer in the beam direction. Also the separating tungsten septa usually are made very thin to reduce the dead spaces between sensitive elements. The primary photons interact mainly with the tungsten septa plates. The electrons released and the low energy scattered photons produced from these interactions are readily attenuated in xenon gas, and increase the QE of this detector. The CT images from this system are used for patient set up verification and as such an image registration between the MVCT and the planning CT images is performed prior to each treatment. Dose reconstruction combines the transmission data that is taken during treatment with images of the patient's anatomy to calculate the spatially distributed dose to the patient [Kapatoes, et al. 2001]. The UW Tomotherapy MVCT detector consists of 738 detector cells each comprising of two gas cavities divided by a thin tungsten septa plate. The distance between the two plates defines the size of a single gas cavity. The separation is 0.32 mm, which is also the thickness of the plates. The septa plates are 2.54 cm long. At every odd plate a high-voltage of +300 V is applied. The even plates act as charge-collecting electrodes for the charge produced in the gas cavities, which are filled with xenon gas under high pressure. The charge produced in the two adjacent xenon cavities is collected together to yield the signal of a detector cell. On top and at the bottom of the detector, front and back plates made of 0.1 cm and 0.5 cm thick aluminum, respectively, are mounted. For the 4 MV ORION linac, the front plate acts as a filter for the contaminant electrons. Using this system, a low contrast resolution below 2% and resolution of 3 mm with doses ranging from 8 to 12 cGy have been reported [Ruchala, et al. 1999].

2.2.4 MVCT used in other Fields

MVCT has also found important applications in industrial fields. For imaging some large dense objects the megavoltage photons are necessary since kV photons will be completely attenuated within the object. Furthermore, the main problems for MVCT in medical field are the low soft tissue contrast and the high dose deposited in the patients. But for MVCT in the industrial fields, these problems don't exist or are less serious. Most objects to be imaged have obvious mass attenuation coefficient differences, thus the low contrast resolution is not the significant issue for imaging industrial objects.

The most important industrial applications of MVCT are in the areas of, for example, the aviation and automobile industries, where safety is of fundamental importance and material faults may have catastrophic implications.

Azevedo, et al. [1993] used CT equipment to inspect some particular aircraft components for defects, such as the cracks, voids and flaws. These included fuselage panels and single crystal turbine blades. They also used CT to quantitatively analyze material compositions, such as the density/atomic number gradients and inhomogeneities in the aluminum-lithium composites.

Persson, et al. [1985] illustrated the ability of tomography to detect and locate defects of a number of polymeric products, such as the airplane tires, shock absorbers, thick-walled rubber cylinders and welded thermoplastic car components. They also showed the possibility of using CT to study cross-link density gradients in, e.g., vulcanized rubber.

In forestry and tree sciences, CT allows the quantitative determination of the locally varying absorption coefficients for penetrating radiation within a thin slice of the trunk. The tomogram not only shows hollows, rot, knots and other defects but also the distribution of water in the invisible interior of the stem [Habermehl, et al. 1997]. A portable, Cesium-137 base MVCT system has been developed and built for computerized tomography of standing trees in forests and parks at Philips University in Germany [Habermehl, et al. 1997]. This equipment was used in forestry sciences and in tree-care to obtain information about decay, checks, heartwood formation and moisture content. Additional applications are in the detection of interior decay by fungi and its spread in a horizontal and vertical direction, in determining sapwood area dependent on fertilization, in evaluating development and treatment of tree wounds and in studying the influence of resin tapping on the water supply of pines.

In order to improve the high spatial resolution, Munier, et al. [2002] used large-area digital flat panel detectors instead of the conventional crystal scintillation detectors. They used this detector system to inspect the printed microelectronics circuit boards, electronic devices and connection techniques. They showed that this system could detect and measure 25 μm diameter bonding wires. They also used it to detect the de-lamination, internal flaw or other micro-structural anomalies in composite materials.

In addition to these applications in industrial fields, MVCT was also applied to image nuclear fuel pin bundles, ocean acoustic tomography, analysis of failure, dimensional measurements of inaccessible geometrical features [Flisch, et al. 1999], geophysical exploration and welding inspection on pipeline in oil industry.

Another interesting application of CT in industry is the reverse engineering applications [Flisch, et al. 1999, Dastarac, et al. 1999, Losano, et al., 1999]. Reverse Engineering is a term which is used to describe the creation of a digital data set based on a physical representation, reversing the regular process of going from an idea through CAD construction to a product [Flisch, et al. 1999]. Since a CT image is digital data, it can be processed by image processing software for display and enhancement, or converted into a format (such as CAD, STL, IGES file) suitable for other purposes. It can be made available to other users and compatible to the most commonly used engineering design software applications. Hence, CT can play an important role in the field of Reverse Engineering. When modifications to the real object must be updated into its CAD model, CT can be a powerful tool relating the CAD model of a component to the real component itself [Losano, et al. 1999]. Using this new technology it is possible to reduce the time to market for development of new products. Thus companies can realize substantial competitive advantages [Flisch, et al. 1999, Habermehl, et al. 1997].

2.3 Problems With MVCT

The main problems encountered in MVCT imaging are the poor soft tissue contrast, high dose deposited in the patient and low DQE of the detector system.

2.3.1 Poor Soft Tissue Contrast

The primary goal for MVCT in medicine is to verify radiotherapy treatments. Thus the images are intended for the purpose of determining the patient's organ positions at the time of treatment, and for providing reliable density information for treatment planning and dose reconstruction. Since the tissues of interest generally have low-contrasts, it is particularly important that the MVCT images have good low-contrast resolution. Failure to visualize soft tissue structures such as tumor and sensitive organs would significantly diminish the utility of the MVCT images. But comparing to kVCT images, MVCT images have inherently poorer soft tissue contrast. This is because in MV photon energy range, the physical interactions of incident photons are mainly Compton interactions.

Compton interactions are almost independent of atomic numbers of the interacting media. Therefore at MV energies the main reason for tissue contrast would be the density difference which is not very significant among soft tissues (e.g. 1040 kg/m^3 for muscle, 1650 kg/m^3 for bone and 916 kg/m^3 for fat) [Johns and Cunningham, 1983]. But at kV photon energies, e.g. 60 keV photons in water, Compton scattering accounts for about 88% of attenuation and photoelectric effect accounts for 6.7% [Attix, 1986]. The photoelectric interaction coefficient varies almost proportional to $Z^{3.8}$ and Z^3 per electron for low and high atomic number (Z) materials respectively [Johns and Cunningham, 1983]. Therefore, even though different tissues in the body show small differences in Z (e.g. 7.64 for muscle, 12.31 for bone and 6.46 for fat) [Johns and Cunningham, 1983], the differences in the photoelectric process are significant. This is the reason for rich contrast among different tissue types at kV energies. In general, the attenuation coefficients decrease significantly from kV to MV energies [Attix, 1986]. Obviously, it is easier to detect a given percent contrast between two objects if the objects are highly attenuating as opposed to objects that have lower attenuation coefficients. Thus the smaller attenuation at MV energies results in inferior soft tissue contrast than that at kV energies.

2.3.2 High Dose Deposited in Patients

The patient dose is higher in MVCT since the energy deposited per interaction is higher than for kV photons. The mass energy-absorption coefficients are not very different for the same tissue at kV or MV energies. For example, the mass energy-absorption coefficient of water is 0.032 cm^2/g for 60 keV photons and 0.026 cm^2/g for 2 MeV photons [Attix, 1986]. This means that the fraction of the photon energy deposited in the medium is similar at kV and MV energies. Therefore, for the same photon fluence, the absolute value of the dose deposited in the patient is larger at MV energies compared to kV energies [Ruchala, et al. 1999].

Ruchala et al. [1999] derived a relationship for contrast-maintaining-dose factor (CMDF) which gives the increase in MV dose given to the patient to maintain the same level of low contrast resolution as in kV images.

$$CMDF = \left(\frac{\mu_{en} \cdot E \cdot \bar{\phi}_{phan}}{\eta \cdot \phi_{\text{det}}} \right)_{kV}^{MV} \left(\frac{1}{\mu^2} \right)_{kV}^{MV} \tag{2-1}$$

where μ_{en} and μ are the linear energy-absorption and attenuation coefficients;

E is the energy of incident x-ray photons;

$\bar{\phi}_{phan}$ is the average fluence inside a cylindrical phantom;

ϕ_{det} is the fluence at the detector; and

η is the detective quantum efficiency. The subscript and super-subscript indicate that a ratio of the quantities given in brackets is calculated between MV and kV photon energies.

In this equation, the first term on the right shows the photon reduction ratio (PRR), which tells the factor by which the number of photons detected in MVCT is less than the number of detected kV photons. The second term on right is the kV contrast factor, which benefits kV contrast by the squared ratio of the mass-attenuation coefficients for kV and MV energies, $[(\frac{\mu}{\rho})_{MV}^{kV}]^2$ [Barrett, et al. 1976, Simpson, et al. 1982].

According to Ruchala, et al. [1999], for 30 cm thick patient, the CMDF between 1.33 MV and 60 kV photons was 37 and 13 respectively for 5 mm and 20 mm thick $CdWO_4$ detectors. Thus in order to have similar low soft tissue contrast to kV images, the patient has to receive higher deposited dose. In practice, therefore, a compromise between the low contrast resolution and dose is generally required. In order to decrease the dose deposited in the patient, the number of MV photons incident on the patient has to decrease significantly. Accordingly, the photon fluence reaching the detector also decreases which, coupled with the low detector DQE as discussed in the next section, increases image noise further decreasing the low contrast resolution.

2.3.3 Low DQE

At MV energies, only a very small fraction of the photons actually interact with the detector. Furthermore, interacting photons do not deposit all of their energy in the interacting medium. While at kV energies, almost all of the energy of the interacting photons is deposited in the detector [Johns and Cunningham, P168, 1983]. Therefore, the detective quantum efficiency of detectors at MV photon energies is much lower than that at kV photon energies. Solid state detectors are over 80% efficient at kV energies, but is only slightly better than 20% efficient at MV photon energies. For xenon gas, the xenon chambers are only around 1% efficient at MV photon energies [Ruchala, et al., 1999].

Despite the aforementioned problems with MVCT, there are some distinct advantages of MVCT over kVCT for radiotherapy verification. Although MVCT may provide relatively poor low contrast resolution making it an inferior tool for patient positioning verification as compared to kVCT, its relatively low cost and ease of engineering make it an attractive option. With respect to image quality MVCT images should still be sufficient for both dose verification and patient position verification. A further advantage of MVCT as compared to kVCT is the relative increase in the linearity of tissue electron density to CT number of MVCT. This is because the fact that Compton scattering is the dominant interaction at MV energies. The Compton cross section mainly depends on the electron density. Therefore, at MV energies, CT numbers provide a better measure of the actual linear attenuation coefficients of different tissues. This potentially makes MVCT more accurate for dose calculations and inhomogeneity corrections as compared to kVCT [Ruchala, et al., 1999; Keller, et al., 2001]. Another advantage of MVCT is that MV photons are more penetrating than kV photons. Therefore, for imaging larger patients and patients containing metallic implants, MV energies are advantageous in reducing photon starvation and metal artifacts in the images [Ruchala, et al. 1999].

2.4 Thesis Objectives

The objective of this project is to build a bench-top MVCT $CdWO_4$ photodiode detector in order to evaluate its imaging characteristics, and to reconstruct CT images using standard filtered back-projection method from the collected fan-beam projection data.

As we mentioned in the last section, at MV photon energies, inherent contrast among tissue types is lower; dose per unit incident fluence is higher; and the DQE of the detectors is lower. Therefore, MVCT images have higher noise and reduced low contrast resolution for a given dose compared to diagnostic CT images. The spatial frequency dependent DQE of MVCT detectors must, therefore, be optimized in order to obtain clinically useful low contrast images for a reasonable dose. Inorganic scintillators have a comparatively good detection efficiency for hard radiation [van Eijk, 2002]. Of the presented materials, CsI:Na, CsI:Tl, $CdWO_4$, NaI:Tl and BGO are the traditional scintillators [van Eijk, 2002]. Among them, we think $CdWO_4$ is the better candidate scintillator for MVCT detector. Because $CdWO_4$ has higher density with 7.9 g / cm^3 (compared to 3.67 for NaI, 4.51 for CsI and 7.1 g / cm^3 for BGO [van Eijk, 2002]) to offer higher quantum efficiency. It's optical yield is large (≈20000 photons/MeV compared to 9000 photons/MeV for BGO [van Eijk, 2002]) and afterglow is small (< 0.02% at 60 msec compared to 0.5% at 60 ms for CsI(Tl) [Monajemi, et al. 2004]). With 520 nm peak emission wavelength [Farukhi, 1982], cadmium tungstate has a better optical spectral match to self-scanned photodiode arrays than NaI or BGO [Kearfott, et al. 1990]. It's non-hygroscopicity, compactness and stability also make it an attractive detector at MV energies. A previous study [Monajemi, et al. 2004] showed that the DQE at zero frequency of this $CdWO_4$-photodiode detector was 26% and 19% in Co^{60} and 6 MV photon beams, respectively. Therefore, this detector could be used to obtain MVCT images with clinically useful low contrast resolution and a low dose.

References

Attix F. H., *Introduction to radiological physics and radiation dosimetry*, (John Wiley & Sons, New York, 1986).

Azevedo S, Martz HE and Schneberk DJ, "Potential of computed tomography for inspection of aircraft components," *Nondestructive Inspection of aging aircraft* (san Diego, CA) ed Valley M, Del Grande N and Kobayashi A (SPIE—The International Society for Optical Engineering), 47-57(1993).

Barret H. H., Gordon S.K., and Hershel R.S.," Statistical Limitations in Transaxial tomography," *Comput. Biol. Med.* 6: 307-323 (1976).

Brahme A., Lind B, and Nafstadius P., "Radiotherapeutic computed tomography with scanned photon beams," *Int. J. Radiation Oncology Biol. Phys.* 13: 95-101 (1987).

Dastarac D., "Industrial computed tomography at TOMO ADOUR: control and digitizing," *DGZfP Proceeding BB 67-CD*, Poster 9, 193-201 (1999).

Farukhi M. R., "Recent developments in scintillation detectors for X-ray CT and positron CT applications," *IEEE. Trans. Nucl. Sci.* NS-29: 1237-1249 (1982).

Feldkamp L. A., Davis L. C., and Kress J. W., "Practical cone-beam algorithm," *J. Opt. Soc. Amer*, 1: 612-619 (1984).

Flisch A., Wirth J., Zanini R., Breitenstein M., Rudin A., Wendt F., Mnich F., and Golz R., "Industrial computed tomography in reverse engineering applications," *DGZfP-Proceeding BB 67-CD*, Paper 8, 1-9(1999).

Ford E. C., Chang J., Mueller K., Sidhu K., Todor D., Mageras G., Yorke E., Ling C. C., and Amols H., "Cone-beam CT with megavoltage beams and an amorphous silicon electronic portal imaging device: potontial for verfication of radiotherapy of lung cancer," *Med. Phys.* 29: 2913-2924 (2002).

Groh B. A., Siewerdsen J. H., Drake D. G., Wong J. W., and Jaffray D. A., " A performance comparison of flat-panel imager-based MV and kV cone-beam CT," *Med. Phys.* 29: 967-975 (2002).

Guan H. and Zhu Y., "Feasibility of megavoltage portal CT using an electronic portal imaging device (EPID) and a multi-level scheme algebraic reconstruction technique (MLS-ART)," *Phys. Med. Biol.* 43:2925-2937 (1998).

Habermehl A. and Ridder H.-W., "Gamma-ray tomography in forest and tree sciences," Developments in X-Ray Tomography ed Bonse U (Proceedings of SPIE vol.3149. SPIE—The International Society for Optical Engineering), Bellingham, Washington, p234-244 (1997).

Hesse BM, Spies L and Groh BA, "Tomotherapeutic portal imaging for radiation treatment verification," *Phys. Med. Biol.* 43:3607-3616 (1998).

Jaffray D. A., Siewerdsen J. H., Wong J. W., and Martinez A. A., "Flat panel cone-beam computed tomography for image guided radiation therapy," *Int. J. Radiation Oncology Biol. Phys.* 53: 1337-1349 (2002).

Johns H.E., Cunningham J.R., *The Physics of Radiology*, 4th ed. (Thomas, Springfield, IL, 1983).

Kapatoes J. M., Olivera G. H., Balog J. P., Keller H., Reckwerdt P. J., and Mackie T. R., "On the accuracy and effectiveness of dose reconstruction for tomotherapy," *Phys. Med. Biol.* 46: 943-966 (2001).

Kearfott K. J. and Murty K. N., "A high spatial resolution computed electro-optic radiation detector array," *Health Physics* 58: 99-105 (1990).

Losano F., Marinsek G., Merlo A. M., and Ricci M., "Computed tomography in the automotive field--Development of a new engine head case study," *DGZfP Proceedings BB 67-CD*, Paper 10, 65-73 (1999).

Lewis D. G., Swindell W., Morton E. J., Evans P. M., and Xiao Z. R., " A megavoltage CT scanner for radiotherapy verification," *Phys. Med. Biol.* 37: 1985-1999 (1992).

Mackie T. R., Holmes T., Swerdloff S., Rockwerdt P., Deasy J. O., Yang J., Paliwal B., and Kinsella T., " Tomotherapy: a new concept for the delivery of dynamic conformal radiotherapy," *Med. Phys.* 20: 1709-1719 (1993).

Midgley S, Millar RM, and Dudson J, "A feasibility study for megavoltage cone beam CT using a commericial EPID," *Phys. Med. Biol.* 43: 155-169 (1998).

Mohan R., "Intensity modulated radiotherapy", in *Teletherapy: Present and Future*, edited by Mackie T. R and Palta J. R. (Advanced Medical Publishing, Madison, WI, 1996), pp.761-793.

Monajomi T.T., Steciw S., Fallone B.G., Rathee S., "Modeling scintillator-photodiodes as detectors for megavoltage CT," *Med. Phy.* 31: 1225-1234 (2004).

Mosleh-Shirazi M. A., Evans P. M., Swindell W., Webb S., and Partidge M., " A cone-beam Megavoltage CT Scanner for Treatment Verification in Conformal Radiotherapy", *Radiotherapy and Oncology*. 48: 319-328 (1998).

Munier B., Casagrande J-M, Koch A., Kaftandjian V., Duvauchelle P., and Babot D., "High resolution digital flat panel detector for NDT," *NDT.net* 7(12): 1-10 (2002).

Nakagawa K., Aoki Y., Akanuma A., Onogi Y., Terahara A., Sakata K., Muta N., Sasaki Y., Kawakami H., and Hanakawa K., "Real-time beam monitoring in dynamic conformation therapy," *Int. J. Radiation Oncology Biol. Phys.* 30: 1233-1238 (1994).

Persson S and Ostman E, "Use of computed tomography in nondestructive testing of polymeric materials," *Applied Optics* 24:4095-4104 (1985).

Ruchala K. J., Olivera G. H., Schloesser E. A., and Mackie T. R., " Megavoltage CT on a tomotherapy system," *Phys. Med. Biol.* 44: 2597-2621 (1999).

Seppi J., Munro P., Johnsen S. W., Shapiro G., Tognina C., Jones D., Pavkovich J., Webb C., Mollov I., Partain L. D., and Colbeth R. C., "Megavoltage cone-beam computed tomography using a high-efficiency image receptor," *Int. J. Radiation Oncology Biol. Phys.* 55: 793-803 (2003).

Simpson R. G., Chen C. T., Grubbs E. A, and Swindell W., "A 4-MV CT scanner for radiation therapy: the prototype system," *Med. Phys.* 9: 574-579 (1982).

Swindell W., Simpson R. G., and Oleson J. R., "Computed Tomography with a linear accelerator with radiotherapy applications," *Med. Phys.* 10: 416:420 (1983).

Van Dyk J., "Radiation oncology overview", in *The Modern Technology of Radiation Oncology*, edited by Van Dyk J. (Medical Physics Publishing, Madison, WI, 1999), pp.1-19.

van Eijk C. W. E., " Inorganic scintillators in medical imaging," *Phys. Med. Biol.* 47: R85-R106 (2002).

Chapter 3: MATERIALS AND METHODS

The main purpose of this project is to fabricate an experimental MVCT system that is based on $CdWO_4$ detectors. In scintillation-photodiode detectors, the x-rays interact with the scintillation material and set the electrons in motion. These electrons ionize and excite the scintillation material that emits flashes of light. A fraction of optical energy may reach the photodiodes where it creates additional charge in the depletion layer of the photodiode. The charge produced in the photodiode elements is collected by a charge sensitive amplifier, digitized and stored into the computer for further processing. Therefore, a scintillation photodiode detector, in its simplest form, contains a scintillation crystal, a photodiode, an amplifier, an analog-to-digital (A-to-D) converter and a computer. Detailed experimental design of this project is to ensure that the bench-top MVCT scanner with $CdWO_4$-photodiode detectors works appropriately. Therefore, in this chapter, we describe details about our prototype detector array of $CdWO_4$. We also describe the designing, fabricating and testing procedures of the data acquisition timing control system, precision rotary stage control system and an analog data multiplexer unit for a prototype 80-element detector array. In addition, a user interface is designed using the LabVIEW (National Instruments, Austin, Texas, USA) graphic programming language. This software system allows the user to collect a specified amount of data for each radiation pulse for each detector and then stores the data in the hard disc of the computer.

The important characteristics of the MVCT detector are the linear response to the radiation dose and its ability to linearly measure the attenuation of photon beam. In this chapter, we briefly describe the experimental set up for testing the linearity of the detector system.

The other important imaging characteristics of multi-element detector array are spatial frequency dependent modulation transfer function (MTF (f)), noise power spectrum (NPS(f)) and detective quantum efficiency (DQE(*f*)). This chapter also discusses the experiments used for measuring these functions for the prototype detector.

The last part of the experimental design is concerned with collecting fan-beam data for MVCT images.

3.1 System Overview

Figure 3.1 shows the block diagram of the bench-top MVCT system. The objects to be imaged are placed on the precision rotary stage between the x-ray source and the detector array. The x-ray source from a linear accelerator (or Co^{60}) is collimated to a thin fan-beam. The transmitted x-ray fluence is measured by an 80-element detector array where each element contains a $CdWO_4$ crystal and a pair of photo-diodes. The data acquisition board contains a single analog to digital converter (A-to-D) that resides in a personal computer. The data measured by the 80-element detector array is therefore multiplexed on a single data line that is connected to the A-to-D board. The data acquisition timing board provides control signals to the 80-element detector array, 80:1 multiplexer system, motor control and the data acquisition. For pulsed radiation from a linear accelerator, the master trigger for all the timing signals generated by the timing board is derived from the "SYNC" pulses of the linear accelerator. The linear accelerator produces a 5-6 μsec long radiation pulse after 1-2 μsec following each "SYNC". There are three operational modes for “SYNC” pulses. If linear accelerator is operated in the service mode with the feed back from the monitor chamber turned off, the radiation produced by the linear accelerator has a certain regular pattern. The radiation is always on for 5 pulses followed by no radiation in one pulse (250 MU/min, 600C, Varian Medical Systems). In the other two modes, which are clinical and service modes with the automatic servo control using the feed back from the monitor chamber turned on, the radiation produced by the linear accelerator is somewhat irregular. But in the service modes, there is a great capability of damaging the machine with a single keystroke. Therefore as a novice user for the linac machine, I did most of the experiments in the thesis in clinical mode. In case of continuous radiation as produced by a Co^{60} source, the timings for various sub-systems are controlled by a computer independent internal clock located within the timing control board. The requirements and generation of the specific timing signals for each sub-system is described in the section of timing control board.

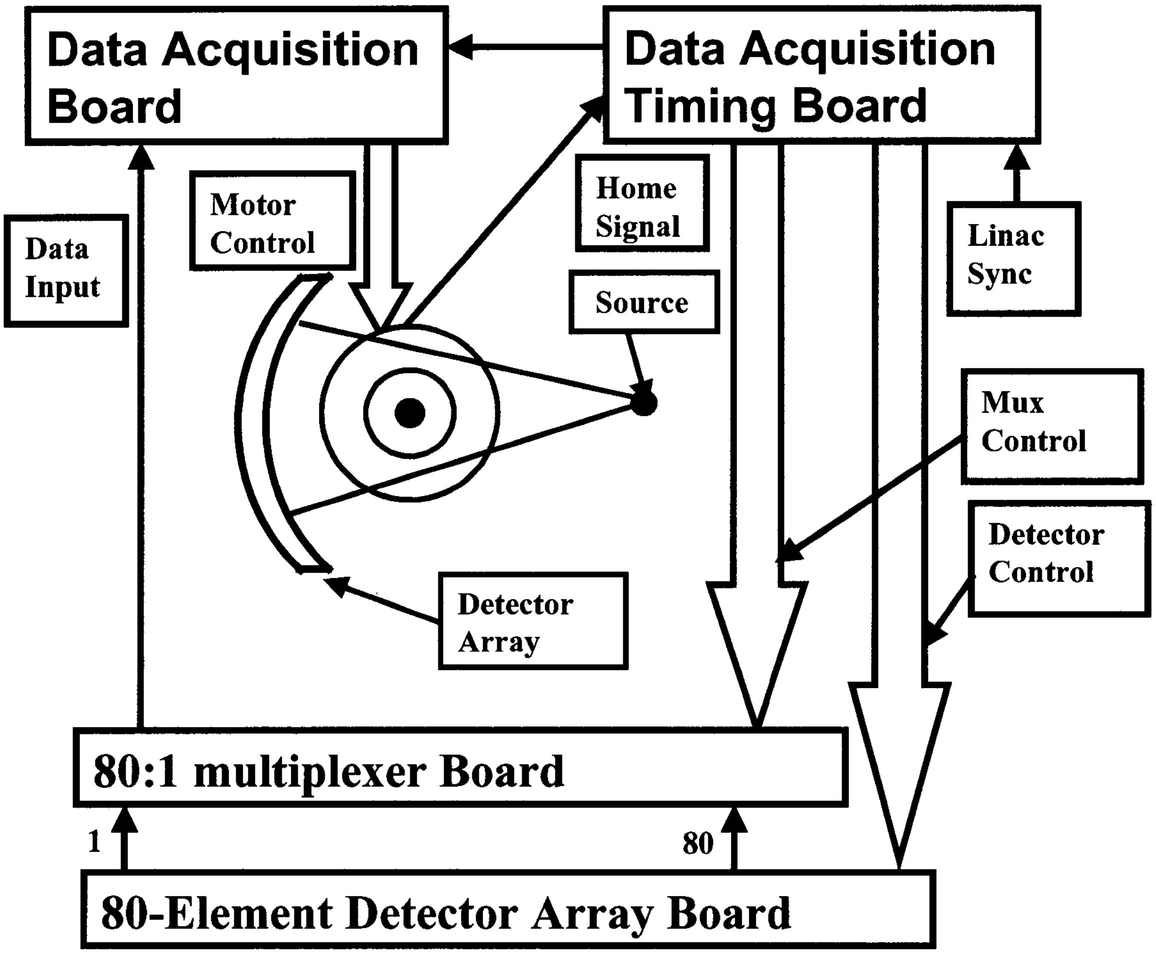

Figure 3.1: The block diagram of the experimental MVCT system. The objects to be imaged are placed on the rotary stage between the x-ray source and the detector array.

Figure 3.2 shows the photograph of the 80-element detector assembly and the precision rotary stage along with the power supply of the detector board and the stepper motor controller. A specially designed low contrast phantom is placed on the rotary stage. The phantom is further described in section 3.7. The detector assembly is secured on the stage that can linearly translate the entire detector assembly with a manual control knob in steps of 0.375 mm. The entire experimental set-up is arranged on the treatment couch in the treatment room that houses 600C linear accelerator (Varian Medical Systems, Palo Alto, CA). The box containing the timing control board and the control PC with the data acquisition board are not shown in this figure since they are set beside the console control system outside of the treatment room.

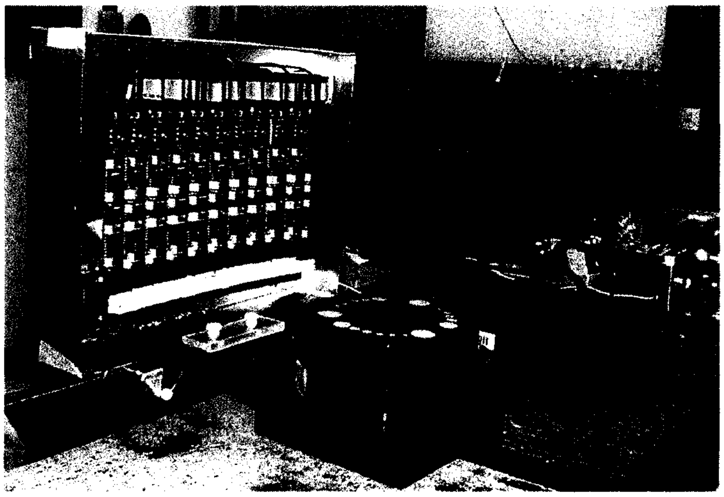

Figure 3.2: A photograph showing the 80-element detector assembly and the precision rotary stage including the necessary power and controller for stepper motor. The phantom to be imaged is placed on top of the rotary stage.

3.1.1 Signal Flow Diagram

The signal flow for the whole system is given in Figure 3.3. At first, the data acquisition timing board produces all control signals synchronized with the "Sync" pulses from the linear accelerator. Among them, there are seven detector select signals A_0 to A_6. These seven-bit numbers are used to select one out of the 80 detectors at one time. Other signals are detector-timing signals used for integrating and holding the detected charge. The motor control signals are produced in the data acquisition board and pass through the timing and multiplexer boards to the motor driver. For the detector select signals, three of them, A_0, A_1 and A_2 together with the detector timing signals, go through the ribbon cables to each of the ten detector boards. The 8:1 multiplexer in each 8-element detector array board multiplexes the 8 detector signals into a single data line based on the status of A_0, A_1 and A_2. Therefore, there are ten such single data lines, each with a multiplexed signal from 8 detectors. The higher level detector-select signals A_3, A_4, A_5 and A_6 are used to select one of ten data lines at one time. The higher level bits are thus used in the multiplexer unit that implements a 10:1 multiplexer. The combination of 8:1 multiplexer on each detector board with this 10:1 multiplexer produces the overall 80:1 multiplexer system. Finally, the single line containing time-multiplexed data for 80 detectors is connected to the A-to-D board.

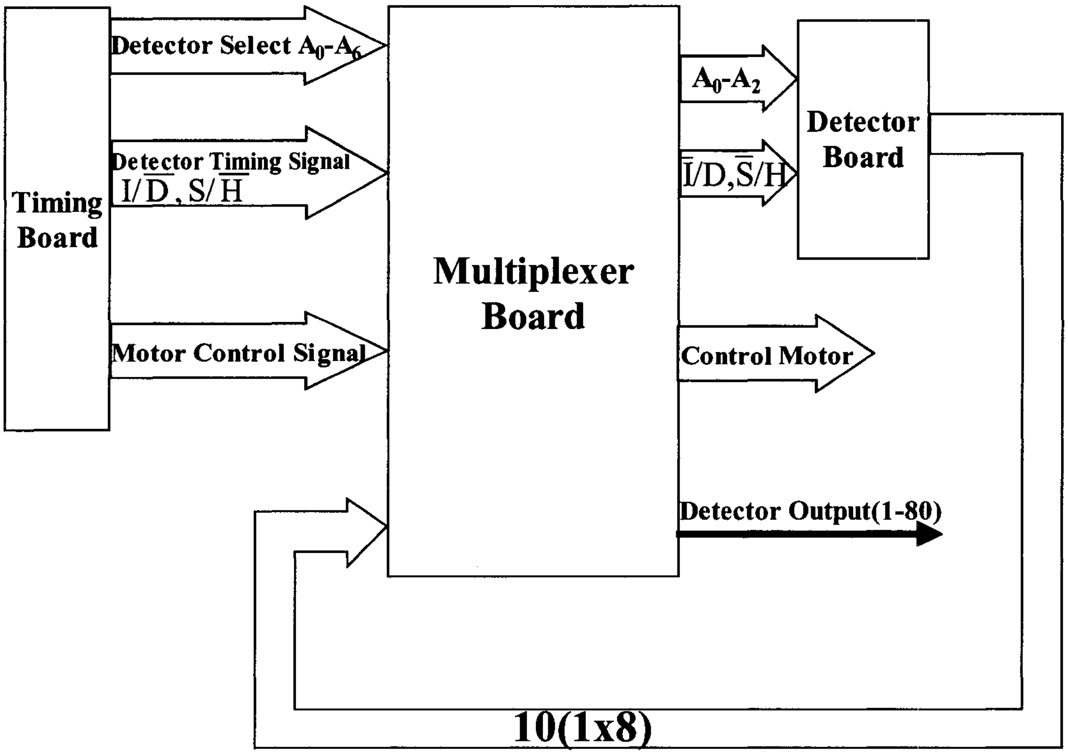

Figure 3.3: The signal flow diagram of the bench-top MVCT scanner.

Each of the sub-systems shown in Figure 3.1 is separately described in the following sections preceded by a general discussion regarding the scintillation crystals for CT imaging application.

3.2 Choice of Scintillation Materials

3.2.1 Important Characteristics for CT imaging Application

Scintillating materials are widely used in current medical diagnostic imaging modalities using x-rays or gamma rays [van Eijk, 2002]. For photon detection, heavy inorganic scintillators are the most often used [Derenzo, et al. 1992]. This can be explained by the comparatively good detection efficiency of heavy inorganic scintillators for hard radiation. The density and the attenuation coefficient of a scintillation material determine its x-ray quantum efficiency for a given spectrum of photons.

Most common heavy inorganic scintillators used in medical imaging applications are NaI(Tl), BGO, CsI(Tl), LSO, $ZnWO_4$, $PbWO_4$ and $CdWO_4$. Table 3.1 shows some important properties of these detectors for CT imaging applications. At kV photon energies, an interacting x-ray photon deposits almost all of its energy. Therefore, x-ray quantum efficiency directly determines the detector noise for a given energy fluence of photons incident on the detector. At MV photon energies, interacting photons not only deposit only a fraction of its energy but the deposited fraction has wide range determined by the angular (energy) dependent Compton cross-section as given by the Klein-Nishina formula [John and Cunningham, 1983]. Therefore, the detector noise is generally determined by the DQE of the detector. However, higher quantum efficiency scintillation detector generally results into higher DQE. The other factors that may affect the DQE of the detector are the light yield, optical self-absorption and optical spectral match with the photodiode. Scintillation materials that have higher light yield are desirable since light detection becomes easier. It is also important that there is a reasonable match between the optical emission spectrum of the scintillation material and the sensitivity spectrum of the photodiode or else a larger fraction of the optical photons will remain undetected. The spectral response of silicon photodiodes ranges from 320 nm to 1100 nm [Hamamatsu, 1994]. The scintillation material should also be non-hygroscopic and relatively non-toxic so that it does not require complex enclosure and it can be easily handled. Afterglow is the phenomenon that luminescence can still be observed after the end of x-ray exposure, which is caused by radiant recombination of electrons and holes delayed by trapping of electrons or holes [Blasse, et al. 1994]. Afterglow is defined as the fraction of light emitted from the scintillation material after the end of x-ray exposure [Blasse, et al. 1994]. Large afterglow will result in incorrect signals being recorded because readings are influenced by the previous detector signals.

Based on the above four important properties for CT imaging application, we choose $CdWO_4$ as our scintillator for this project according to the following analysis. Although NaI(Tl) has been used extensively in medical imaging because of its excellent light yield [Vittore, et al. 2000], its lower density and hygroscopicity make it unsuitable scintillator for MV CT imaging. Although BGO has a reasonably high density, its light yield is very low. The light output of CsI(Tl) is the largest of all scintillation materials. As discussed in the previous chapter, CsI(Tl) has been used in MV cone beam CT [Mosleh-Shirazi, et al. 1998]. However, its afterglow, measured at 6 ms after stopping irradiation, could be as high as 5%. The afterglow has become an important consideration for modern fast CT imaging. Perhaps the most important disadvantage of CsI(Tl) for a relatively slower MVCT application is its lower density. The density of CsI(Tl) is only 4.51 g/cm^3 compared to 7.9 g/cm^3 for $CdWO_4$. $ZnWO_4$ is almost as dense as $CdWO_4$ and much cheaper than $CdWO_4$, and previous investigators [Morton, et al. 1990] have used $ZnWO_4$ for MV imaging applications. But its light yield is nearly 50% of $CdWO_4$, furthermore, $ZnWO_4$ has a relatively long optical decay time of 3000 ns, a single cleavage plane, and also it is hygroscopic. Another member of the tungstate series is $PbWO_4$ which has a very high density (8.2 gcm^{-3}) and fast response time (15 ns). However, the light yield is only 200 photons/MeV [van Eijk, 2002]. As seen in Table 3.1, LSO is probably a good candidate for CT application; however, it is very difficult to grow large stress-free crystals [van Eijk, 2002] and the scintillating crystal itself is not readily available [Derenzo and Moses, 1992]. Therefore, we have chosen to utilize the detector based on $CdWO_4$ and photodiodes for MVCT application. The $CdWO_4$ was a detector of choice in fourth generation diagnostic CT systems (PQ5000, Philips Medical Systems) due to its higher quantum efficiency and ease of fabricating into detector ring.

A special application of this detector in a prototype fourth generation CT system based on the high dose rate brachytherapy source (^{192}Ir) had also been described [Berndt, 2002]. In our laboratory, we have previously studied the signal forming mechanism of $CdWO_4$ detector. The present detector system is an extension of the 8-element detector array presented previously [Monajemi, 2004 and Berndt, 2002].

Table 3.1: Properties of selected γ-ray detecting scintillators [van Eijk, 2002; Krus, Novak and Perna, 1999; Duclos, 1998; Kinloch, et al. 1994; Derenzo and Moses, 1992]

Scintillator	*Density (g/cm^3)*	*Hygro-scopic*	*Light Yield (Photons/MeV)*	*Emission Maximum (mm)*	*Afterglow (% at ? ms)*
NaI:Tl	3.67	Yes	41,000	410	0.3-5/6ms
$Bi_4Ge_3O_{12}$ (BGO)	7.1	No	9,000	480	<0.005/3ms
CsI:Tl	4.51	Slightly	66,000	550	0.5-5/6ms
Lu_2SiO_5:Ce (LSO)	7.4	No	26,000	420	-
$ZnWO_4$	7.87	Yes	10,000	480	-
$PbWO_4$	8.2	No	200	460	-
$CdWO_4$	7.9	No	20,000	495	0.1/3ms

3.2.2 The 80-element Detector Array

In the 80-element detector array, we have used 10 photodiode arrays (S5668-2, Hamamatsu, Japan) each containing 16 photodiodes (0.1175 cm x 0.2 cm) with 0.04 cm gap between them. On top of each photodiode array, we have placed 8 $CdWO_4$ crystals (Rexon Corporation, USA). Each crystal is of 0.275 cm x 0.8 cm base area and is 1.0 cm tall. A photograph showing the individual crystals and the photodiode array is given in

Fig. 3.4. The crystals are bonded together, with a 0.04 cm gap, using a mixture of epoxy resin and gelcoat [Berndt, 2002]. Each crystal thus covers two consecutive photodiode elements. The combination of one photodiode array and 8-bonded crystals gives an 8-element detector array. Figure 3.5 shows the geometry of 8-element $CdWO_4$ detector array. The photodiode dimension longer than 0.2 cm was not commercially available at the inception of this project. However, the x-ray beam width in the longitudinal (i.e. slice thickness) direction is almost always larger than 0.2 cm; therefore, we choose the crystal dimension along longitudinal direction as 0.8 cm, to cover the 0.2 cm of photodiode dimension. For the outside area of photodiode, we have placed a bare metal foil underneath the crystal area to act as a rough yet nearly perfect reflector for the optical photons and to increase the amount of light reaching the photodiodes [Berndt, 2002]. Optical coupling glue (Dow Corning 20-057) was placed atop the photodiode elements. Since the photodiode arrays abut perfectly with each other, an almost spatially uniform detector containing 80-elements was thus formed by placing 10 such combinations side by side (See the photograph in Fig. 3.2).

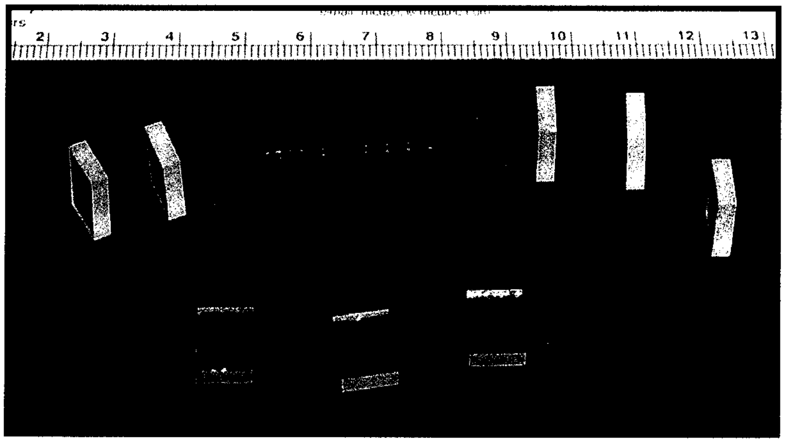

Figure 3.4: Photograph of photodiodes and single $CdWO_4$ crystals (Courtesy of Dr. Berndt, CancerCare Manitoba, Winnipeg, Manitoba).

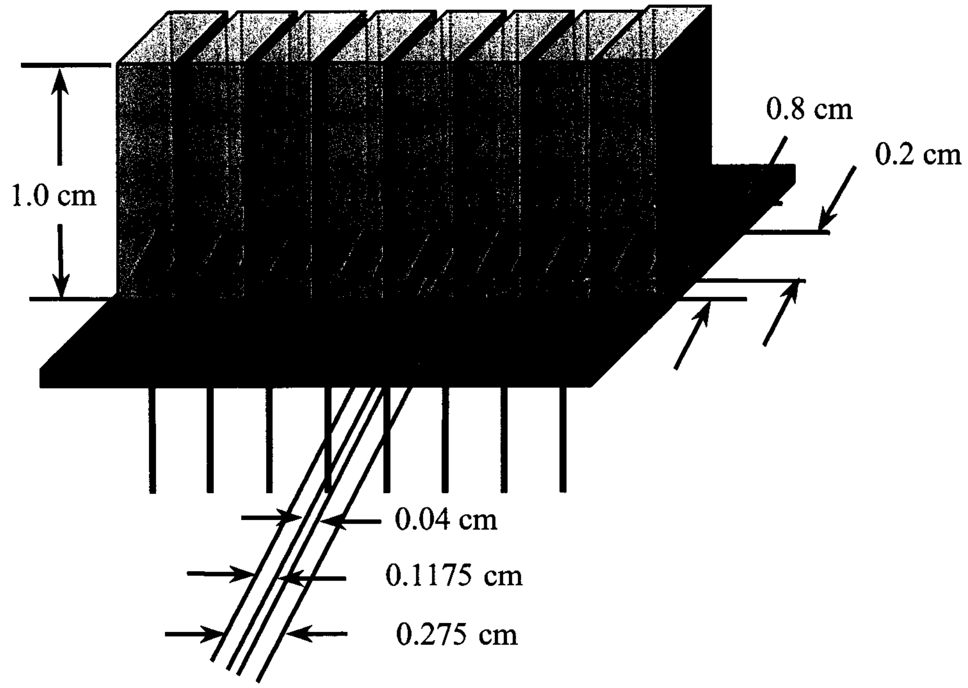

Figure 3.5: The geometric arrangement of the single $CdWO_4$ crystals and the photodiode array. The crystal dimensions are 0.275 x 0.8 x 1.0 cm^3. The photodiodes are 0.1175 cm x 0.2 cm with a 0.04 cm gap between two consecutive elements. A crystal covers two consecutive photodiode elements to form a single detector channel.

3.3 Electronic Sub-Systems of Bench-top MVCT System

Our bench-top MVCT system consists of five different circuit boards: the detector assembly board, a data acquisition timing control circuit board, a multiplexer board, a motor control circuit board and an analogue-to-digital (A-to-D) converter board. The block diagram of these components is shown in Figure 3.1. In this section, a detailed description of the design and function of different boards will be given.

3.3.1 The 80-element Detector Array Board

3.3.1.1 The Overview of Detector Array Board

The detector array board is used to integrate and amplify the signal from $CdWO_4$-photodiode for each pulse of radiation from a linear accelerator or for each integration period in case of continuous radiation.

Figure 3.6 shows the photograph of the 80-element detector array board. It contains 10 identical sub-detector assemblies, each containing the 8-element $CdWO_4$-photodiode array as described in section 3.2.2. The 10 boards are mounted on a curved steel plate such that the 80-elments are arranged in the form of an arc of 110 cm radius. The electronic system for all 80 detector channels is identical and described in the following sections. The timing signals that control the charge integration and sample-and-hold parts of the read cycle are fed from the timing control board using the ribbon cable. Each of the ten sub-detector assemblies contains an 8:1 multiplexer. The multiplexed data is carried by the co-axial cables from the detector assembly board to the multiplexer board that contains another 10:1 multiplexer unit.

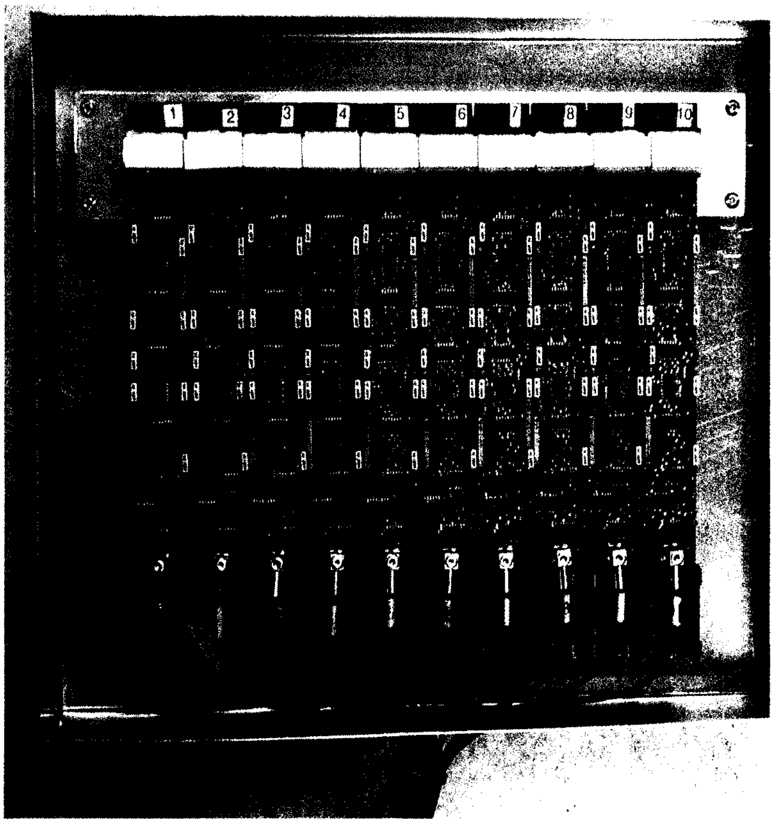

Figure 3.6: The picture of 80-element detector board. There are 10 consecutive detector boards each containing 8-element array. A set of 10 co-axial cables connects the signal output from 8-element array boards to the multiplexer board. The ribbon cable carries the timing control signals from timing board to each of the 8-element array boards.

One of the detector channel assemblies is described in detail below.

3.3.1.2 Detector Assembly Components

As we described above, our detector board consists of 10 8-element detector arrays. Each 8-element detector array constitutes eight parallel analogue signal processing channels, one for each individual detector. Figure 3.7 shows the components of the detector assembly board for one channel. Each channel consists of two photodiodes (Hamamatsu S5668-02), a gated integrator (Texas Instruments TL074C op-amp; Temic DG442 Analogue Switch), a sample and hold circuit (Analog Devices SMP-04), and an 8-to-1 multiplexer (MUX) (Fairchild semiconductor, CD4501BC). First, the MV photon beam is incident on the scintillating crystals to produce the optical photons. The photodiodes detect optical photons and produce a current that is proportional to the photon fluence incident on their corresponding crystals. The integrator circuit accumulates this current for a certain time to produce a voltage signal. Then the sample-and-hold circuit will hold this voltage signal for a certain time called hold period before being routed to an 8-to-1 analog multiplexer. During the hold period, the multiplexer in each 8-element detector array multiplexes the data from the channels into a single data line by using the control signals from the ribbon cable. A sample-and-hold circuit is needed since the A-to-D converter is shared among all 80 detector channels. This circuit follows its input voltage until it is instructed to hold the voltage for a predetermined period within each sampling interval. During this hold period, the 80-to-1 multiplexer sends the output of the channels to the A-to-D converter board one by one. This way, the output of all the channels is sampled at the same instant in time. The voltage signals are digitized to a precision of 16-bit by the A-to-D converter (National Instruments PCI-MIO-16XE-50) located in a PC. The acquisition software is written in LabVIEW (National Instruments). Different components of the detector assembly board are discussed individually in the following section.

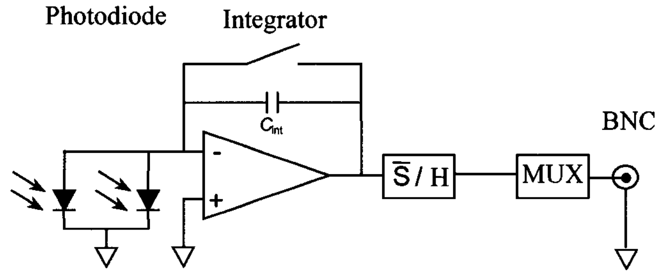

Figure 3.7: Circuit diagram showing the detector assembly components with C_{int}=1 nF.

3.3.1.2.1 Photodiodes

Photodiodes are semiconductor light sensors that produce a voltage or current when the P-N junction is illuminated by light. The photons cause electron-hole pairs to be generated by a process called photo-ionization, which can be achieved by using a surface material that is transparent to light. In a photodiode, the reverse saturation current depends on the light intensity [Rizzoni, 1996]. A photodiode may be thought of as a conventional diode with an internal current source producing a photo-current, i_{photo}, proportional to the light level present. The total current, i_{total}, measured by an external ammeter is equal to the current flowing through the photodiode, namely, $i_{total} = i_{forward} - i_{dark} - i_{photo}$. Here $i_{forward}$ is the current forced through the photodiode by the external positive voltage and i_{dark} is the current flowing through the photodiode in the reverse bias condition in the absence of light.

Photodiodes can be operated in two modes: the photo-conductive (PC) mode and the photovoltaic (PV) mode. In PC mode, where a reverse bias voltage is applied, the current is forced through the photodiode by the external bias voltage and consequently $i_{forward}$ is zero. Therefore, $i_{total} = -i_{photo} - i_{dark}$, as shown in Figure 3.8a. This means that the measured current will be directly proportional to the intensity of the light illuminating the photodiode. This is the main difference from conventional diodes in which only a small leakage or dark current i_{dark} is detected when a reverse voltage V is applied. In PV mode, a positive bias voltage or no external bias voltage is applied. When a positive bias voltage V applied across the photodiode, as shown in Figure 3.8b, then $i_{forward} > 0$ and $i_{dark} = 0$, so that $i_{total} = i_{forward} - i_{photo}$. If no external bias voltage V is applied, as shown in Figure 3.8c, the photocurrent provides the total photodiode current so that $i_{total} = -i_{photo}$.

As shown in Figure 3.8d, the response of the photodiode is linear if it is operated in reverse-biased mode or with no external voltage [Rizzoni, 1996]. In these regions, the increase in reverse saturation current is directly proportional to the incident optical energy φ_{light}. Even though, operating a photodiode in reverse voltage has the advantage of increased sensitivity due to the large size of the depletion region, the statistical (shot) noise in the i_{total} is high. Therefore, we chose to operate our photodiodes in photo-voltaic mode with no external voltage.

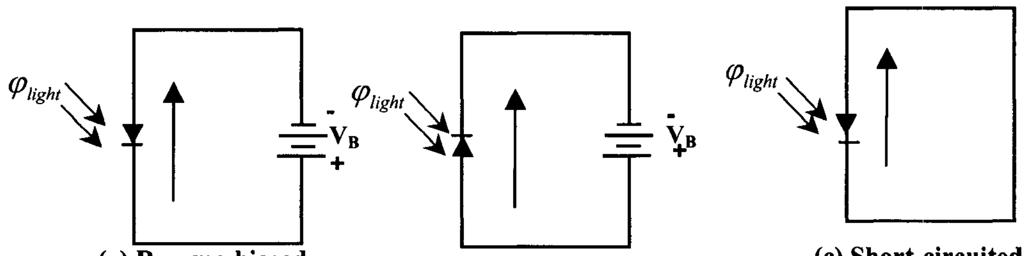

(a) Reverse-biased photodiode (PC mode)

$i_{total}=-i_{dark}-i_{photo}$

(b) Forward-biased photodiode (PV mode)

$i_{total}=i_{forward}-i_{photo}$

(c) Short-circuited photodiode (PV mode)

$i_{total}=-i_{photo}$

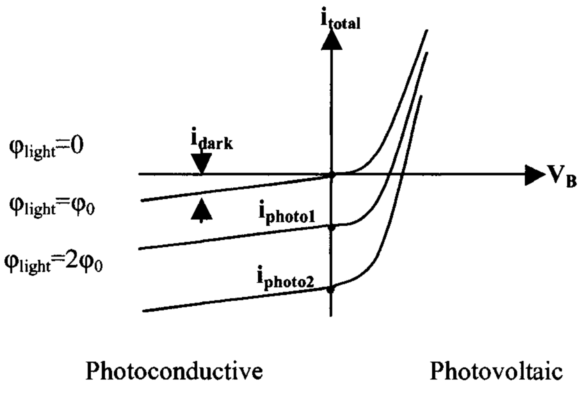

(d) i-v characteristic curve of a photodiode

Figure 3.8: Photodiode operating in (a) reverse-biased mode, (b) forward-biased mode and (c) short-circuited mode. (d) the i-v characteristic curve of a photodiode.

3.3.1.2.2 Integrator

The integrator circuit is used to collect the charge produced by the photodiode. This integrator circuit is made up of a low noise JFET operational amplifier, a 1 nF capacitor and an analog reset switch as shown in Figure 3.7. When the switch is opened, the capacitor accumulates the charge and when the switch is closed, the capacitor is discharged. In case of an ideal integrator, the output voltage ΔV_{total} is given by:

$$\Delta V_{total} = \frac{1}{C_{\text{int}}} \int_0^{T_0} (i_{photo} + i_D)dt \qquad (3.1)$$

where i_{photo} is the photocurrent, C_{int} is the capacitance in the feed back loop; T_0 is the sampling period, for our system T_0=0.7 ms. Here $i_{forward} = 0$ and $i_{dark} = 0$ because no bias voltage is applied. The current i_D is the sum of the op-amp input bias and the switch leakage currents, and can be thought of as a "dark current" (it is different from the photodiode dark current i_{dark}) in the sense that it flows even in the absence of light. Therefore, in the absence of radiation, the non-zero signal is given as

$$\Delta V_D = \frac{i_D T_0}{C_{\text{int}}} \qquad (3.2)$$

The voltage ΔV_D produced by the dark current will always be subtracted from the measurements performed in this work.

For the pulsed radiation, the radiation occurs for a short period of time within each cycle (137 Hz for 600C, Varian Medical Systems, Palo Alto, CA). The integration time could be made equal to radiation pulse duration during each cycle. This was not practically implemented since the radiation pulse-width time is known to change from one system to another.

3.3.1.2.3 Analog Switch

The analog switch is used to discharge the capacitor so that it is ready for integration during the next measuring cycle. An ideal analog switch has such properties: when it is opened, the current flowing through it should be zero; when it is closed, the voltage across it should be zero. But the real switches always have a small leakage current to flow when they are opened. However, it is not a big problem in our detector system because the leakage current produces a constant offset voltage which can be simply subtracted.

However, there are two major shortcomings for the analog switch (Temic DG442) was used here. The first one is the injection of charge from the digital control inputs into the analog outputs as a consequence of stray capacitance. This switch will inject a certain charge at the common point of the integrating capacitor, photodiode and operational amplifier when it is opened. As a result, it will introduce a relatively large random offset that is added to ΔV_{total}. Another major shortcoming of this switch is that it is easily damaged by long time radiation. Thus the analog switch must be isolated from the radiation source when the long radiation is carrying out.

3.3.1.2.4 Sample and Hold Stage

The photo-current and the integration time determine the output of the integrator stage for each channel. The integration period must be the same for all the channels. Therefore, the sample and hold circuit is used to hold the output of all the channels at the same instant in time to keep the integration time identical for all of them.

3.3.2 Data Acquisition Control Circuits---The Timing Board

The purpose of the data acquisition control circuit is to generate control signals for the gated integrator ($\bar{I}$/D), the sample and hold ($\bar{S}$/H), the MUX (A_0-A_6), and the A-to-D converter (Ext Conv). These control signals are synchronized with the radiation pulses from the linear accelerator or with the independent clock for the continuous radiation source such as Co^{60}. A functional schematic showing these components is depicted in Figure 3.9.

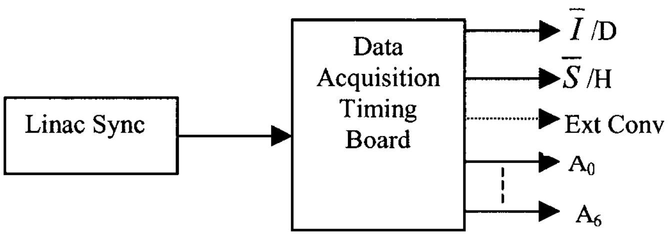

Figure 3.9: Schematic showing the function of timing board

The timing board also houses the NI 6034 AE output port, thus some control signals for motor driver from the DAQ board also go out from the timing board. These motor driver control signals together with the control signals for the gated integrator ($\overline{I}$/D), the sample and hold ($\overline{S}$/H), the MUX (A_0-A_6) go out from the timing board through the DB25(I) to multiplexer board, the detector board and the motor driver. See Figure 3.10 for the photograph of timing board. The control signal for A-to-D converter (Ext Conv) goes to the NI 6034 AE output port directly. The multiplexed single data line also goes through one of the BNC to the NI 6034 AE output port directly. The linac sync signal goes through the right corner BNC to the timing-board, see Figure 3.10.

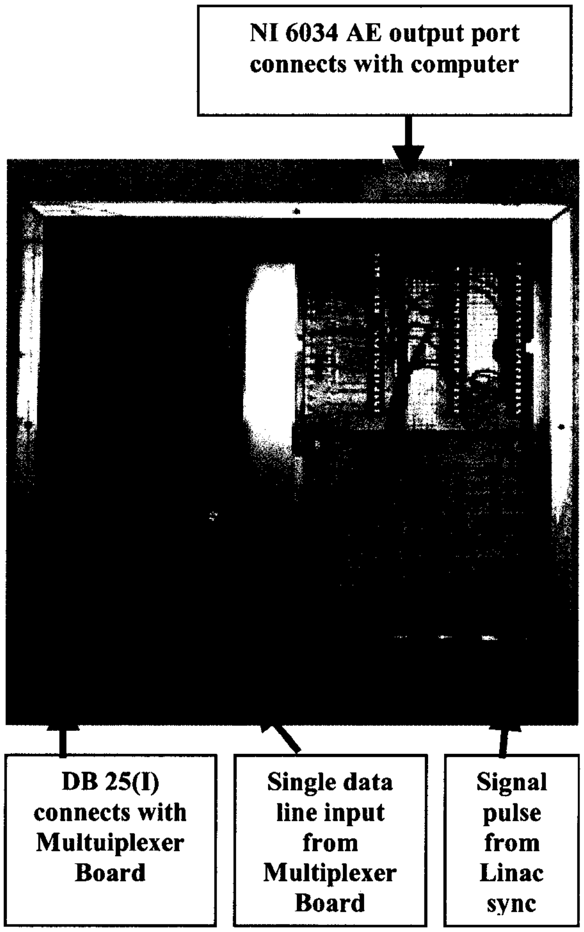

Figure 3.10: The photograph of data acquisition timing board that produces all control signals for the system.

3.3.2.1 Data Acquisition Timing Sequence

Figure 3.11 shows the data acquisition sequence for our detector system. The sync pulse from the linear accelerator (137 Hz) is chosen as the trigger. The radiation comes on 2-3 μs after the sync pulse and lasts around 5 μs. However, the sync pulse period is about 7.3 ms, therefore, the radiation is mostly on the idle mode during each sync pulse period. The data acquisition cycle starts almost immediately after the trigger signal comes on which is marked as t = 0 in Figure 3.11. At this point, the capacitor in the integrator circuit has been fully discharged and the switch is set to open by setting the $\overline{I}$/D (The bar over the “I” in $\overline{I}$/D indicates that integration occurs when the signal is low, and discharge occurs when the signal is high) to low. Therefore, the charge accumulates on the capacitor. The charge accumulation continues till t = 0.8 ms when the capacitor is discharged (switch closed). Immediately prior to discharging the capacitor, at t = 0.7 ms, the $\overline{S}$/H (The bar over the “$\overline{S}$” in $\overline{S}$/D indicates that sampling occurs when the signal is low, and holding occurs when it is high) signal is set to high to hold the integrated voltage for 4 ms. This amount of time is enough for external convert circuit to finish 80 pulses on "Ext Conv". Each pulse corresponds to data collection for one detector. During this holding interval, the seven MUX control signals (A_0-A_6) are generated synchronously with the external convert pulse (20 KHz). The seven MUX control lines (A_0-A_6) generate a 7-bit number between 0 and 79 that determines which channel is read during each external convert pulse by the A-to-D converter. The waveform at the bottom of Figure 3.11 shows the output of the sample and hold chip which is the signal being sent to the A-to-D converter via the coaxial cable. It should be noted that only $\overline{I}$/D is generated for each trigger pulse even if the detector is idling or the motor has not crossed the home position. This is done to ensure that the integrating capacitors are not saturated by the dark signal when the detector is not being used.

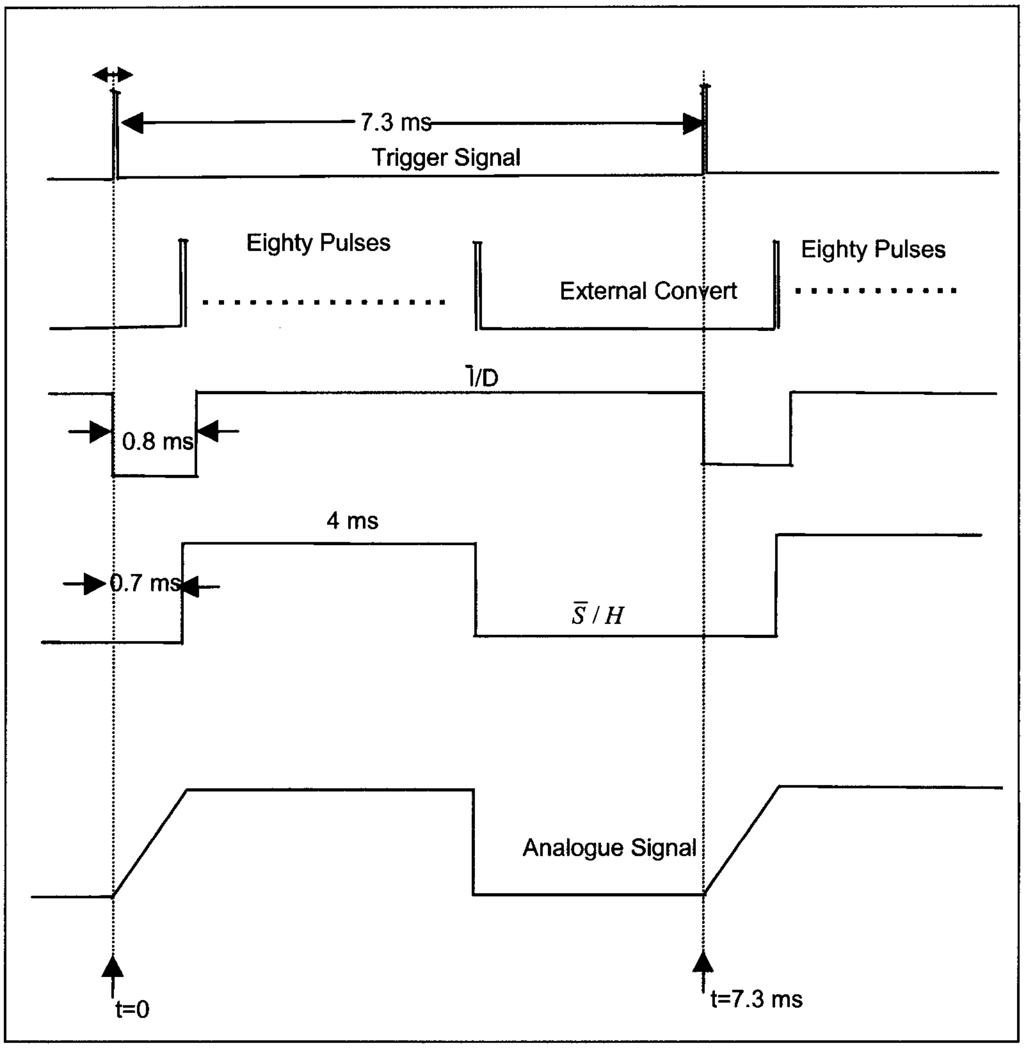

Figure 3.11: Data acquisition timing sequence for the eighty-channel detector assembly for the 6 MV measurements. Detector output after sample-hold for one of the eighty channels is shown. The trigger signal for a continuous radiation is derived from an independent clock.

3.3.3 Multiplexer Board

The data acquisition board contains a single analog to digital (A-to-D) converter. Therefore, the data from 80-detectors need to be time-multiplexed into a single data line. The first stage of multiplexing occurs within each of the ten 8-element detector boards. Each boards contains one 8:1 multiplexer unit, thus, the ten outputs provide an 80:10 multiplexing. Fig 3.12 shows the next two stages of time-multiplexing. In the first stage, provided by two middle multiplexer chips, a 10:2 multiplexing occurs. The last device on the right side of figure then provides the final 2:1 multiplexing stage

In addition to completing the stages of multiplexing, the multiplexer board also contains opto-isolators for each of the control signals generated by the timing control board. Since the timing control board is interfaced directly to the computer and uses the computer's power supply (+5 V), the timing control signals ($\overline{I}$/D, $\overline{S}$/H, A_0-A_6, Ext Conv) contain spurious undershoots and overshoots. If these signals are connected directly to the 8-element boards and the multiplexer unit, the spurious under/overshoots find their way into the detector signal outputs. Therefore, we have provided a complete electrical isolation between the analog electronics of the detectors and the digital control signal by routing the control signals via optical isolation. The schematic of the optical isolation is shown in Fig. 3.13. At the input of opto-isolator (NEC, PS9601) for each control signal, there is a light emitting diode that converts the electrical amplitude modulations into optical intensity modulations. On the output side of the opto-isolator, the photo-transistor-inverters then senses these optical intensity modulation and converts them back into electrical amplitude modulations. The +5V power supply and the electrical ground on the right side of Fig. 3.13 belong to independent supply of the detector analog electronics and thus a complete electrical isolation is provided. It should be noted that the analog signal output of multiplexer board (80:1 multiplexed data) is connected to the A-to-D board via differential signal inputs that provide the adequate electrical isolation.

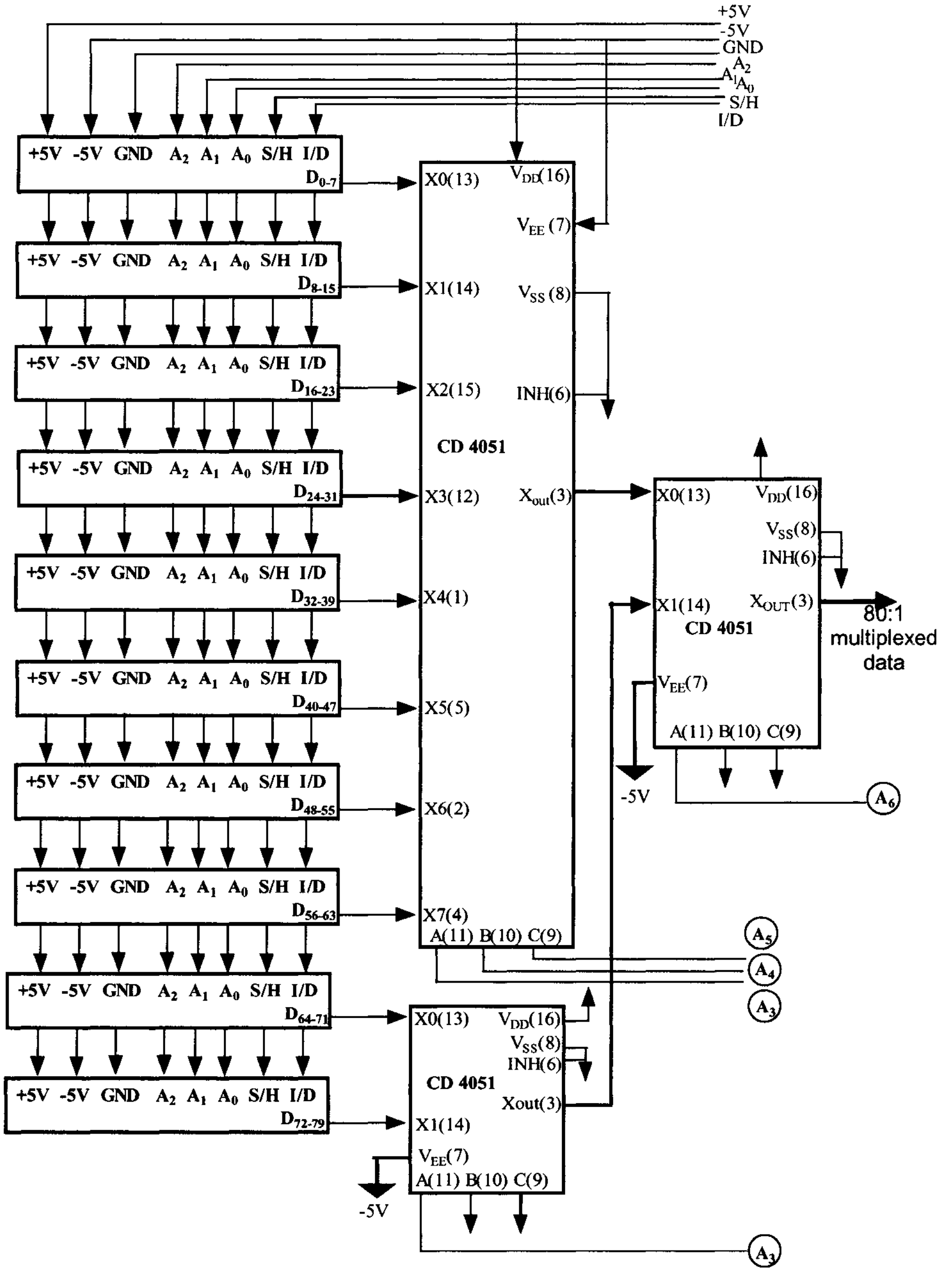

Figure 3.12: Schematic of 80:1 multiplexer. The first stage of multiplexing occurs within the 8-element detector boards that provide ten data lines each containing the time-multiplexed data for 8 channels. The second stage, provided by the two devices in the middle row, converts 10 lines into 2. Final stage, provided by the last device, provides a 2:1 multiplexer.

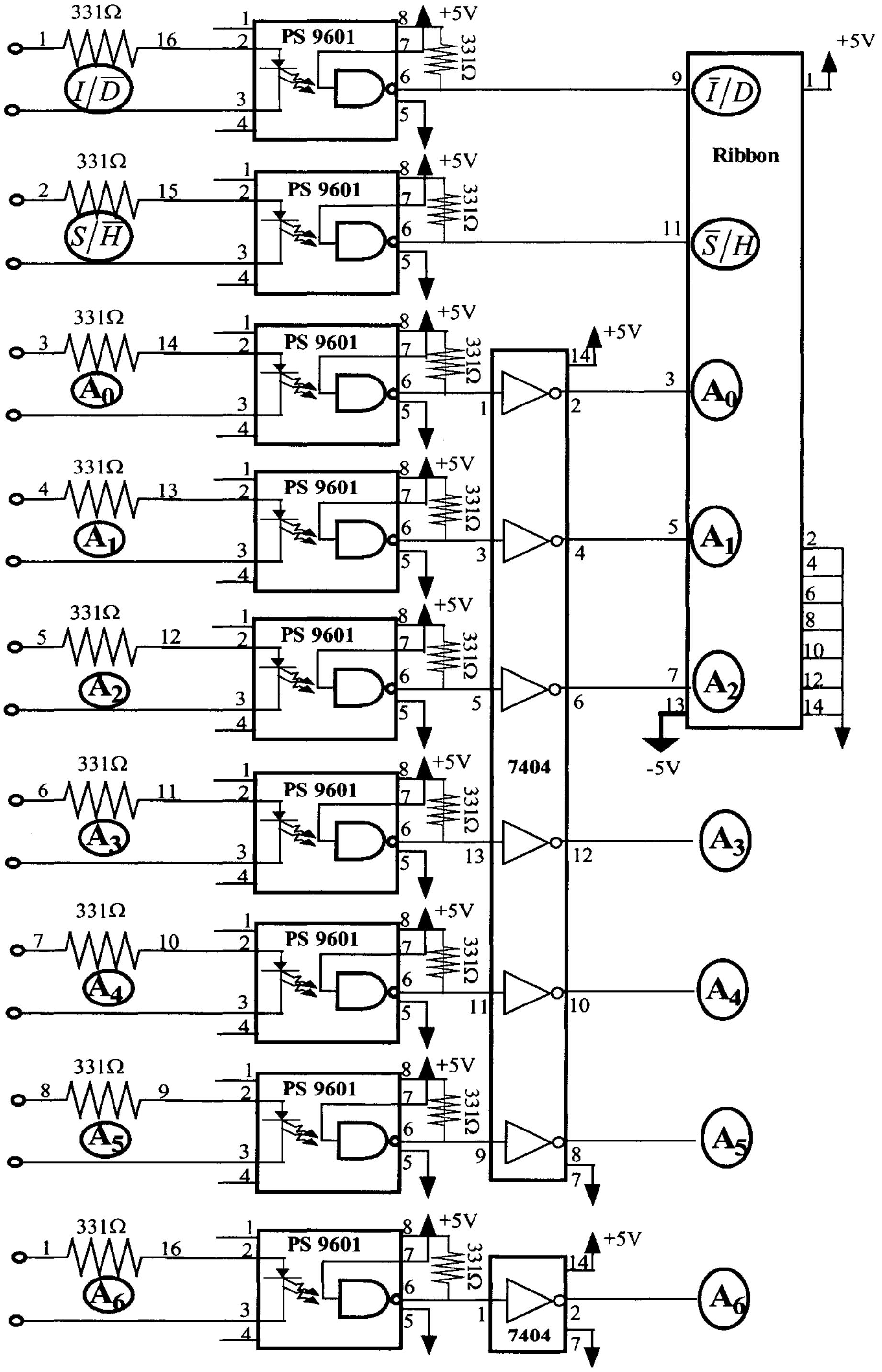

Figure 3.13: Optical isolation of each of the timing control signals in order to reduce the noise from the spurious under/overshoots in the signals from the timing control board.

As the multiplexer board is kind of communication center of the system, therefore, there are a total of 7 connection ports on the multiplexer board as shown in Figure 3.14. There is a linear supply from a regulator that gives the +5V and –5V for the analog electronics of the detector system. There are ten inputs from ten 8-element detector assemblies. There is a single data line that carries the multiplexed signal to data acquisition board. The timing control signals from the timing board are connected by a DB25(II) connector. These timing control signals are opto-isolated and transferred to 8-element detector assemblies via the ribbon cable, and to the motor driver control via another DB25(III) connector. The zero-position switch line from the motor drivers tells the home position of the rotary stage to the data acquisition board and signals the start of data collection for a single rotation.

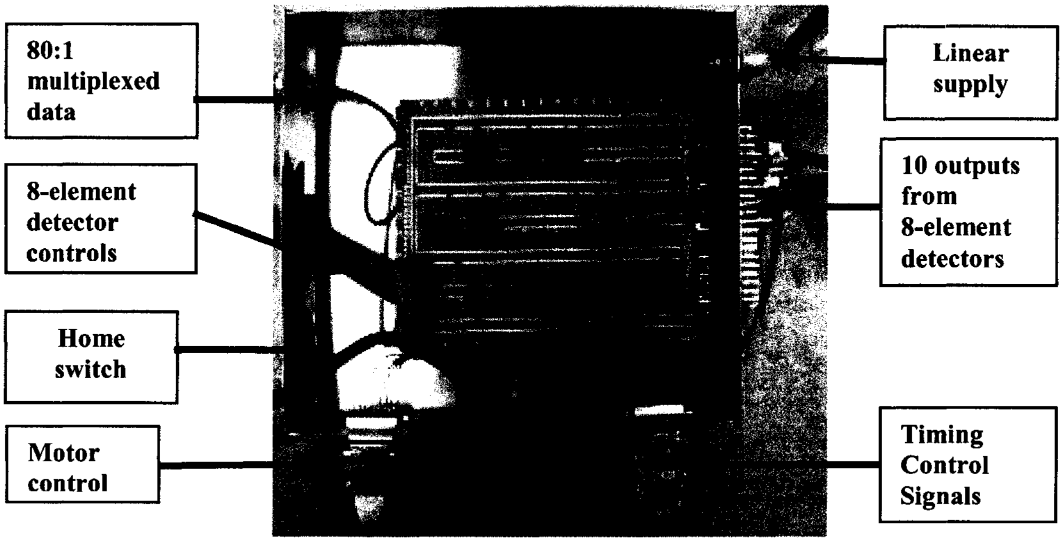

Figure 3.14: Various connections to the multiplexer board.

3.3.4 The Motor and Bench-top

For research purposes, it is more convenient to rotate the phantom instead of the x-ray source and detector assembly. We use the motor driven bench-top to rotate the phantom. The precision rotary stage (200 RT, Daedal division, Parker Hannifin Corp, USA) is rotated by a stepper motor system (ZETA 57-83, Compumotor division, Parker, USA). The stepper motor is controlled via digital port and a programmable pulse generator from the data acquisition board.

Figure 3.15 shows the photograph of stepper motor driver and the bench-top. The motor driver gets the control signals from the data acquisition board via the port DB25(IV). The zero position switch line carries the home signal when bench-top rotates to the zero position.

Figure 3.16 shows the control circuit for motor and bench system. The home switch is normally closed. When motor rotates to the zero position, the home switch will be opened that signals the data acquisition board to start collection of data. The other signals come from the data acquisition board. The DIO0 controls the direction of motor rotation; the DIO1 tells motor when to shut down the motor rotation; the DIO2 controls the motor reset; the DIO3 reads the fault from motor; and GPCTR0 controls the step rate of motor rotation.

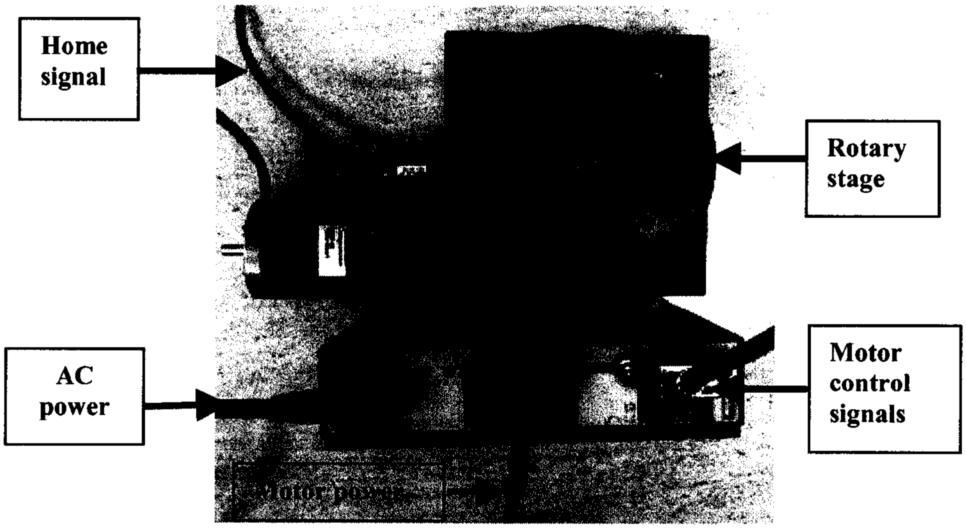

Figure 3.15: Photograph of motor driver and the bench-top showing control and power signals.

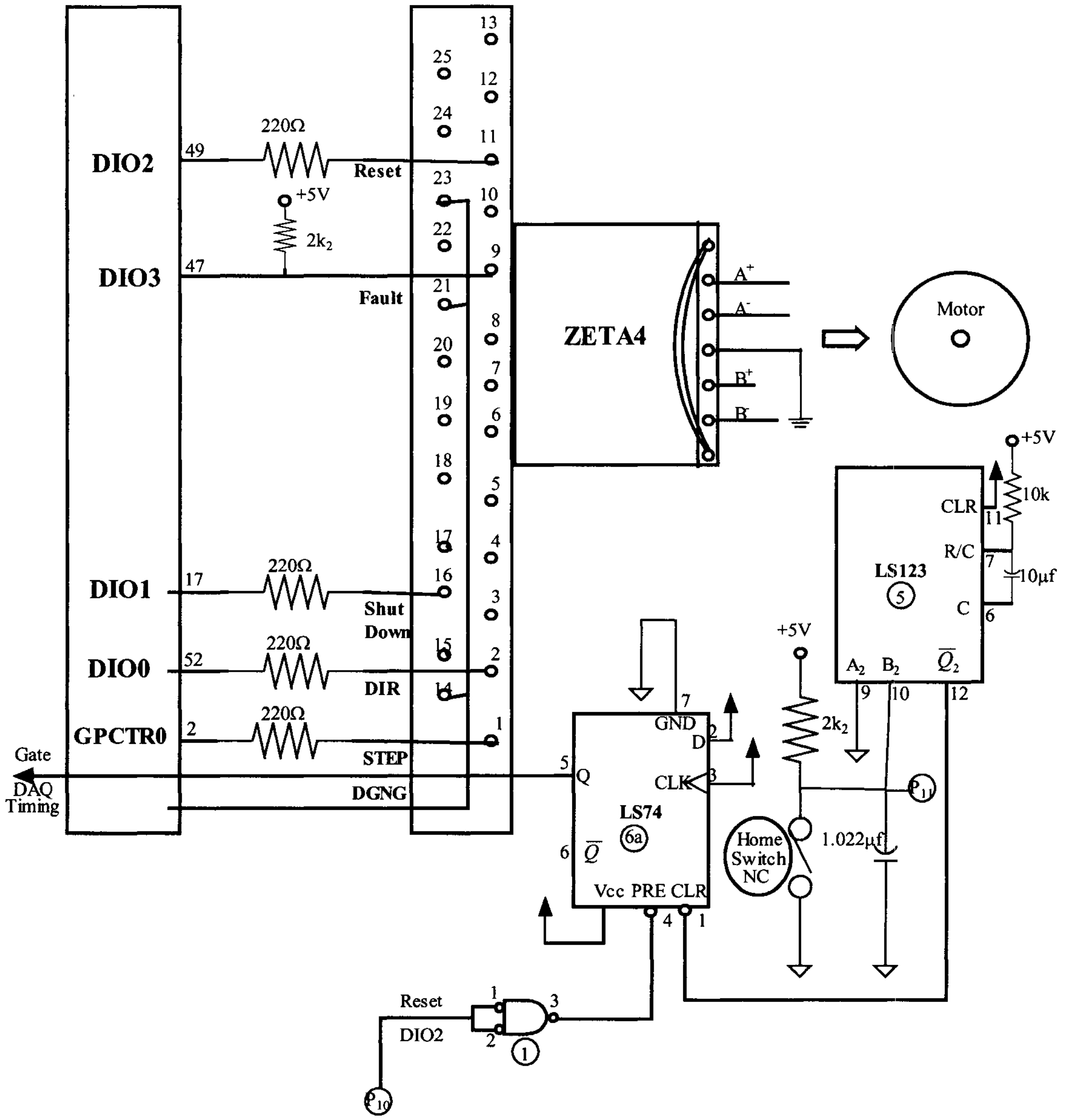

Figure 3.16: The motor control signal and the home switch. The signals DIO0-DIO3 and GPCTRO are generated by the data acquisition board to control the direction and speed of motor rotation. As the motor passes through the zero-position, the home-switch signals to open the gate for the data collection.

3.3.5 Data Acquisition Board

The data acquisition board, which is located in the computer, is used to convert the collected analog data from the 80:1 multiplexed line into a digital format. The conversion takes place at every clock pulse in the "Ext Conv" signal generated by the timing control board. In each read cycle, initiated by the "Sync" trigger from linear accelerator or internal sync for the continuous radiation, "Ext Conv" signal contains 80 pulses. The data conversion occurs in 16-bit and at the rate of 20 kHz. The digital output port (NI 6034E user manual, National Instruments, Austin, USA) and the programmable counter output of the data acquisition board are used to provide the direction, speed and on/off control to the motor as described in the previous section. The software user interface and the control is written in the LabVIEW programming language.

3.4 The LabVIEW Graphic Program

LabVIEW is a graphical development software for test, measurement, and control. It delivers a powerful graphical development environment for signal acquisition, measurement analysis, and data presentation, giving the flexibility of a programming language without the complexity of traditional development tools [LabVIEW user manual, 2000]. The main characteristic of LabVIEW programming is using icons, in contrast with other languages such as C and FORTRAN that are characterized by instructions in a simple plain text. Therefore, LabVIEW has some advantages: such as the program can be made very quickly and without much debugging, analog to digital conversation is made easy, etc.

Each LabVIEW program at least contains two components: a front panel that serves as the user interface and a block diagram that contains the graphical source code which defines the functionality of the program.

3.4.1 The Front Panel of our Bench-top MVCT System

The main functions of our LabVIEW program are to monitor the signals received from the detectors, save the sorted data into a file and control the motor movement. Figure 3.17 is part of the front panel of our bench-top MVCT system. The graph shows the signal from one 8-element array detector for each pulse (converted to time scale). The irregularly spaced pulses that do not produce radiation in normal clinical mode of linear accelerator are clearly visible. Below each graph, the mean and standard deviation of data for each of 8 detectors (only two are shown) are displayed during the collection period that helps in identifying dead or noisy detectors. The complete front panel contains 10 such graphs one each for ten 8-element boards.

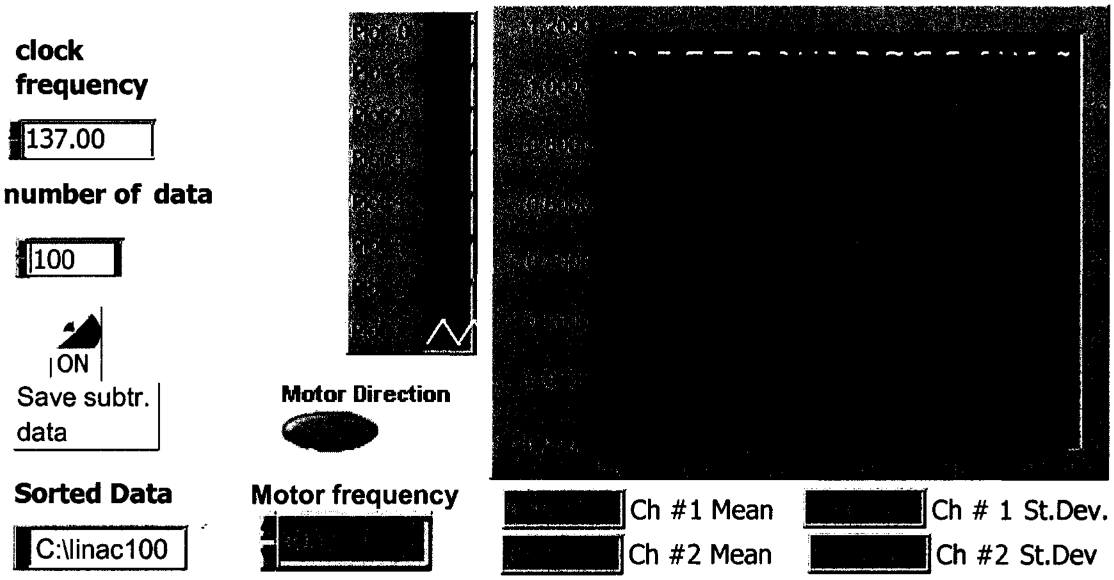

clock frequency: 137.00

number of data: 100

Sorted Data: C:\linac100

Figure 3.17: The main parts of front panel of LabVIEW code for the MVCT system.

At the left top, the "clock frequency" is the sync frequency of linear accelerator or the frequency of the trigger pulse for the continuous radiation. Below it, the "number of data" tells the program how many points will be collected for each detector during a run. Therefore, the total data collected during a run is 80 times this number. Below the "number of data" is the "ON" or "OFF" button to tell the program whether to save the sorted data as the file name shown just below this button. On the right side of this button, the "Motor direction" button can control motor rotated direction. Below this "Motor direction" is the "Motor frequency", f_{motor}, which controls the speed of motor movement. The stepper motor completes one revolution in 25,000 steps. The gear ratio of 90:1 is fixed between the motor and stage. Therefore, time for one revolution of the stage (scan time) is given by (25,000 x90/ f_{motor}). The scan time of 22.5 seconds results for a motor frequency of 100 kHz.

3.4.2 The LabVIEW Block Diagram of our Bench-top MVCT System

After designing the front panel, we need to design the block diagram to perform tasks as per the inputs and outputs on the front panel. Therefore, the block diagram actually is the main part of the programming. Our block diagram contains 13 frames and some of the frames also contain several sub-frames. Thus it is difficult to show the functionality of all of these frames. Figure 3.18 shows the flow chart that is followed by block diagram design. At first, we need to initialize all variables, and make the DAQ board ready to collect the data. Then we will check if the motor status is ready for move or not. If motor is not ready, then reset the motor; if the motor is ready, then start the motor with a specified speed. For each trigger pulse, the sample-and-hold and "ExtConv" pulses are only generated after the motor has reached home that signals the beginning of data collection. After the data collection is finished, the motor rotation is stopped. Therefore, the number of data points collected determines the time when the scan is finished. The collected data is then sorted into (80 x n) matrix and displayed on the graphs shown on the front panel. Mean and standard deviation of each detector channel is also calculated and displayed.

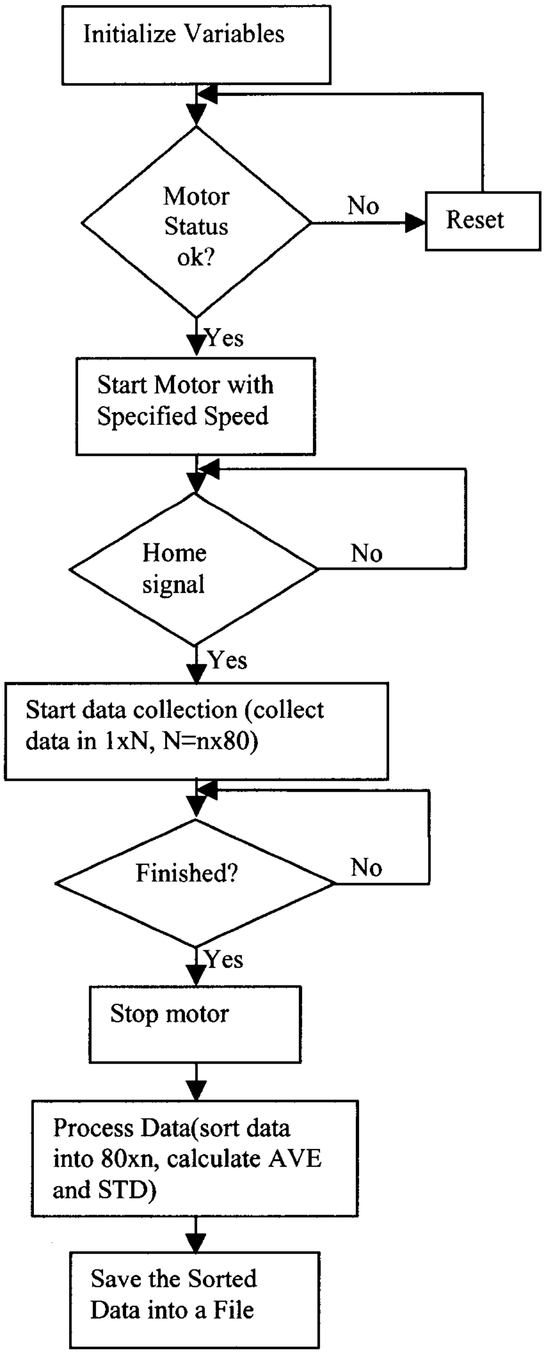

Figure 3.18: Flow chart of the block diagram for MVCT system.

3.5 Dose Response and Beam Attenuation Characteristics of the $CdWO_4$ Detector

The detector array made from $CdWO_4$ was used to test the detector's response to dose rate. The same detector was also used to measure the attenuation of 6 MV photon beam by solid water. The linear dose response and the accuracy of attenuation measurements are desirable properties of a CT detector.

3.5.1 Detector Dose Response

This experiment was designed to test the response of the detector with respect to dose in a 30.0 x 2.2 cm^2 6 MV photon beam (600C, Varian Medical System, Palo Alto, CA). The source to detector distance (SDD) was varied from 100 cm to 150 cm in 5 cm steps in order to vary the dose rate. A total of 2000 data points were collected at each SDD. Every measured data point corresponds to the sync pulses from the linear accelerator at a sync frequency of 137 Hz. The data points corresponding to sync pulses that did not produce radiation were discarded. The mean detector signal over the remaining points minus the dark current was taken as the detector signal at each SDD. The signal is then plotted against $(100/SDD)^2$. According to inverse square law [Khan, 1984], the dose is proportional to $(100/SDD)^2$. Therefore, the graph for signal vs. $(100/SDD)^2$ is actually the signal vs. dose, representing the detector's dose response.

The experimental set up for the detector dose response is shown in Figure 3.19.

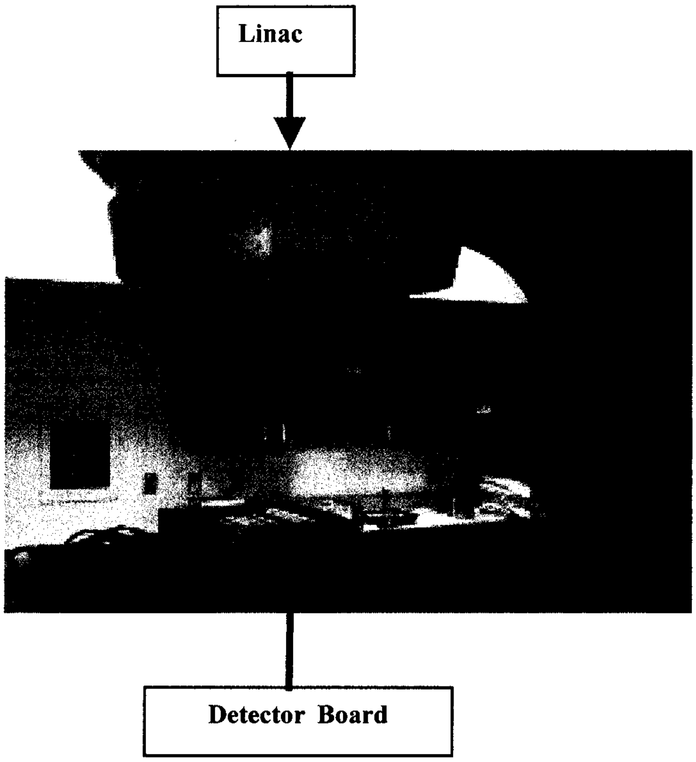

Figure 3.19: Experiment set up for detector dose response.

3.5.2 Measurements of Beam Attenuation

The linear beam attenuation measurement is the basis for the CT image reconstruction. Let us assume that a mono energetic beam passes through an object with linear attenuation coefficient distribution μ(x,y), and let I_0 and I be the incident and transmitted x-ray fluences, respectively. The transmitted and incident fluences are related according to the Beer's law [John and Cunningham, 1983]:

$$I = I_0 e^{-\int \mu(x,y) dl} \tag{3.6}$$

where the integration occurs along the path of the ray '*l*' through the object.

Equation (3.6) can be transformed into the following equation.

$$\ln(I_0 / I) = \int \mu(x,y) dl \tag{3.7}$$

The reconstruction process creates an image that is a map of the x ray attenuation coefficients of the tissue in the plane under examination by mathematical inversion of Eq. (3.7). Thus the fundamental objective of CT detectors is to measure the attenuation of the beam by the scanned object in an accurate and linear manner. For this purpose, a second experiment was designed to study the attenuation of photon beam by solid water using the 80-element $CdWO_4$ array. Slabs of solid water (12 slabs each 2 cm thick) were placed in the path of a narrowly collimated photon beam (25 x 2.2 cm^2) on top of the treatment couch while the detector was placed under the treatment couch at a SDD of 127 cm. The source to couch top distance was 100 cm. For each thickness of solid water, one thousand readings were taken, and the whole experiment was repeated 5 times. The corresponding dark current was subtracted from the mean of 1000 points for each solid water thickness. The data points corresponding to sync pulses that did not produce radiation were discarded. The attenuation factor for each solid water thickness was then calculated using the relation: Attenuation = Ln (Open signal/Attenuated signal).

The set-up for this experiment is shown in Figure 3.20.

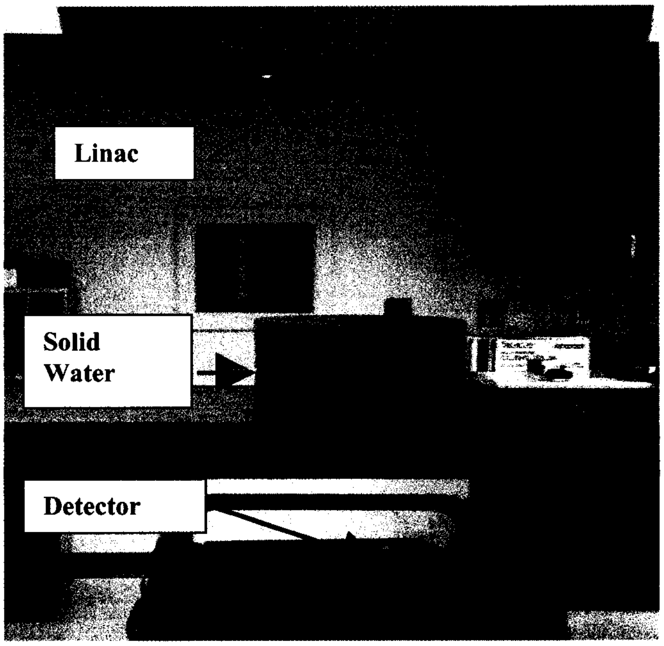

Figure 3.20: Experiment set up for beam attenuation measurement.

3.6 Imaging Characteristics Studies Performed on the CdWO$_4$ Detector Array

In the research environment, the detective quantum efficiency (DQE) is the standard by which the performance of x-ray imaging systems is measured [Bushberg, et al. 2002]. According to I. A. Cunningham [2000], DQE can be calculated as:

$$DQE(f) = \frac{MTF^2(f)}{(NPS(f)/\overline{S}^2)\varphi} \tag{3.8}$$

Here φ is the photon fluence impinging on the detector and $\overline{S}$ is the average detector signal. $MTF(f)$ is the modulation transfer function which describes how well an imaging system processes signal and $NPS(f)$ is the noise power spectrum which describes how well an imaging system processes noise in the image. Therefore, in order to calculate the $DQE(f)$, we need to measure the $MTF(f)$ and $NPS(f)$ for the 80-element array.

3.6.1 Modulation Transfer Function

Modulation transfer function is defined as the ratio of modulation of output signal to the modulation of input signal [I. A. Cunningham, 2000]. Thus MTF illustrates the fraction of the input signal's contrast recorded by the imaging system as a function of the spatial frequency of the signal and it is a very complete description of the spatial resolution of the system [Bushberg, et al. 2002].

It is not easy to measure the MTF(f) experimentally because we are unable to produce sinusoidal variations of x-ray fluence at a variety of spatial frequencies [John and Cunningham, 1983]. Although there are several indirect methods to measure the MTF(f), we here only use the line spread function (LSF) method to measure the MTF(f).

To measure the LSF, we used a very narrow slit beam of radiation. In our experiments, we set the slit width as 0.2 mm by using two 25 cm x 5 cm x 10 cm lead blocks. The slit beam was centered on 39th detector and 10,000 readings for each detector were taken. The detector data was corrected for the detector to detector sensitivity variations that were calculated from the open beam data measured in previous experiments. The corrected readings were averaged and dark current was subtracted to provide the LSF. See Figure 3.21 for the experiment set up for the measurement of LSF.

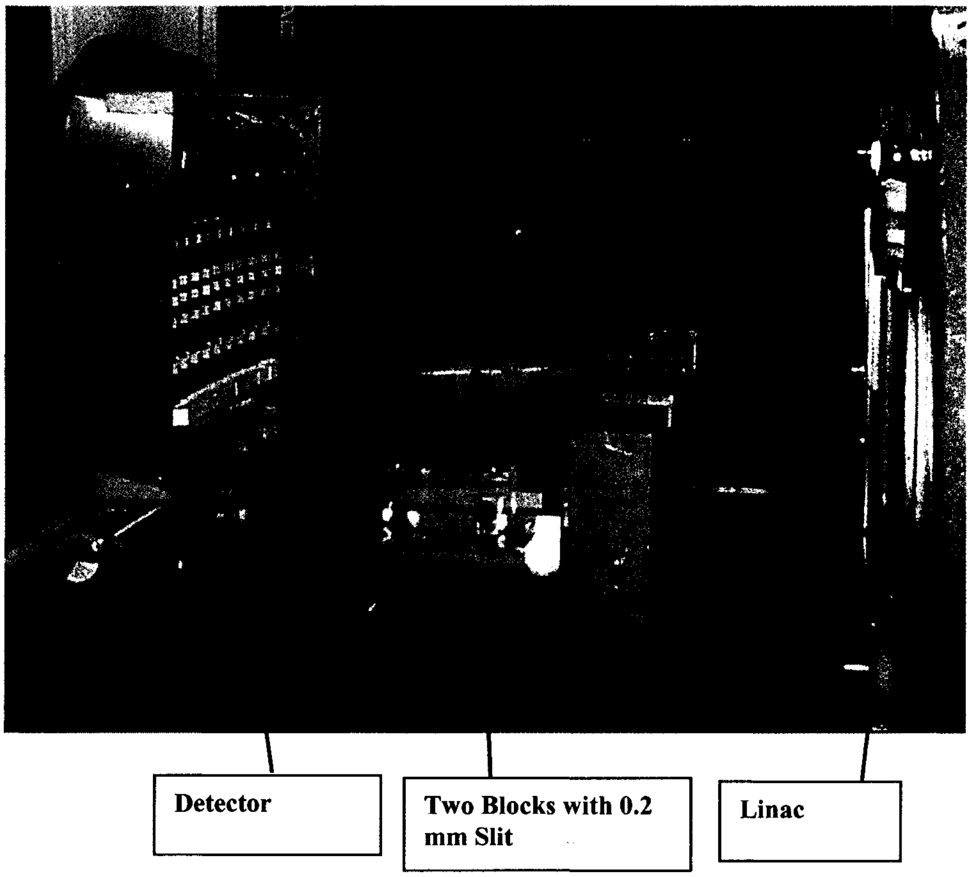

Figure 3.21: The experiment set up for the LSF measurement. The slit was centered on the 39th crystal, field size = 4 x 4 cm^2, SDD = 110 cm. Slit width = 0.2 mm.

When the LSF is measured, the MTF can be computed directly from it using the Fourier transform:

$$MTF(f_S) = |FT\{LSF(x)\}|, \qquad f_S(cycles/mm) = n/(3.15\times 80), n = 0,1,...,40 \qquad (3.9)$$

This was calculated using fast Fourier transform (FFT) method available in MATLAB (MATLAB 6.5.1, Mathworks, USA).

It should be noted that the spacing between detector elements for our array is large (0.315 cm). The main contribution to the spatial spread of the signal in this array is given by the Compton scattered photons from one detector element to another [Monajemi thesis, 2004] because the spread of optical photons is limited by the use of reflective coating on the crystals. At MV photon energies, the Compton scattering is relatively forward peaked. As a result, the pre-sampled LSF is very narrow and it will be significantly aliased if sampled with the large detector spacing. The aliasing is explained in the following paragraphs.

Considering a continuous function $f(x)$ which is sampled at a finite number of spatial locations, the resulting sampled-data may or may not represent the function correctly. Let $F(u)$ be the Fourier transform of the $f(x)$, $F_S(u)$ be the Fourier transform of the sampled data $f_S(x)$, and d be the sampling distance which usually is the detector pitch. According the sampling theory [Barrett, et al. 1981 and I. A. Cunningham, 2000], the sampled data $f_S(x)$ can be expressed as

$$f_S(x) = f(x)\sum_{n=-\infty}^{n=\infty}\delta(x-nd) \qquad (3.10)$$

Since multiplication in the x domain corresponds to convolution in the u domain, therefore, the Fourier transform of Equation of (3.10) becomes

$$F_S(u) = F(u) * \frac{1}{d}\sum_{n=-\infty}^{n=\infty}\delta(u-\frac{n}{d}) = \frac{1}{d}\sum_{n=-\infty}^{n=\infty}F(u-\frac{n}{d}), \qquad (3.11)$$

where $1/d$ is the sampling frequency.

Equation (3.11) indicates that the discrete Fourier transform is the summation of infinite number of shifted continuous Fourier transforms scaled by $1/d$. The scaled continuous Fourier transform $\frac{F(u)}{d}$ is shifted at the regular intervals spaced at integer multiples of the sampling frequency $1/d$.

Those shifted replications of $\frac{F(u)}{d}$ might or might not overlap each other. When overlap happens, it is called aliasing due to the under-sampling in the linear coordinates. When aliasing has occurred, the true Fourier transform $F(u)$ cannot be determined from the discrete Fourier transform $F_S(u)$. In other word, the original function $f(x)$ cannot be determined from the sampled data $f_S(x)$ when aliasing has occurred. [I. A. Cunningham, 2000].

The aliasing can only be avoided when there is no overlap between the replication of the continuous Fourier transform. If the continuous Fourier transform is a a bandlimited function,

$$F(u) = 0 \qquad |u| \geq 1/2d, \qquad (3.12)$$

then there is no overlap between the replications of the continuous Fourier transform. In other words, if the maximum spatial frequency presented in the data is less than half the sampling frequency, the aliasing errors can be avoided. It can also be stated that the spacing between samples in digital data determines the highest frequency that can be imaged. This limitation is called the Nyquist criterion and the frequency is called Nyquist frequency. Therefore the Nyquist frequency is given by:

$$f_N = 1/2d \qquad (3.13)$$

In general, the continuous Fourier transform of the finite size objects extends up to ±∞. Similarly, the sharp drop in the continuous LSF produces higher spatial frequency components in the Fourier transform of continuous LSF. Therefore, aliasing in the MTF cannot be completely avoided. But the aliasing errors can be reduced by the pre-sampled method through reducing the effective sampling distance. The procedure to measure the pre-sampled LSF is depicted in Figure 3.22. A slit beam was set at 5 equi-spaced positions within a single detector. At first a slit beam was centered on one of the detector elements (indicated by co-ordinate '0' in Figure 3.22) and an average signal for each detector element for 10,000 pulses was obtained. Then the detector array was translated on a manually operated translation stage at four other positions indicated by -2δ, -δ, δ and 2δ (δ = Δx/5, Δx is the detector pitch of 3.15 mm) with respect to the slit beam location. The average signal of detector element for 10,000 radiation pulses was obtained at each translated position. The average signals for the detector array from five translated positions (i.e. -2δ, -δ, 0, δ, 2δ) were interlaced to give the pre-sampled LSF. In this way, the effective sampling distance is reduced to one-fifth of the detector pitch and the aliasing errors can be greatly reduced.

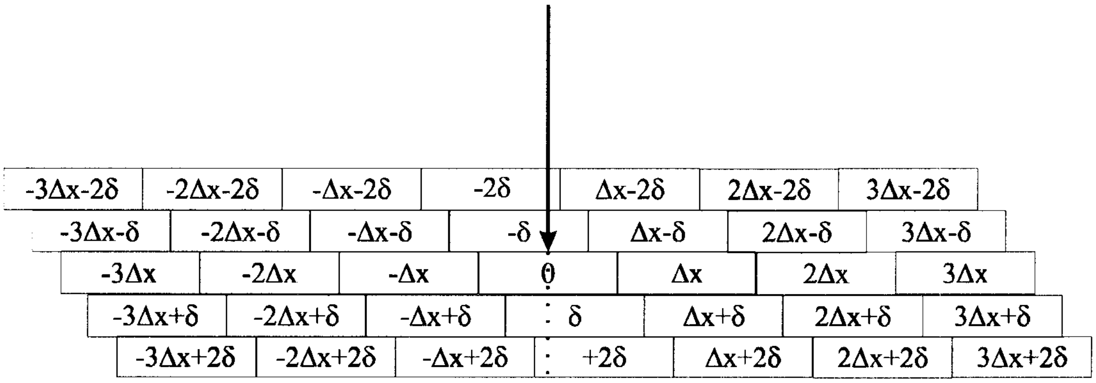

Figure 3.22: Arrangement of the slit beam and the detector array in the measurement of the pre-sampled LSF. Δx = detector aperture (3.15 mm), δ = resolution of detector translation with respect to the slit beam (0.63 mm).

3.6.2 Noise Power Spectrum

The main source of noise in detector readings is the statistical fluctuation caused by the random detection process. At diagnostic energies, where every interacting photon deposits almost all of its energy within the detector, the incident photon fluence and the quantum efficiency determine the noise in the detector signal. Since the photons scattered in one detector element rarely make to its neighbours, the noise power spectrum is white and the noise can be completely described by the variance. At MV photon energies, different interacting photons within the detector deposit different amount of energy to the detector determined by the Klein-Nishina relationship. Moreover, the photons scattered from detector element may reach its neighbours producing spatial correlation in the statistical fluctuations of detector signal [John and Cunningham, 1983]. Therefore, the noise is neither white nor is it completely specified by the incident photon fluence and the quantum efficiency. In order to describe the noise in our detector, we measured the NPS.

The experimental set up for the NPS measurement is almost the same as for the measurement of detector's dose response, see Figure 3.19 for reference.

We used a 32 x 2.5 cm^2 open beam with SDD of 110 cm. The data for 10,000 pulses was recorded, and the data collection was repeated 10 times. To calculate the NPS, we used a MATLAB code to process the recorded data. First, the 80-element data was corrected by subtracting mean dark current, deleting the non-radiation pulses and dividing by the mean values which contain the effects of variation in detector sensitivity and beam profile. Then for each pulse, i, the 80-element data, S_i was divided into 5 spatial sub-groups k, each containing 16 detectors. The noise only data, ΔS_i, for each radiation pulse in each of the 5 sub-groups, was obtained by subtracting first 8-elements from the second 8-elements. The Fourier transform (*FT*) of the 8-point noise only data was performed to obtain one periodogram [Williams, et al. 1999]. Finally, the NPS was obtained by averaging these periodograms over sub-groups, k, and total number of radiation producing pulses, I:

$$\Delta S_i(1:8) = S_i(16k-15:16k-8) - S_i(16k-7:16k) \qquad 1 \le k \le 5, 1 \le i \le I \quad (3.14)$$

$$NPS(f_S) = \frac{1}{2 \cdot 5 \cdot I} \sum_{i=1}^{I} \left(\sum_{k=1}^{5} \left| FT(\Delta S_i)^2 \right| \right), \quad f_S = \frac{n}{8 \cdot 3.15}, \quad n = 0,1,2,3,4 \quad (3.15)$$

3.6.3 Detective Quantum Efficiency

As mentioned in the beginning of section 3.6, the DQE is the gold standard to evaluate the imaging quality for the imaging system. After measuring the MTF and NPS of our detector system, the average detectors signal $\overline{S}$ for a given incident fluence (φ) in equation (3.8) is required. In calculating the NPS data, we divided the corrected data by the mean value; therefore, the average signal $\overline{S}$ has already been normalized to one. The photon fluence impinging on the detector φ was obtained using the following method.

First, we need to know the fluence-to-dose conversion factor for 6 MV photon spectrum for the linear accelerator (Varian 600c). Lachaine, et al. [2001] used the EGSnrs Monte Carlo software to calculate the fluence-to-dose factor as F = 7.51×10^{-8} cGy.mm^2/photon for the 6 MV spectrum of this machine. This factor is reasonable compared to the estimated value of 8.35×10^{-8} cGy.mm^2/photon. The estimated value is calculated by taking the average energy of 6 MV photon beam as 2 MeV, then the fluence-to-dose factor is given by

$$F = \frac{D}{\varphi} = \overline{E}\left(\frac{\mu_{en}}{\rho}\right)_{water} = 2MeV \times 0.0261 cm^2/g = 8.35 \times 10^{-8} cGy \cdot mm^2/photon \quad (3.16)$$

Then the photon fluence φ can be obtained from the following equation:

$$\varphi = \frac{\dot{D}(Dose/pulse)}{F(Dose\,per\,unit\,fluence)} \quad (3.17)$$

Here, $\dot{D}$ is the dose for per radiation pulse that was calculated in following way.

The treatment beam is calibrated to deliver 1 cGy at a depth of d_{max} = 1.5 cm in water for a 10 x 10 cm^2 field size when the chamber is located at 100 cm from the source. A pinpoint chamber (N31006, PTW Freiburg) was placed at a depth of d_{max} = 1.5 cm in a solid water phantom at a distance of 100 cm from the source. The charge collected (x_0) by the chamber in a 10 x 10 cm^2 field was recorded as 100 MUs were delivered. The irradiation was repeated using a 2.5 cm x 32 cm field size and a source to chamber distance of 110 cm to replicate the irradiation condition of the NPS measurement. This provided another charge reading (x) from the chamber for 100 MUs. Therefore the dose delivered at a depth of maximum dose in the geometry of NPS measurements is given by the following equation.

$$D = 100cGy\frac{x}{x_0} \qquad (3.18)$$

In the second irradiation, the 80-element detector was also placed underneath the solid water phantom in order to count the mean number of irradiation producing pulses. In other words, the saved data from the detectors for 100 MU irradiation was analyzed to determine the number of pulses, N, that actually produced radiation. Therefore, the dose D obtained from equation (3.18) was divided by N to obtain the dose per pulse in the solid water phantom at a depth of maximum dose in the irradiation geometry of NPS measurement.

$$\dot{D} = \frac{D}{N} \qquad (3.19)$$

The dose per pulse from equation (3.19) and fluence to dose conversion factor determined by Lachaine et al [2001] were used to determine the incident fluence on the detector. As a result, the absolute value of the frequency dependent DQE was thus obtained from equation (3.8)

3.7 Sinogram and Image

A sinogram is a display of the collected projection data in Cartesian coordinates. In a fan-beam CT scanner (a third-generation scanner), the horizontal axis of the sinogram corresponds to the data acquired by all the detectors for a fixed projection angle (source rotation angle).

The experimental set up for sinogram measurement is the same as shown in Figure 3.2. The 6 MV linac beam is incident on the detectors from the right side of the rotary stage. The distances from the source to the center of rotation of the stage and detector arc were 97.5 cm and 110 cm respectively. The field size was set at 26 x 0.9 cm^2 at the isocenter. The data was corrected for dark current, element-to-element variation in sensitivity, incident beam profile, and beam hardening. While calculating the detector signal, I, we discarded non-radiation pulses out of 3082 collected for one rotation and then selected one data for 1° rotation increments. The detector signals in the sinogram measurement were normalized with respect to the open beam data (I_0) for each detector that provided (I_0/I) data. This operation corrected for both the detector sensitivity and incident beam profile. Preliminary sinogram data was then obtained by taking the natural log of (I_0/I) data. The second order polynomial obtained from the attenuation measurement experiment were used to correct for the beam hardening. For each detector and source angle, the second order polynomial coefficients were used to obtain equivalent solid water thickness from the preliminary sinogram data.

We measured sinogram data for various objects: a 2 mm lead wire; the uniform insert of CATPHAN500 phantom (Phantom Laboratories, Salem, NY); and a specially designed low contrast insert of the CATPHAN 500 phantom. This phantom contains inserts that are 15 cm in diameter. The specially designed low contrast insert contains plugs of various diameters in three groups with 3%, 2.5% and 1.5% contrasts. In each group, there are seven small cylinders with diameters of 20, 15, 8, 7, 6, 5 and 4 mm.

The sinogram data was then rebinned into the equivalent parallel beam geometry [Barret and Swindell, 1981]. A parallel beam filtered backprojection method was then used to reconstruct cross-sectional images. In all images, a Shepp-Logan [Shepp and Logan, 1974] filter function was used in the reconstruction process.

References

Barret H. and Swindell W., *Radiological Imaging: The Theory of Image Formation, Detection, and Processing* , (Academic Press, 1981).

Blasse G. and Grabmaier B. C., *Luminescent Materials* (Springer, Berlin,1994)

Berndt A. G., "A Fourth Generation 192IR Source-Based CT scanner for Brachytherapy", PhD thesis, University of Manitoba (2002).

Bushberg J. T., Seibert J. A., Leidholdt E. M., and Boone J. M., *The Essential Physics of Medical Imaging*, (Lippincott Williams & Wilkins, Philadelphia, 2002).

Cunningham I. A., *Applied Linear-Systems Theory*, Chapter 2, Handbook of Medical Imaging Vol 1, edited by Van Metter R. L. (SPIE Publications 2000).

Derenzo, S. and Moses W. W., " Experimental efforts and results in finding new heavy scintillators", *Proceedings of the CRYSTAL 2000 International Workshop on Heavy Scintillators for Scientific and Industrial Applications*, Chamonix, France, 125-135(1992).

Duclos S. J., "Scintillator phosphors for medical imaging," *The Electrochemical Society Interface*, 34-38 (1998).

Johns H. E. and Cunningham J. R., *The Physics of Radiology*, 4th ed. (Thomas, Springfield, IL, 1983).

Khan F., The Physics of Radiation Therapy, 2nd ed (Williams & Wilkins, Baltimore, 1994).

Kinolch D. R., Novak W., Raby P., and Toepke I., "New developments in Cadmium Tungstate", *IEEE Trans. Nucl. Sci.*, 41: pp .752-754 (1994).

Krus D. J., Novak W. P., and Perna L., " Precision linear and two-dimensional scintillation crystal arrays for x-ray and gamma ray imaging applications," Presented at *The SPIE International Symposium on Optical Science, Engineering and Instrumentation*, July 18-23, 1999, Hard X-ray, Gamma-Ray and Neutron Detector Physics (SPIE Vol. 3768).

LabVIEW User Manual, (National Instruments Corporation, Austin, 2000).

Lachaine M., Fourkal E., and Fallone B. G., "Detective quantum efficiency of a direct-detection active matrix flat panel imager at megavoltage energies", *Med. Phys.* 28: 1364-1372 (2001).

Monajemi T. T., Steciw S., Fallone B. G., and Rathee S., “Modeling scintillator-photodiodes as detectors for megavoltage CT,” *Med. Phy.* 31: 1225-1234 (2004).

Monajemi T. T., “Modeling scintillator-photodiodes for MVCT,” M.Sc. thesis, University of Alberta (2004).

Moron E. J., Swindell W., Lewis D. G., and Evans P. M., “A linear array, scintillation crystal-photodiode detector for megavoltage imaging,” *Med. Phys.* 18:681-691 (1990).

Mosleh-Shirazi M. A., Evans P. M., Swindell W., Webb S., and Partidge M., “ A cone-beam Megavoltage CT Scanner for Treatment Verification in Conformal Radiotherapy”, *Radiotherapy and Oncology*. 48: 319-328 (1998).

Rizzoni G., *Principles and Applications of Electrical Engineering,* 2rd ed. (IRWIN,1996).

Ruchala K. J., Olivera G. H., Schloesser E. A., and Mackie T. R., “ Megavoltage CT on a tomotherapy system,” *Phys. Med. Biol.* 44: 2597-2621 (1999).

Shepp L. A. and Logan B. F., “The Fourier reconstruction of a head section,” *IEEE Transactions on Nuclear Science* NS-21: 21-43 (1974).

van Eijk C. W. E., “ Inorganic scintillators in medical imaging,” *Phys. Med. Biol.* 47: R85-R106 (2002).

Vittori F., de Notaristefani F., Malatesta T., and Puertolas D., “A study on light collection of small scintillating crystals,” *Nuclear Instuments and Methods in Physics Research, Section A* 452: 245-251 (2000).

Williams M. B., Mangiafico P. A., and Simoni P. U., “Noise power spectra of images from digital mammography detectors”, *Med.Phys.*26: 1279-1293(1999).

www.bicron.com [Manufacturer of crystal used in this study]

www.hamamatsu.com [Manufacturer of the photodiodes used in this study]

Chapter 4: RESULTS AND DISCUSSION

This chapter presents and discusses the experimental results obtained by following the methods described in chapter 3. First, the results concerning the linearity of response to dose of the ($CdWO_4$) detector array and its ability to linearly measure the beam attenuation by solid water are presented. Also, the detector sensitivity and the amount of spectral hardening of a 6 MV beam (600C, Varian Oncology Systems) in solid water are presented. The second part presents the experimental results of the imaging characteristics of the detector array. In this section, the measured aliased and pre-sampled line spread functions (LSF), their corresponding modulation transfer functions (MTF(f)), noise power spectrum (NPS(f)), and detective quantum efficiency (DQE(f)) of the detector are given. The relationship between the pre-sampled and aliased LSFs is also described. The last part presents the measured sinograms of various phantoms and the reconstructed images of low contrast phantom in a 6 MV photon beam.

4.1 Linearity of the $CdWO_4$ Array Detector

A linear-system response is generally necessary before we use the linear-systems approach to analyze or characterize system performance [I. A. Cunningham, 2000]. Thus, if we want to use the linear-system approach to measure MTF(f), NPS(f) and DQE(f) for quantifying and analyzing the imaging characteristics of our system, we must ensure that the system is indeed linear. This means that for our detector system, the measured signal must be proportional to the input dose. Although the ideal linear system does not exist in reality, the assumption of linearity can be validated approximately within a certain range of incident dose for operational detector system or can be achieved with an appropriate calibration [I. A. Cunningham, 2000].

4.1.1 Detector Dose Response

Figure 4.1 shows mean signals of eight different detector elements, chosen at evenly spaced points within the array, as a function of inverse of the square of SDD. It can be safely assumed that the dose rate in free space of the 6 MV beam from the linear accelerator is linearly proportional to $(100/\text{SDD})^2$. It can be seen that the detector's response with $(100/\text{SDD})^2$ is quite linear. Therefore, the output signal of the detector is linearly proportional with respect to the input dose. The difference in the slopes of various linear regression lines is due to the element-to-element sensitivity variations and the photon beam profile. The photon beam after passing through the flattening filter used in a linear accelerator is not a perfectly flat beam; the on-axis radiation intensity is lower compared to that on the off-axis points. The measured beam profile at a depth of 1.5 cm in a water phantom of the 6 MV beam is shown in Figure 4.2. Therefore, it is necessary to perform the beam profile correction. This correction is division of the signal by the relative beam profile intensity. Figure 4.3 shows the detector signals as a function of $(100/\text{SDD})^2$ after applying the beam profile correction. Here, the difference in slope of various linear regression lines is mainly caused by the variation in element-to-element sensitivity of the detector elements. The variation in sensitivity among different detector channels is caused by various factors such as non-uniform optical glue, non-uniform optical yield (± 15% as per manufacturer), variations in optical sensitivity of photodiodes, radiation scattered from a crystal to its neighbors, etc. Generally speaking, for each 8-element detector array, the detector channels on the edges may have a slightly shallower slope than the inner channels as a result of decreased detection of lower energy scattered radiation from neighbors due to the air gaps. The relative detector sensitivities were calculated as the slope resulting from linear regression of mean detector signal and $(100/\text{SDD})^2$. The relative detector sensitivities, i.e. change in absolute detector signal per unit change in $(100/\text{SDD})^2$, of the 80-element array are shown in Table 4.1. A correction for the variation in the element-to-element sensitivity is automatically applied in the imaging application of this detector as the open beam signals are used to normalize the attenuated signals.

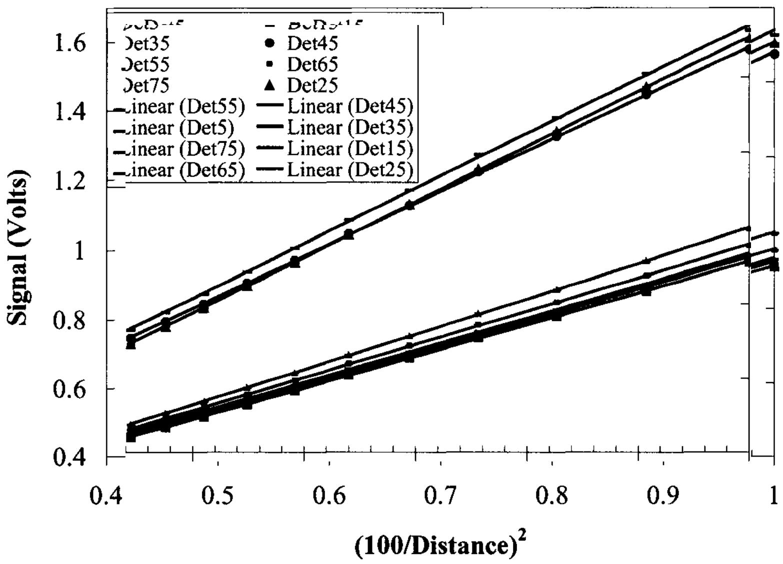

Figure 4.1: Detector signal as a function of the inverse-squared distance from source. Slope differences are due to the element-to-element sensitivity and the beam profile. The error in data points is smaller than the symbol.

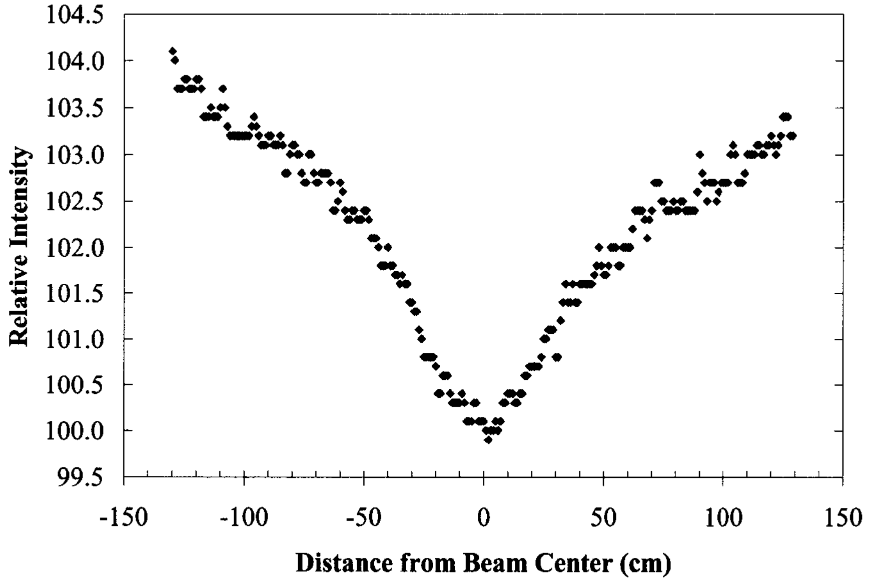

Figure 4.2: The 6 MV photon beam profile of Varian 600C at SDD = 100 cm and D_{max} =1.5 cm.

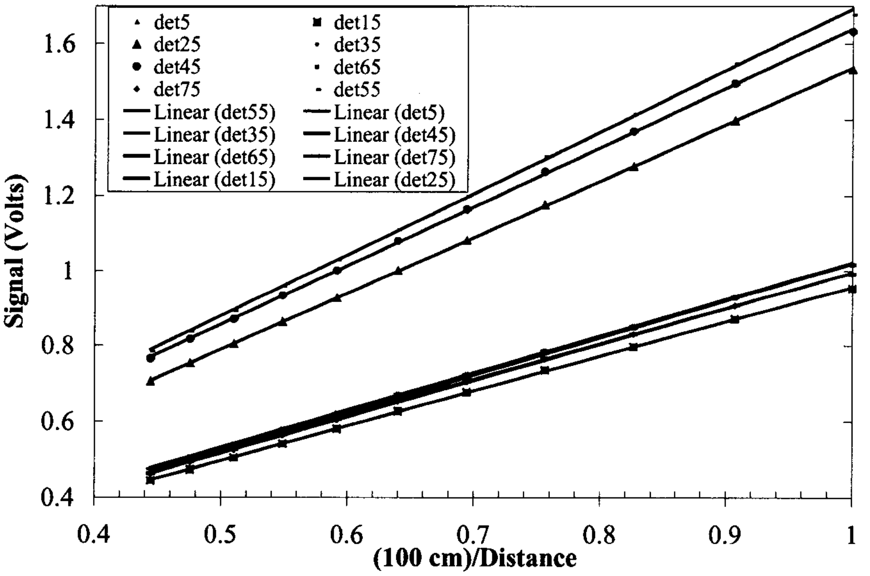

Figure 4.3: Detector signal as a function of distance from source after beam profile correction. The error in data points is smaller than the symbol.

Table 4.1: The relative detector sensitivity (signal per unit dose) of eighty-element array

Detector Array Number	*Detector Number in each Array*							
	1	2	3	4	5	6	7	8
1	0.4864	0.5546	0.5391	0.5854	0.5667	0.5503	0.5689	0.5099
2	0.5573	0.4991	0.5966	0.5215	0.5183	0.5159	0.5256	0.5763
3	0.9174	0.9189	0.8871	0.9118	0.8458	0.8551	0.9992	0.4173
4	0.8530	0.9068	0.9049	0.9094	0.9502	0.9417	0.9099	0.8327
5	0.5419	0.5744	0.5423	0.6134	0.6079	0.7404	0.8035	0.6205
6	0.6654	0.8788	0.8606	0.8885	0.8958	0.9040	0.9392	0.5083
7	0.5089	0.8268	0.9163	1.0000	0.9466	0.9085	0.9307	0.5509
8	0.4983	0.5212	0.5333	0.5186	0.5070	0.5088	0.5167	0.5066
9	0.5601	0.5813	0.5738	0.5570	0.5353	0.5582	0.5881	0.5592
10	0.4778	0.5943	0.5474	0.5189	0.5053	0.5355	0.5302	0.4714

4.1.2 Measurement of Beam Attenuation

The attenuation of 6 MV photon beam (Varian 600C) by solid water, calculated as the log of (open beam signal divided by the attenuated signal), is shown in Figure 4.4 as a function of the solid water thickness for all 80-elements in the detector array. The linear regression lines to the data from detector elements 1, 80 and 39 are also shown. The elements 1 and 80 are located off-axis while element 39 is located on central axis. We can see that the relationship between the attenuation and solid water thickness is nearly linear; the small yet important deviation from the linear relationship is explained in next paragraph. From Figure 4.4, we can see that the central detector-element has lower slope than the detector-elements located off-axis. These slightly different slopes for the different detector-elements are due to the differences in the photon beam spectra caused by the presence of the flattening filter. After the photon beam passes through the conical shaped flattening filter, more of the lower energy photons are filtered out at the central axis compared to the off-axis points. As a result, the flattened photon beam, in general, is more penetrating on the central axis than at off-axis points. Therefore, the central axis detector-elements (i.e. 39) correctly indicate the lower attenuation of the beam by the solid water compared to the off-axis detectors (i.e. 1 or 80).

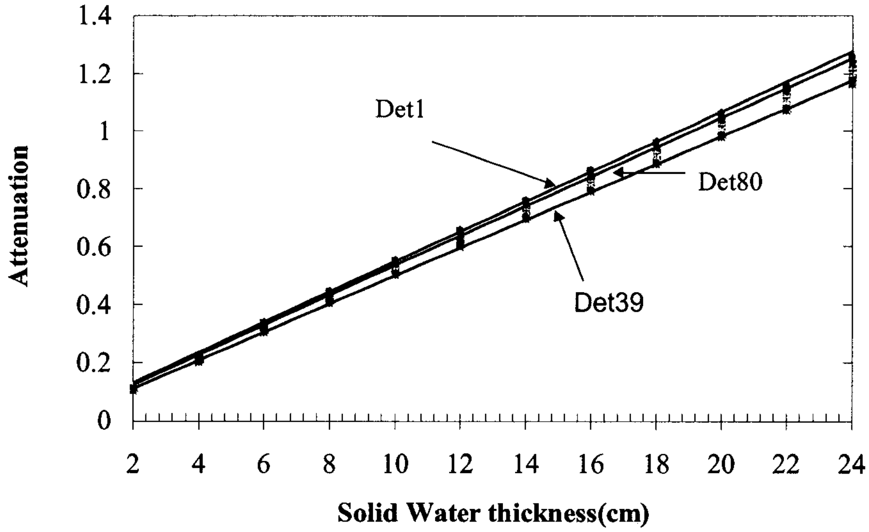

Figure 4.4: Measured attenuation as a function of solid water thickness using 80-element $CdWO_4$ crystal array. The data from 80-channels along with a linear fit to the data from elements 1, 39 and 80 are shown.

As noted above, the relationship between the measured attenuation and solid water thickness is not exactly linear. This is shown in Figure 4.5 that shows the linear regression line to the attenuation data measured by detector element 1 with a correlation coefficient $R^2 = 0.9983$ being less than unity. For smaller thickness of solid water, the data points are generally above the straight line and for the larger thickness of solid water, the data points are generally below the straight line. Although, the deviation from linearity is numerically small, its systematic nature may produce noticeable cupping artifact if the attenuation data is used for CT image reconstruction as such. These deviations can be explained by beam hardening. When the beam passes through the solid water, it becomes more energetic as the lower energy photons are preferentially attenuated. Since the attenuation per unit solid water thickness of the harder beam is lesser than the incident beam, the initial data points fall above and the final data points fall below the regression line in Figure 4.5.

A function of the form

$$-\ln[I(t)/I(0)] = \alpha t + \beta t^2 \qquad (4.1)$$

may better describe the relationship between the detected attenuation and the thickness (*t*) of any uniformly attenuating material such as solid water [Lewis et al., 1992]. In Eq. (4.1), I(*t*) is measured detector signal after the beam has passed through thickness '*t*' of solid water. It can be seen from Figure 4.6 that the second order polynomial better describes the measured attenuation as a function of the thickness of solid water with $R^2 = 1$. In general, due to the off-axis softening of the photon beam spectra, we found that the first order coefficient decreases near the central axis (i.e. detector element 39). Usually the second order coefficient β is much smaller than the first order coefficient α. From the data given in Figure 4.6 (element 1), we see that the second order coefficient β is only 0.35% of the first order coefficient α; however, at large solid water thickness, the non-linear component (second order part) is significantly large and cannot be ignored. For example, at 22 cm solid water thickness, the non-linear component is about 8.3% of the total measured attenuation by detector element 1. Figures 4.7 and 4.8 give the linear and second order polynomial fits for data points of element 39, respectively. We can see that the results are similar to element 1; however, the non-linear component of the total measured attenuation at 22 cm thickness is only 4.5%. For CT detector systems, the measured attenuation's linearity with respect to the thickness is the basis of reconstruction. Therefore, it is important to correct the measured signal of our system for beam hardening before image reconstruction.

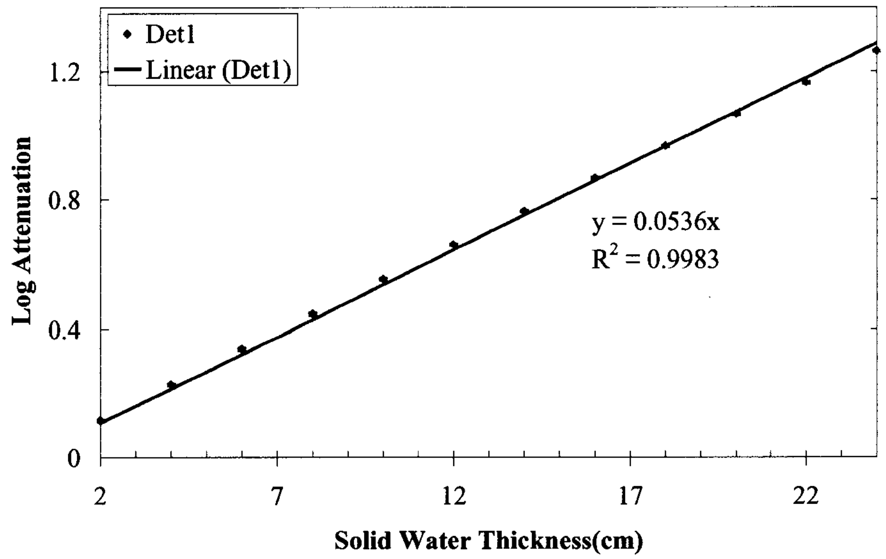

Figure 4.5: Linear fit to the attenuation data of detector 1. The error in data points is smaller than the symbol.

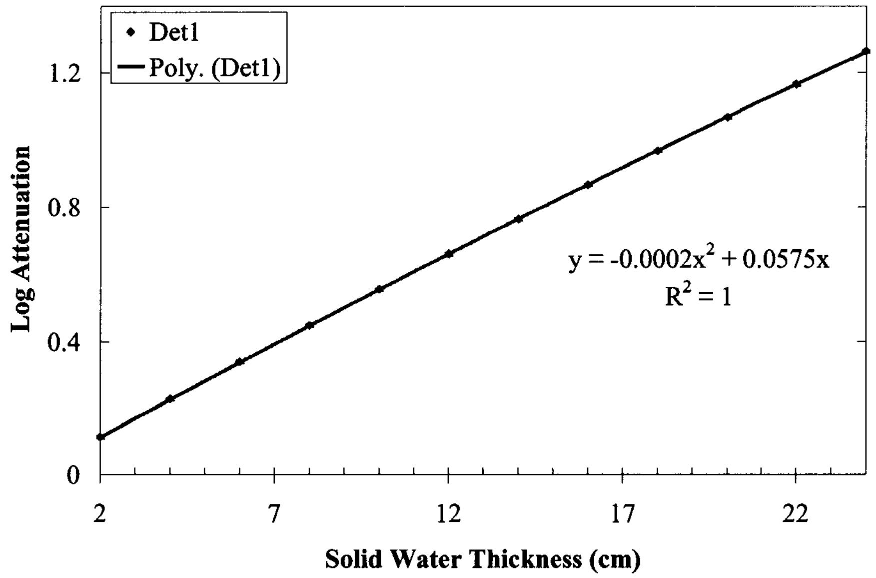

Figure 4.6: Second order polynomial fit to the attenuation data of detector 1. The error in data points is smaller than the symbol.

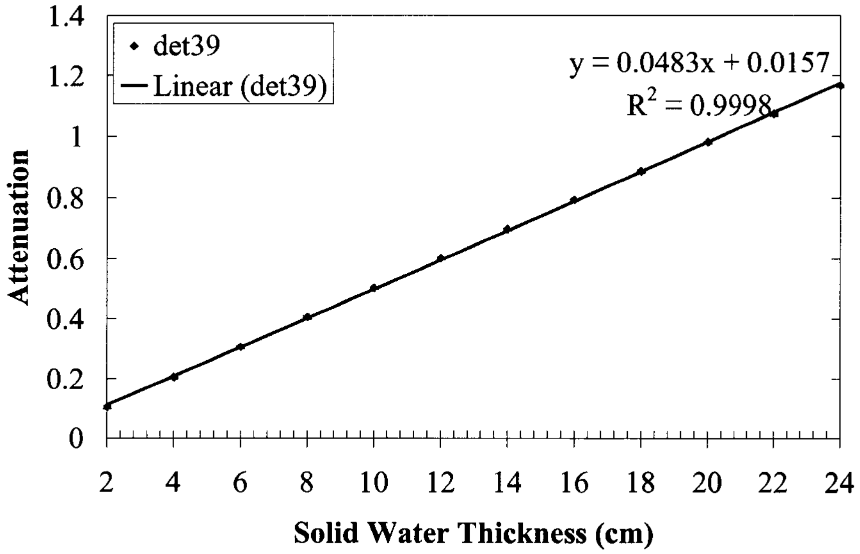

Figure 4.7: Linear fit to the attenuation data of detector 39. The error in data points is smaller than the symbol.

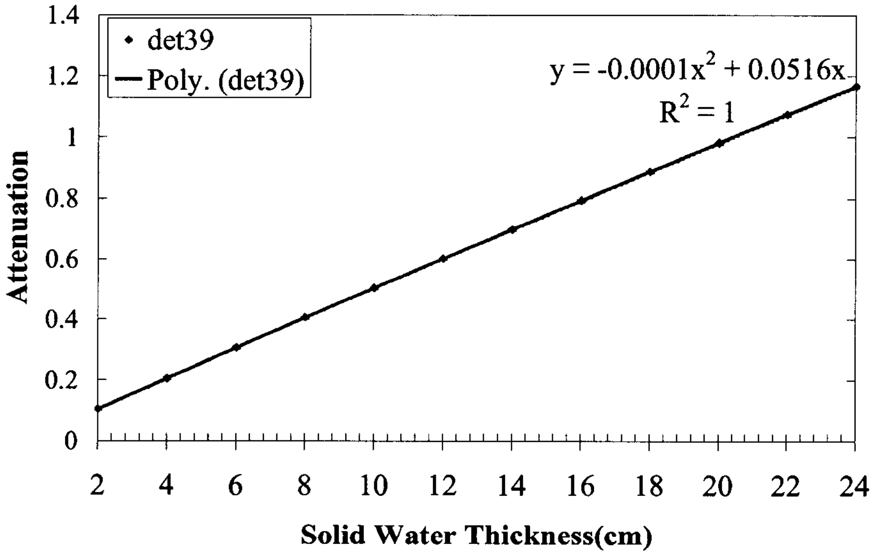

Figure 4.8: Second order polynomial fit to the attenuation data of detector 39. The error in data points is smaller than the symbol.

4.2 Imaging Characteristics of the $CdWO_4$ Array Detector

4.2.1 Line Spread Function and Modulation Transfer Function

The aliased LSF is measured by placing a slit beam at the center of detector element and recording the detector signal spreading in the neighboring elements. With a detector pitch of 3.15 mm, the Nyquist frequency is 0.16 cycles per mm. Figures 4.9 and 4.10 show the aliased LSF and the corresponding aliased MTF respectively. This MTF has a small reduction in its magnitude up to the Nyquist frequency due to the aliasing. A small dip in the MTF at the low frequency of 0.004 cycles/mm is also noticeable. This dip is caused by the leakage radiation from the treatment head. The two lead blocks used to form a slit beam are each 5 cm wide and 25 cm thick. Therefore, the detectors falling underneath the 5 cm width on either side of the slit beam will detect negligible leakage radiation. A 5 cm wide block will approximately cover 16 detector element on either side of the slit beam, thus detector elements 20 through 52 will not detect leakage radiation. We used additional blocks to remove the leakage radiation reaching the detector elements outside this range. However, the additional blocks were only 5 cm thick and do not completely remove the leakage radiation. This can be seen clearly in Figure 4.11, which is the same graph as Figure 4.9 except that the range of y-axis is reduced to highlight the small leakage signal. Therefore, for the purpose of MTF calculation, we can assume the data before detector 20 and after detector 52 is zero. Figure 4.12 shows the MTF taken after making this assumption that does not show the small dip in the magnitude of the MTF. Similar effect of leakage radiation is also seen in the pre-sampled LSF and MTF. Figure 4.13 shows the pre-sampled LSF obtained by placing the slit beam at five equi-spaced points within detector element 36 (the central data point at 178). In this experiment, the head leakage is detected before data point 98 (178 -16x5) and after data point 258 (178 + 16x5). This is indicated by magnifying the y-axis scale of the pre-sampled LSF in Figure 4.14. Figure 4.15 shows the pre-sampled MTF(f) including the gantry head leakage. Figure 4.16 shows the pre-sampled MTF excluding the gantry head leakage which only uses data points between 98 and 258 in pre-sampled LSF; the other data points are assumed to be zero. Therefore the small dip at very low frequency caused by the leakage radiation is removed in Figure 4.16.

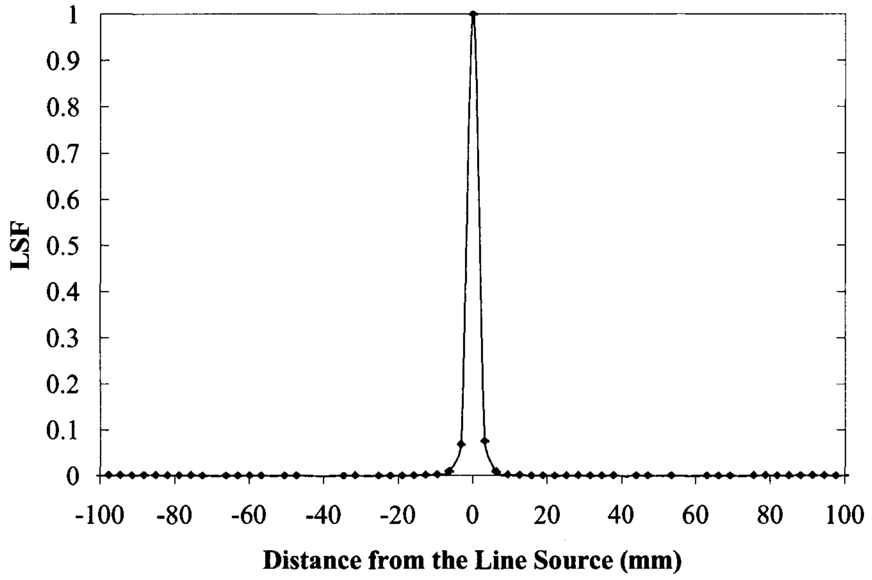

Figure 4.9: The aliased LSF with slit beam centered at detector element 36. The error in data points is smaller than the symbol.

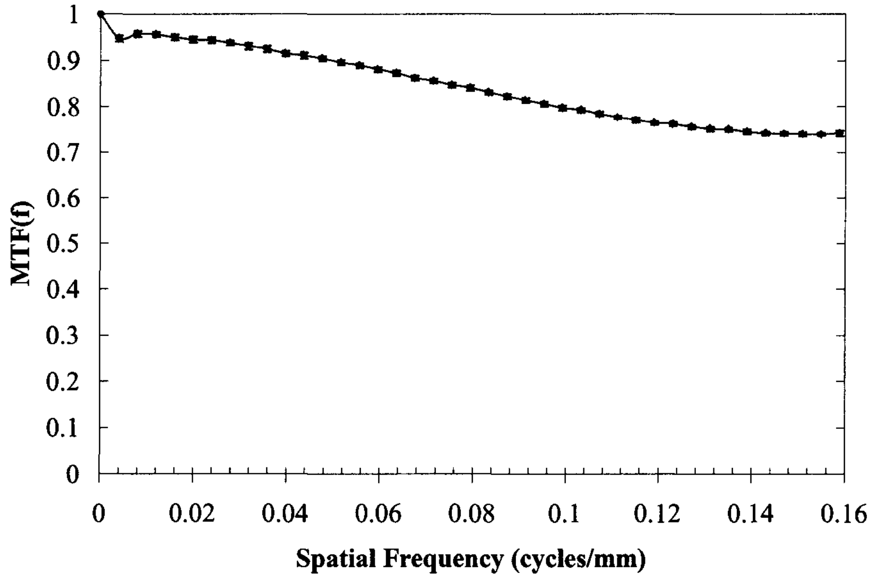

Figure 4.10: The aliased MTF, which is obtained from the corresponding aliased LSF of Figure 4.9. The small dip at 0.004 cycles/mm is due to leakage radiation as shown in Figure 4.11.

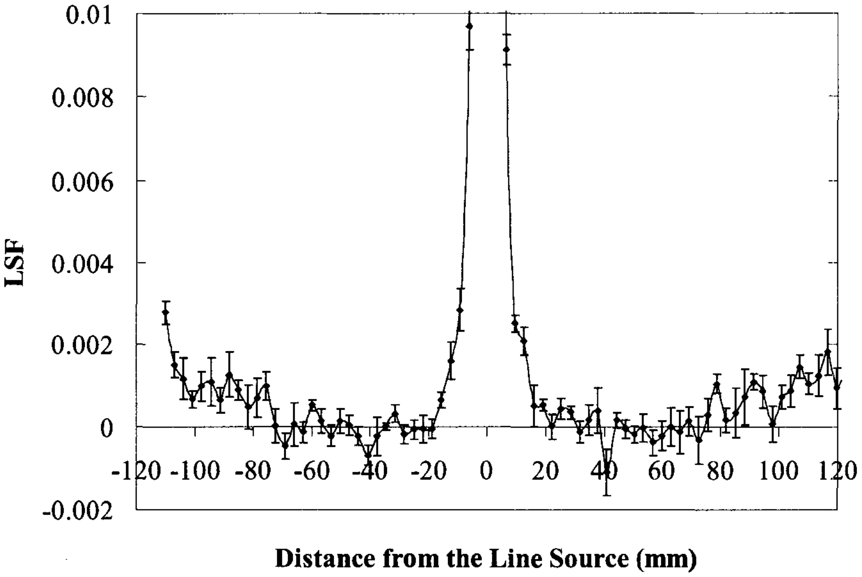

Figure 4.11: The same aliased LSF as Figure 4.9 except a much smaller y-axis range.

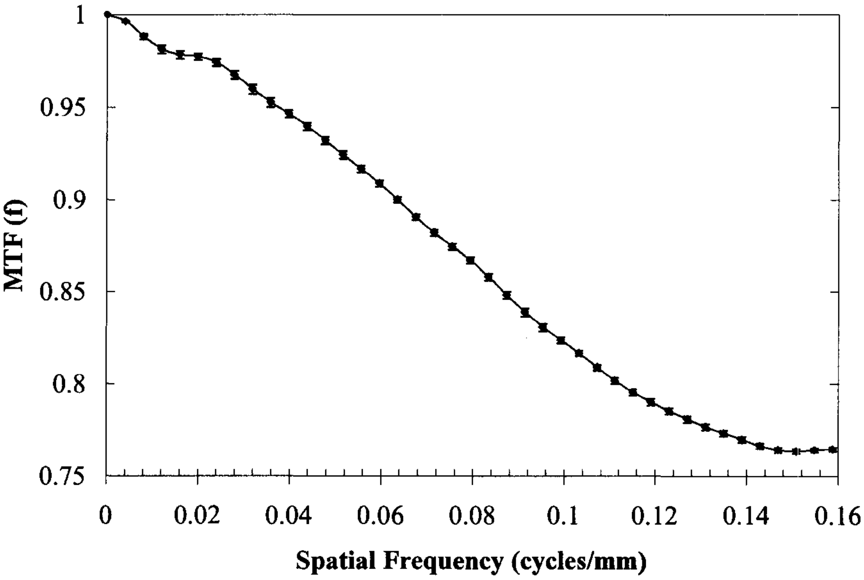

Figure 4.12: The same aliased MTF as Figure 4.10 after the head leakage is removed.

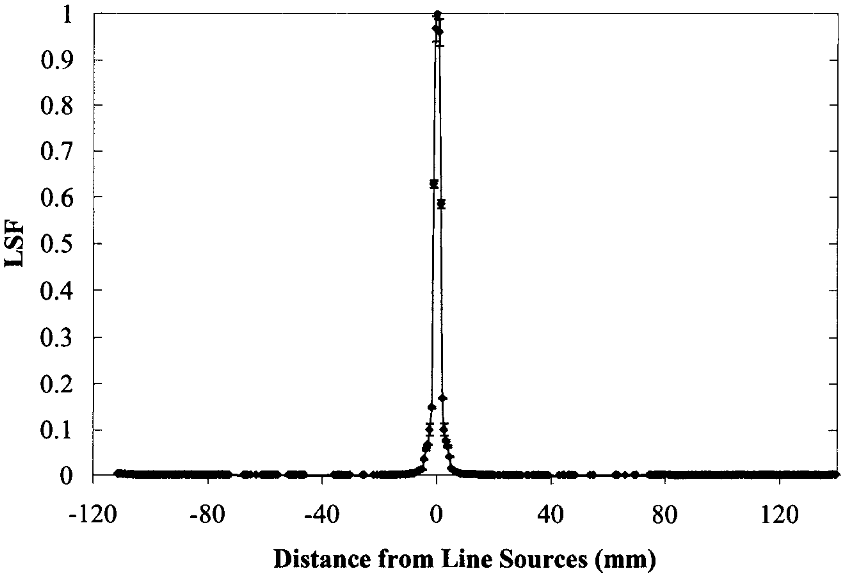

Figure 4.13: The pre-sampled LSF with slit beam at 5 equi-spaced positions within detector element 36.

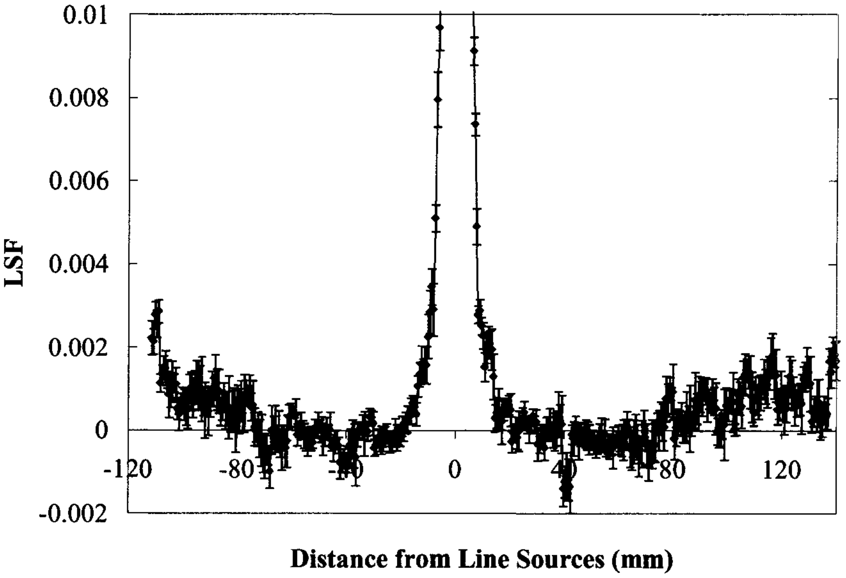

Figure 4.14: The same pre-sampled LSF as Figure 4.13 except a much smaller range in y-axis in order to show the leakage of the head.

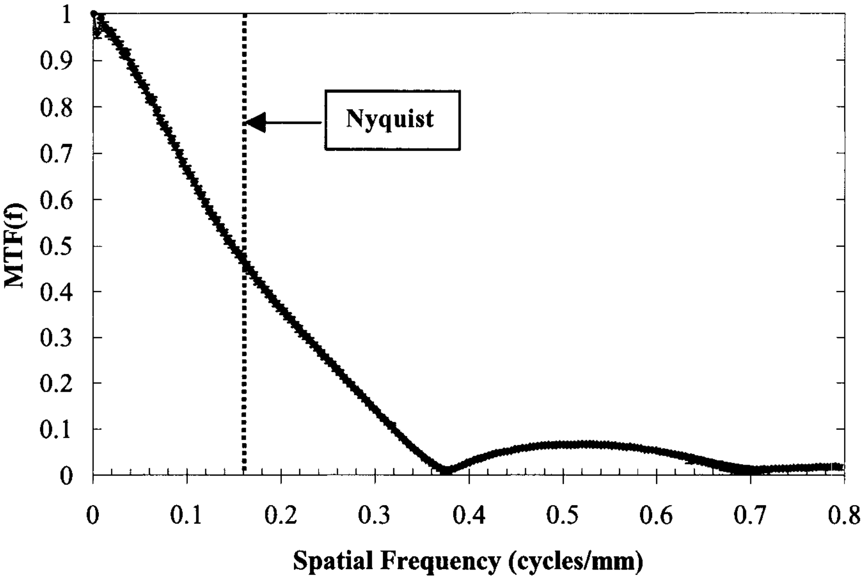

Figure 4.15: The pre-sampled MTF obtained from the corresponding pre-sampled LSF as shown in Figure 4.14. The small dip at 0.004 cycles per mm is due to the head leakage detected in data points prior to 98 and after 258 in the pre-sampled LSF.

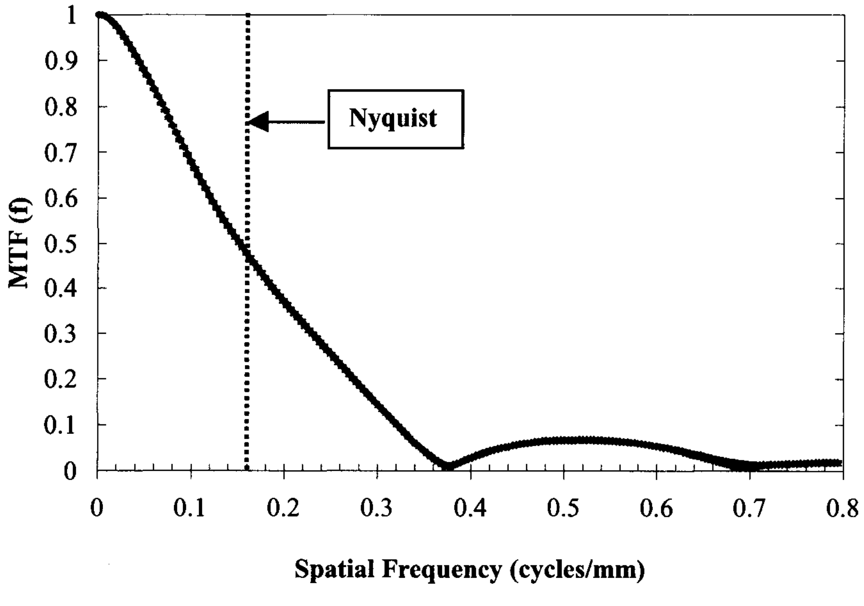

Figure 4.16: The same pre-sampled MTF as in Figure 4.15 after the head leakage is removed. The dip at 0.004 cycles/mm has been removed.

As noted earlier, the Nyquist frequency in the aliased MTF occurs at 0.16 cycles per mm i.e. at (1/3.15) x 0. 5. The effective Nyquist frequency in the pre-sampled MTF occurs at 0.8 cycles per mm. Figure 4.17 compares the aliased and pre-sampled MTF. The two important observations can be made from this comparison. The aliased MTF is significantly larger in magnitude than the pre-sampled MTF. The fact that the difference between the two MTFs is indeed due to aliasing is explained in the next paragraph. The second observation is that the pre-sampled MTF is dominated by the MTF of the aperture of a single element i.e. 2.75 mm wide $CdWO_4$ crystal. The approximate aperture MTF was calculated by dividing the 2.75 mm crystal into five 0.63 mm (3.15/5) wide segments. The middle three segments lie completely within the crystal width while two end segments are only partially filled by the crystal. Thus the detector aperture function contains five non-zero points out of total 400 points. The detector aperture MTF (Fourier Transform of the detector aperture function) is shown in Figure 4.18 along with the measured detector MTF. It can be seen that the behavior of the measured pre-sampled MTF is quite similar to the detector aperture MTF. The measured pre-sampled MTF was divided by the detector aperture MTF to obtain the MTF that is only affected by signal spread in a $CdWO_4$ crystal. This final MTF is also shown in Figure 4.18 as the crystal MTF. It should be noted that the division was not performed near the zero crossings of the original MTF to avoid the errors due to noise in the measured pre-sampled MTF. Also, the final MTF still contains the effect of the smaller (artificial) detector aperture of 0.63 width. Basically, the final MTF approximately provides the fundamental resolution limit in $CdWO_4$ crystal due to Compton scattering.

Aliasing occurs in a sampled function when there is overlap between the shifted versions of the Fourier transform of the underlying continuous function. Here, we can assume the pre-sampled MTF to be a continuous (relative to detector pitch of 3.15 mm) function and make this function symmetric about zero-frequency. Figure 4.21 shows this symmetric pre-sampled MTF and two of its replications at the sampling frequency for the aliased MTF i.e. at -0.32 and 0.32 cycles per mm. The curve designated as "sum" in this figure is obtained by adding overlapping points of the three replications of the pre-sampled MTF. The added function is then re-normalized to be unity at zero frequency to obtain the "normalized sum" MTF and compared to the measured aliased MTF within 0.0 to 0.16 cycles per mm frequency range. The measured aliased MTF is very similar to the "normalized sum" MTF within this frequency range. Therefore, the aliasing in the measured MTF is mainly caused by the small number of samples within the detector aperture. The small difference between "normalized sum" and measured aliased MTF will occur because the aforementioned analysis is based on the assumption that the basic signal spread is caused solely by the spatially invariant Compton scattering within the crystal array. Obviously, a small spread in the signal is also caused by the propagation of the optical photons that cannot be assumed to be spatially invariant due to the reflective coating on the crystal elements [Monajemi, 2004].

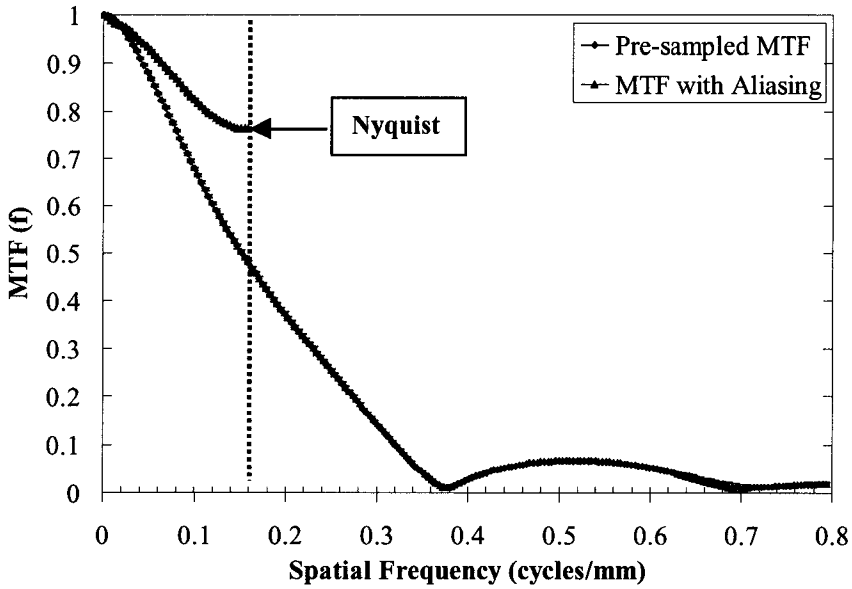

Figure 4.17: The comparison of aliased MTF with the pre-sampled MTF.

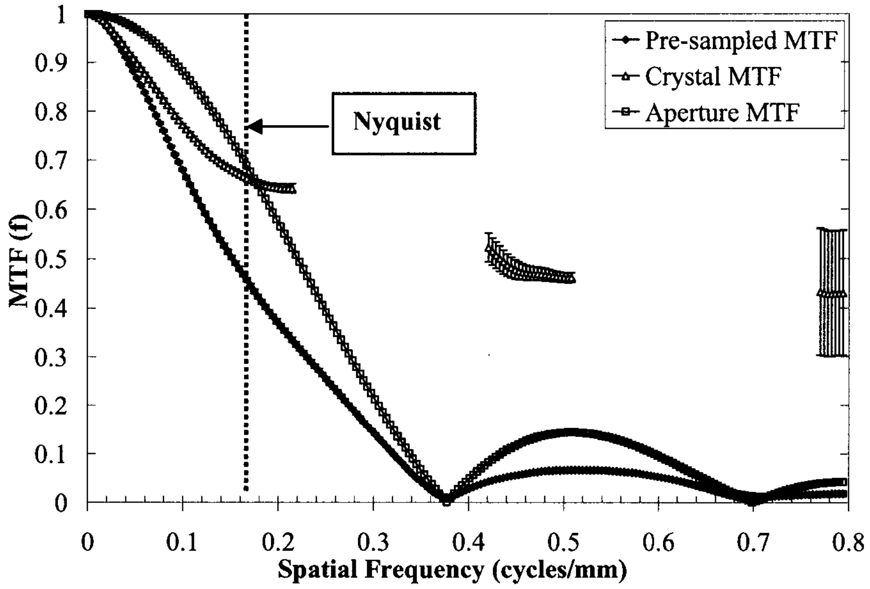

Figure 4.18: The Comparison of measured pre-sampled MTF, detector aperture MTF, and the crystal MTF due to Compton scattering.

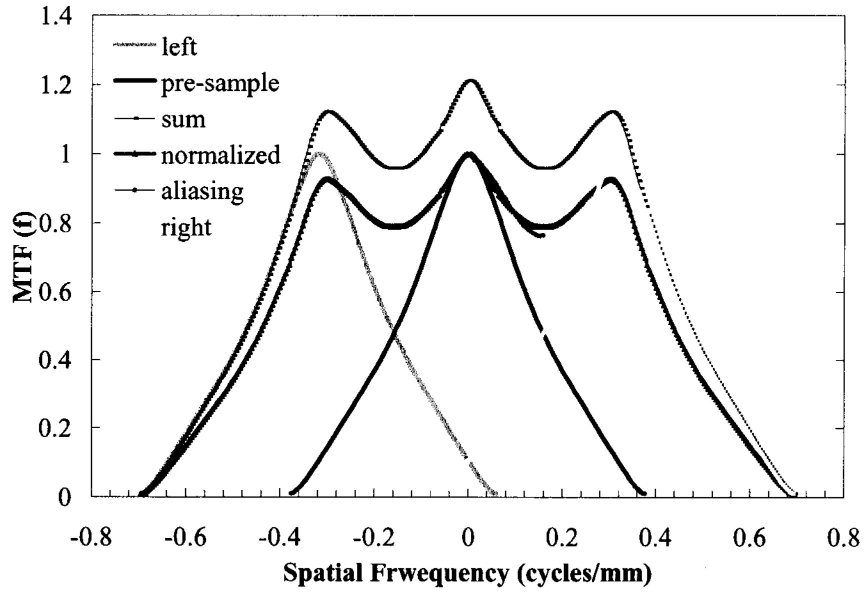

Figure 4.19: A simple diagram to show that the aliased MTF is the sum of the shifted versions of pre-sampled MTF where the replications of the pre-sampled MTF occur at the sampling frequency of the aliased MTF.

4.2.2 Noise Power Spectrum and Detective Quantum Efficiency

Figure 4.20 shows the NPS(f) of detector system using the average periodogram method described in section 3.6. We already know the MTF (f) and the average signal $\bar{S}$ (here it has been normalized to one), therefore, if we find the photon fluence, we can get the DQE (f) according equation (3.8). The photon fluence can be calculated by equation (3.17). Here, the fluence-to-dose factor was given as F = 7.51 x 10^{-8} cGy.mm^2/photon calculated by Lachaine et al. [2001] using the EGSnrs Monte Carlo software for Varian 6 MV spectrum. The charge collected by a pinpoint chamber was 1.80 when the chamber was placed at 1.5 cm depth of solid water phantom at a distance of 100 cm from the source as 100 MUs were delivered in a 10 x 10 cm^2 beam field. When the irradiation was repeated using 2.5 cm x 32 cm field size and source to chamber distance of 110 cm to replicated the irradiation condition of the NPS measurement, the chamber collected charge reading was 1.43 for 100 MUs. Therefore, the delivered dose in the geometry of NPS measurements was 79.44 cGy according to equation (3.18)

$$D = 100cGy\frac{1.43}{1.80} = 79.44cGy.$$

The number of radiation pulses in 100 MUs delivery was found to be 2426 providing a dose rate per pulse in NPS measurement of $\dot{D} = 3.275 \times 10^{-2}\, cGy / pulse$.

Then the photon fluence can be calculated by equation (3.17) as

$$\varphi = \frac{\dot{D}}{F} = \frac{3.275 \times 10^{-2} cGy / pulse}{7.51 \times 10^{-8} cGymm^2 / photon} = 4.36 \times 10^5 photon / mm^2.$$

Finally, the DQE(f) can be calculated by equation (3.8). Figure 4.21 shows the DQE(f) of the detector system.

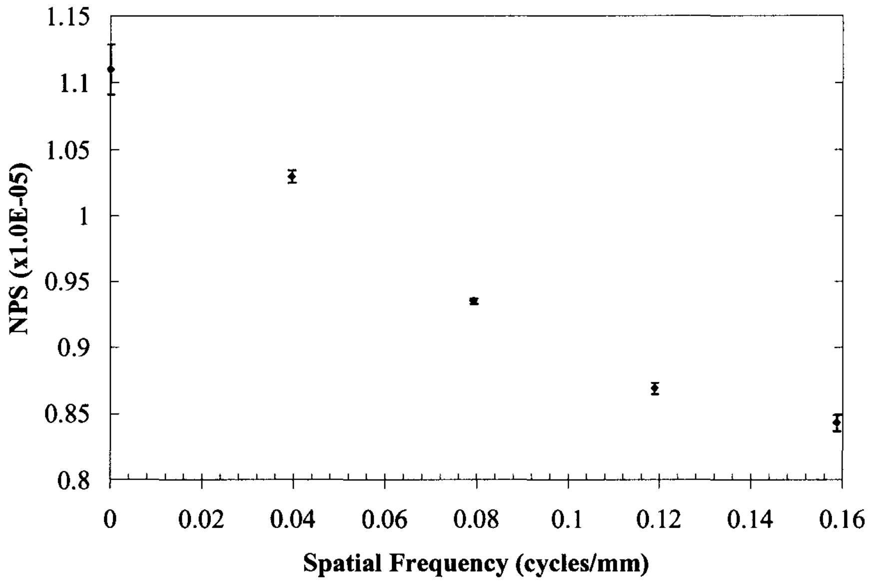

Figure 4.20: The NPS of the 80-element detector system.

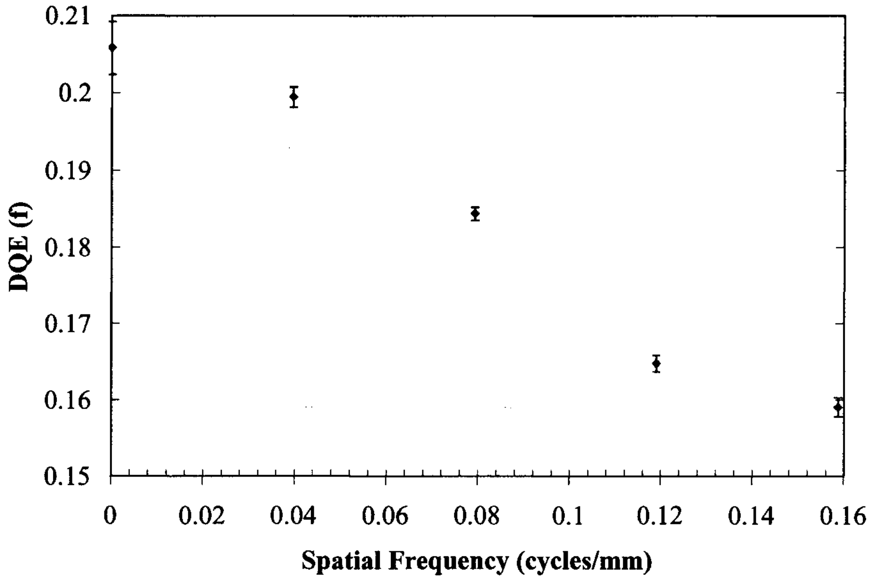

Figure 4.21: The DQE of the 80-element detector system.

From the Figure 4.21, we can see that DQEs of our detector system are 21% and 16% for zero and Nyquist frequencies respectively. This is a very high DQE compared to other imaging systems under MV energy beam. Since the DQE describes the transfer of input SNR to the output of detector at various spatial frequencies, a large DQE results in better performance of the imaging system. Falco et al. [1998] checked the metal-plate/film detectors with different plates and thickness and found the maximum DQE under 10 MV photon beam was 0.37%. El-Mohri group [El-Mohri et al., 2001] found that the maximum DQE for a prototype, indirect detection, and active matrix flat-panel imager under 6 MV photon beam was around 1%. Sawant group [Sawant et al., 2002)] built a new electronic portal imaging device, using a 12.7 mm thick, 20.32 cm diameter, CsI(Tl) scintillator plus 1.5 mm lead, coupled to a liquid nitrogen cooled CCD TV camera. They concluded this imaging system could achieve DQE (0) of 11% under 6 MV photon beam if no loss of optical photons is assumed in the optical chain consisting of mirror and lens system that carried the light produced in the scintillation array to the distant CCD camera. The most port imaging systems recently used in clinic have DQE of only around 1% [Boyer et al., 1992]. Therefore, our imaging system has much higher DQE than other imaging systems. With our high performance detector system, we should obtain MVCT images with more clinically useful low contrast resolution with a low dose.

4.3 Sinogram and Image

Figures 4.22 to 4.24 show the sinograms of a 2 mm thick lead wire, the uniform insert (CTP486) of CATPHAN500 phantom (Phantom Laboratories, Salem, NY) and a specially designed low contrast insert (CTP612) of the CATPHAN500 phantom. To get the projection data for these sinograms, the SDD was set at 110 cm and the source to the rotary stage center distance (SAD) was set at 97.5 cm. The different phantoms were irradiated with a 0.9 x 26 cm^2 field from 6 MV linear accelerator. Alignment of the beam spot, detector center and the motor rotation center was realized by setting a thin lead wire at the rotation center. Projection data points 3082 x 80 were recorded during one rotation.

The stage rotation time was 22.5 s. Then the 3082 projections were averaged into 360 projections per rotation. The basic corrections performed on the sinograms are dark current, zero signal pulses, pulse to pulse fluctuations, and beam hardening.

The sinusoid curve in Figure 4.22 is the measured attenuation of 6 MV beam by the 2 mm lead wire with its values around 0.1. The approximate calculation of the attenuation follows from Eq. 4.2.

$$Ln(I_0/I) = \mu x = \rho(\mu/\rho)_{2MeV}x = 11.36 g/cm^3 \times 0.0453 cm^2/g \times 0.2 cm = 0.103 \tag{4.2}$$

The calculated and measured attenuation values are thus very close. The sinogram of the uniform insert of CATPHAN 500 phantom, as shown in Figure 4.23, is exactly as we expect it. For the low contrast insert of the CATPHAN500 phantom, the sinusoid curve in its sinogram is visible, as shown in the Figure 4.24. All these show that our detector system can measure the phantom attenuation accurately.

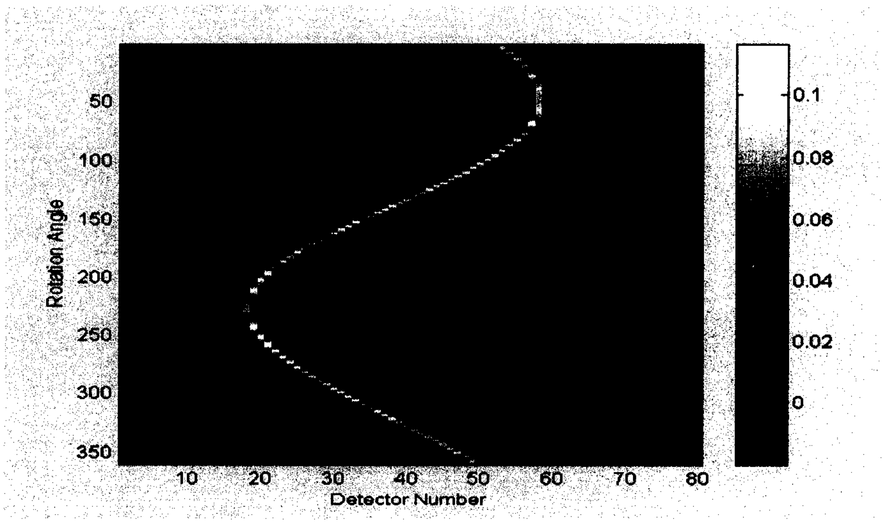

Figure 4.22: Sinogram of a 2 mm thick lead wire. At each of the 360 angular positions (vertical axis) of the rotary stage, the attenuation data measured by 80-elements in the fan-beam is shown along the horizontal lines. SAD = 97.5 cm, SDD = 110 cm, Rotation time = 22.5 s.

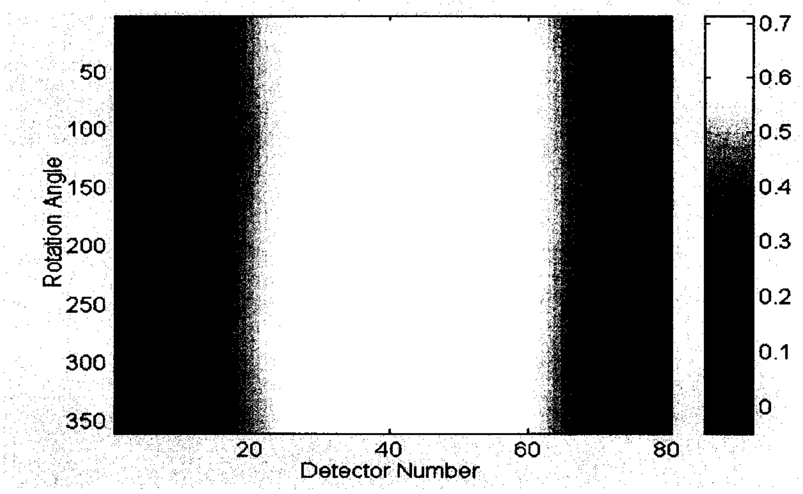

Figure 4.23: Sinogram of the uniform CATPHAN 500 phantom insert with 15 cm diameter. At each of the 360 angular positions (vertical axis) of the rotary stage, the attenuation data measured by 80-elements in the fan-beam is shown along the horizontal lines. SAD = 97.5 cm, SDD = 110cm, Rotation time = 22.5 s.

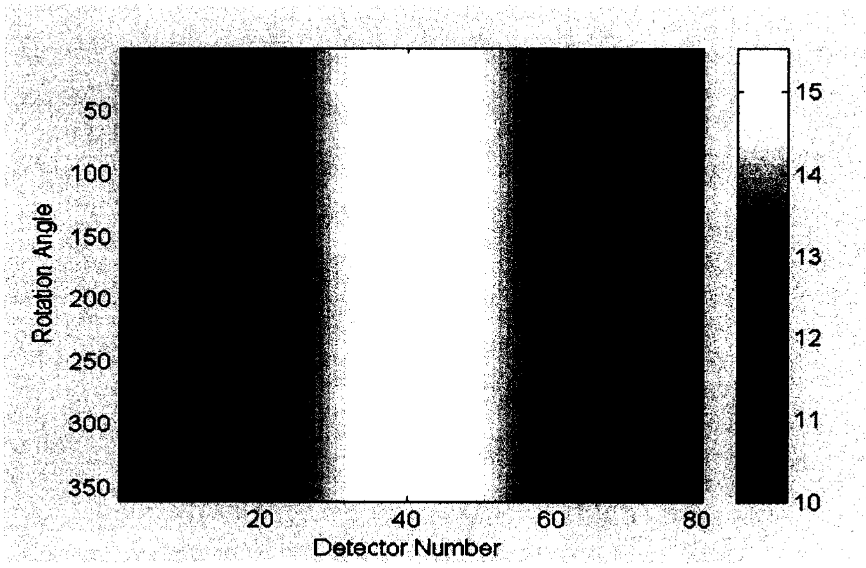

Figure 4.24: Sinogram of the special CATPHAN 500 insert of 15 cm diameter with low contrast levels of 1.5%, 2.5% and 3%. At each of the 360 angular positions (vertical axis) of the rotary stage, the attenuation data measured by 80-elements in the fan-beam is shown along the horizontal lines. SAD = 97.5 cm, SDD = 110 cm, Rotation time = 22.5 s.

Figure 4.25 is the reconstructed image of the low contrast insert of the CATPHAN 500 phantom. The image was reconstructed by the standard filtered backprojection method. The fan beam data was rebinned into parallel beam, and corrected for the non-uniform spacing among the detector channel during this process. Filtered backprojection was performed using Shepp-Logan filter [Shepp and Logan, 1974]. From this image, all the inserts, even those at the lowest contrast of 1.5%, are visible. This further illustrates that our bench-top MVCT scanner works very well. However, the imaging dose is 66.7 cGy which is unintentionally high because of the practical limitations of high dose rate in our linac machine and the slow speed of the rotary stage. The dose calculation was based on the following measurements. As the treatment beam is calibrated to deliver 1 cGy at a depth of d_{max} = 1.5 cm in water for a 10 x 10 cm^2 field size when the chamber is located at 100 cm from the source. Therefore, a pinpoint chamber was placed at a depth of d_{max} = 1.5 cm in a solid water phantom at a distance of 100 cm from the source. The collected charge by the chamber was recorded as x_0 = 1.8 nC by the electronic meter when 100 MUs were delivered in a 10 x 10 cm^2 field. Then the irradiation was repeated using 0.9 cm x 26 cm field size and source to chamber distance of 97.5 cm with 7.5 cm solid water phantom to replicate the irradiation condition of the imaging experiments. The charge reading of x = 1.28 nC was obtained from the chamber for 100 MUs. Therefore, according to Equation (2.18) the dose delivered at center of phantom was calculated as.

$$D = 100cGy\frac{x}{x_0} = 71.1cGy \tag{4.3}$$

However, to acquire one image, the required time is 22.5 second and the linac dose rate was 250 MU per minute. This means that the required monitor unit for one image was

$$250\frac{MU}{\min} \times 22.5s \times \frac{\min}{60s} = 93.75MU \qquad (4.4).$$

Therefore, the corresponding dose for one image was

$$\frac{93.75MU}{100MU} \times 71.1cGy = 66.7cGy \qquad (4.5).$$

The image shown in Figure 4.25 was reconstructed by using only one-eighth of total number of pulses, thus, it uses a dose of only 8 cGy. We are trying to reduce the dose used for an image in 6 MV beam. However, our lab has obtained a 2 cGy image in a Theratron 780E Co^{60} beam in which all the low inserts are also visible by this same bench-top MVCT scanner, as shown in Figure 4.26.

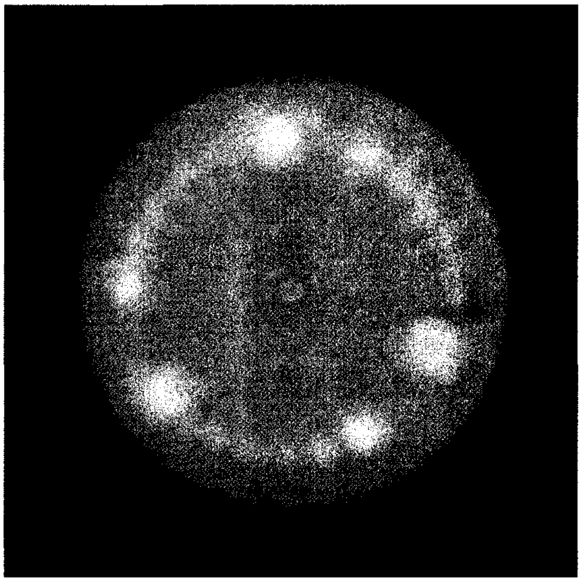

Figure 4.25: The reconstructed image of the special low contrast insert of CATPHAN500 (3.7 cm thick, 15 cm diameter) containing inserts at 3%, 2.5% and 1.5% contrast levels. Each contrast level has 7 cylinders of 20, 15, 8, 7, 6, 5, 4 mm diameters. Central cylinder of 4 mm diameter is at 1.5% contrast level. Estimated dose for this image is about 8 cGy (This image was reconstructed by T. Monajemi).

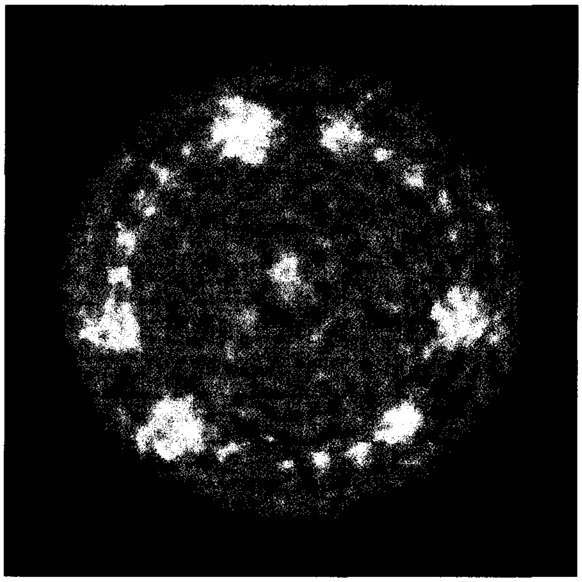

Figure 4.26: The reconstructed image of the same insert as in Figure 3.25 in a Theratron 780E Co^{60} beam. The dose for this image is about 2 cGy (This image was offered by T. Monajemi).

References

Boyer A. L., Antonuk L, Frenster A, van Herk M., Meertens H., Munro P., Reinstein L. E., and Wong J., " A review of electronic portal imaging devices (EPIDs)," *Med. Phys.* 19: 1-16 (1992).

Cunningham I. A., *Applied Linear-Systems Theory*, Chapter 2, Handbook of Medical Imaging Vol. 1, edited by Van Metter R. L. (SPIE Publications 2000).

El-Mohri Y., Jee K., Antonuk L. E., Maolinbay M., and Zhao Q., "Determination of the detective quantum efficiency of a prototype, megavoltage indirect detection, active matrix flat-panel imager," *Med. Phys.* 28: 2538-2540 (2001).

Falco T. and Fallone B. G., "Characteristics of metal-plate/film detectors at therapy energies. II. detective quantum efficiency," *Med. Phys.* 25: 2463-2468 (1998).

Lachaine M., Fourkal E., Fallone B. G., "Detective quantum efficiency of a direct-detection active matrix flat panel imager at megavoltage energies", *Med. Phys.* 28: 1364-1372 (2001).

Lewis D. G., Swindell W., Morton E.J., Evans P.M., and Xiao Z.R., " A megavoltage CT scanner for radiotherapy verification," *Phys. Med. Biol.* 37: 1985-1999 (1992).

Monajemi T. T., Steciw S., Fallone B. G., and Rathee S., "Modeling scintillator-photodiodes as detectors for megavoltage CT," *Med. Phy.* 31: 1225-1234 (2004).

Sawant A., Zeman H., Samant S., Lovhoiden G., Weinberg B., and Dibianca F., "Theoretical analysis and experimental evaluation of a CsI (TI) based electronic portal imaging system," *Med. Phys.* 29: 1042-1053 (2002).

Chapter 5: Conclusions

A detector system based on the previously studied 8-element array of $CdWO_4$ scintillation crystals and photodiodes was extended into a larger array to be utilized in a bench-top MVCT scanner. The various sub-systems including the detector board, data acquisition timing control, data multiplexer unit, and motor control were designed, fabricated and tested. The experimental system was then used to test the basic characteristics of the detector and to collect fan-beam data for a preliminary investigation of the MVCT capability of the detector. The detector's response with respect to dose rate was found to be linear. A small amount of spectral hardening was observed in the attenuation measurements of a 6 MV beam through solid water. This result was indicated by a small, yet significant, second order coefficient when a second order polynomial was fit to the data. The coefficients derived from the data were successfully used to correct the fan-beam projection data for the spectral hardening effect. The two most important results regarding the detector's characteristics are the large DQE at 21% in a 6 MV beam and the fact that the detector's MTF is largely dominated by the detector pitch (3.15 mm). The effect of the detector's aperture on the MTF was studied by measuring the pre-sampled MTF. The large DQE of the detector signifies that a larger than previously reported fraction of incident MV photon fluence on the detector contributes to forming the CT image. This major improvement was indicated by the fundamental properties of $CdWO_4$ scintillation crystal, which have now been realized experimentally in this project. A MTF limited mainly by the detector's aperture suggests that reducing the detector's aperture will have a significant impact on the spatial resolution in CT images and that the Compton scattering within the detector array may have an insignificant impact on the image quality.

The ability of the experimental system to collect the fan-beam sinogram data has been clearly demonstrated. A companion project has been investigating the image quality of this bench-top MVCT in more detail. For this project, a general-purpose data processing method has been designed to correct the fan-beam sinogram data for various effects. These effects include the pulse-to-pulse fluctuations in the beam output of the linear accelerator, the spectral hardening effect, the distinctly different LSF of the detector elements at the ends of each of the ten 8-element blocks and the non-uniform spacing between the detector elements. Also included in the companion project is the method of image reconstruction using the corrected sinogram data. This thesis has included the two images reconstructed using this approach. The most important result is that a contrast level of 1.5% can be visualized using a radiation dose of 2 cGy in the Co^{60} beam. The radiation dose in the 6 MV beam was unintentionally large since neither a reduction in the dose rate per pulse nor the increase in the rotation speed of the precision rotary stage is practical.

There are several future issues regarding MVCT that will be investigated in the companion projects. It has been known that the radiation hardness of the photodiode may limit the life-time of these detectors. However, there has been little experimental work that conclusively demonstrates the effect of radiation damage on the sensitivity of the scintillation-photodiode combination. This is more important for MVCT since a large dose will generally be deposited in the photodiode array because a thick enough scintillation to absorb the entire radiation incident on the detector is quite impractical and hugely expensive. The companion projects will also be theoretically investigating the effect of detector pitch and beam divergence on the MTF within the projection data using a realistic focal spot size and object to detector magnification. These projects will also investigate the use of $CdWO_4$ and photodiodes for cone beam MVCT. In this respect, the photodiode arrays that are tile-able in two dimensions have been recently developed by using back-illumination technology. Therefore, two-dimensional crystal arrays will be formed in contact with new photodiode arrays. These arrays can be mounted such that the entire two-dimensional detector is focussed on the source such that the effect of beam divergence in the thick scintillation crystals is reduced. Therefore, the preliminary investigations that are performed in this project open the door for beneficial future work in fan-beam and cone-beam MVCT and predict a real possibility of a clinically useful system with a small dose of radiation.

Bibliography

Attix F. H., *Introduction to radiological physics and radiation dosimetry*, (John Wiley & Sons, New York, 1986).

Azevedo S, Martz HE and Schneberk DJ, "Potential of computed tomography for inspection of aircraft components," *Nondestructive Inspection of aging aircraft* (san Diego, CA) Ed Valley M, Del Grande N and Kobayashi A (SPIE—The International Society for Optical Engineering), 47-57(1993).

Barret H. and Swindell W., *Radiological Imaging: The Theory of Image Formation, Detection, and Processing* , (Academic Press, 1981).

Barret H. H., Gordon S.K., and Hershel R.S.," Statistical Limitations in Transaxial tomography," *Comput. Biol. Med.* 6: 307-323 (1976).

Berndt A. G., "A Fourth Generation 192IR Source-Based CT scanner for Brachytherapy", Ph.D. thesis, University of Manitoba (2002).

Blasse G. and Grabmaier B.C., *Luminescent Materials* (Springer, Berlin, 1994)

Boyer A. L., Antonuk L., Frenster A., van Herk M., Meertens H., Munro P., Reinstein L. E., and Wong J.,“ A review of electronic portal imaging devices (EPIDs)," *Med. Phys.* 19: 1-16 (1992).

Brahme A., Lind B., and Nafstadius P., "Radiotherapeutic computed tomography with scanned photon beams," *Int. J. Radiation Oncology Biol. Phys.* 13: 95-101 (1987).

Bushberg J. T., Seibert J. A., Leidholdt E. M., and Boone J. M., *The Essential Physics of Medical Imaging*, (Lippincott Williams & Wilkins, Philadelphia, 2002).

Cunningham I. A., *Applied Linear-Systems Theory*, Chapter 2, Handbook of Medical Imaging Vol. 1, edited by R.L. Van Metter (SPIE Publications 2000).

Dastarac D., "Industrial computed tomography at TOMO ADOUR: control and digitizing," *DGZfP Proceeding BB 67-CD*, Poster 9, 193-201 (1999).

Derenzo, S. and Moses W. W., " Experimental efforts and results in finding new heavy scintillators", Proceedings of the CRYSTAL 2000 International Workshop on Heavy Scintillators for Scientific and Industrial Applications, Chamonix, France, 125-135(1992).

Duclos S. J., "Scintillator phosphors for medical imaging," *The Electrochemical Society Interface*, 34-38 (1998).

El-Mohri Y., Jee K., Antonuk L. E., Maolinbay M., and Zhao Q., "Determination of the detective quantum efficiency of a prototype, megavoltage indirect detection, active matrix flat-panel imager," *Med. Phys.* 28: 2538-2540 (2001).

Falco T. and Fallone B. G., "Characteristics of metal-plate/film detectors at therapy energies. II. detective quantum efficiency," *Med. Phys.* 25: 2463-2468 (1998).

Farukhi M. R., "Recent developments in scintillation detectors for X-ray CT and positron CT applications," *IEEE. Trans. Nucl. Sci.* NS-29: 1237-1249 (1982).

Feldkamp L.A., Davis L.C., and Kress J.W., "Practical cone-beam algorithm," *J. Opt. Soc. Amer*, 1: 612-619 (1984).

Flisch A., Wirth J., Zanini R., Breitenstein M., Rudin A., Wendt F., Mnich F., and Golz R., "Industrial computed tomography in reverse engineering applications," *DGZfP-Proceeding BB 67-CD*, Paper 8, 1-9(1999).

Ford E. C., Chang J., Mueller K., Sindhu K., Todor D., Mageras G., Yorke E., Ling C. C., and Amols H., " Cone-beam CT with megavoltage beams and an amorphous silicon electronic portal imaging device: potential for verification of radiotherapy of lung cancer," *Med. Phys.* 29: 2913-2924 (2002).

Groh B. A., Siewerdsen J. H., Drake D. G., Wong J. W., and Jaffray D. A., " A performance comparison of flat-panel imager-based MV and kV cone-beam CT," *Med. Phys.* 29: 967-975 (2002).

Groh B. A., Siewerdsen J. H., Drake D. G., Wong J. W., and Jaffray D. A., " A performance comparison of flat-panel imager-based MV and kV cone-beam CT," *Med. Phys.* 29: 967-975 (2002).

Guan H. and Zhu Y., "Feasibility of megavoltage portal CT using an electronic portal imaging device (EPID) and a multi-level scheme algebraic reconstruction technique (MLS-ART)," *Phys. Med. Biol.* 43:2925-2937 (1998).

Habermehl A. and Ridder H.-W., "Gamma-ray tomography in forest and tree sciences," Developments in X-Ray Tomography Ed Bonse U (Proceedings of SPIE vol.3149. SPIE—The International Society for Optical Engineering), Bellingham, Washington, p234-244 (1997).

Hesse BM, Spies L and Groh BA, "Tomotherapeutic portal imaging for radiation treatment verification," *Phys. Med. Biol.* 43:3607-3616 (1998).

Jaffray D. A., Siewerdsen J. H., Wong J. W., and Martinez A. A., "Flat panel cone-beam computed tomography for image guided radiation therapy," *Int. J. Radiation Oncology Biol. Phys.* 53: 1337-1349 (2002).

Johns H. E. and Cunningham J.R., *The Physics of Radiology*, 4th ed. (Thomas, Springfield, IL, 1983).

Kapatoes J. M., Olivera G. H., Balog J. P., Keller H., Reckwerdt P. J., and Mackie T. R., "On the accuracy and effectiveness of dose reconstruction for tomotherapy," *Phys. Med. Biol.* 46: 943-966 (2001).

Kearfott K. J. and Murty K. N., "A high spatial resolution computed electro-optic radiation detector array," *Health Physics* 58: 99-105 (1990).

Khan F., The Physics of Radiation Therapy, 2nd ed. (Williams & Wilkins, Baltimore, 1994).

Kinolch D. R., Novak W., Raby P., and Toepke I., "New developments in Cadmium Tungstate", *IEEE Trans. Nucl. Sci.*, 41: pp .752-754 (1994).

Krus D. J., Novak W. P., and Perna L., " Precision linear and two-dimensional scintillation crystal arrays for x-ray and gamma ray imaging applications," Presented at *The SPIE International Symposium on Optical Science, Engineering and Instrumentation*, July 18-23, 1999, Hard X-ray, Gamma-Ray and Neutron Detector Physics (SPIE Vol. 3768).

LabVIEW User Manual, (National Instruments Corporation, Austin, 2000).

Lachaine M., Fourkal E., and Fallone B. G., "Detective quantum efficiency of a direct-detection active matrix flat panel imager at megavoltage energies", *Med. Phys.* 28: 1364-1372 (2001).

Lewis D. G., Swindell W., Morton E.J., Evans P.M., and Xiao Z.R., " A megavoltage CT scanner for radiotherapy verification," *Phys. Med. Biol.* 37: 1985-1999 (1992).

Losano F., Marinsek G., Merlo A.M., and Ricci M., "Computed tomography in the automotive field--Development of a new engine head case study," *DGZfP Proceedings BB 67-CD*, Paper 10, 65-73 (1999).

Mackie T.R., Kapatoes J., Ruchala K., Lu W., Wu C., Olivera G., Forrest L., Tome W., Welsh J., Jeraj R., Harari P., Reckwerdt P., Paliwal B., Ritter M., Keller H., Fowler J., and Mehta M., "Image guidance for precise conformal radiotherapy," *Int. J. Radiation Oncology Biol. Phys.* 56: 89-105 (2003).

Mackie T. R., Holmes T., Swerdloff S., Rockwerdt P., Deasy J. O., Yang J., Paliwal B., and Kinsella T., " Tomotherapy: a new concept for the delivery of dynamic conformal radiotherapy," *Med. Phys.* 20: 1709-1719 (1993).

Midgley S, Millar RM, and Dudson J, "A feasibility study for megavoltage cone beam CT using a commercial EPID," *Phys. Med. Biol.* 43: 155-169 (1998).

Mohan R., "Intensity modulated radiotherapy", in *Teletherapy: Present and Future*, edited by Mackie T. R and Palta J. R. (Advanced Medical Publishing, Madison, WI, 1996), pp.761-793.

Monajemi T. T., Steciw S., Fallone B. G., and Rathee S., "Modeling scintillator-photodiodes as detectors for megavoltage CT," *Med. Phy.* 31: 1225-1234 (2004).

Monajemi T. T., "Modeling scintillator-photodiodes for MVCT," M.Sc. thesis, University of Alberta (2004).

Moron E. J., Swindell W., Lewis D. G., and Evans P. M., "A linear array, scintillation crystal-photodiode detector for megavoltage imaging," *Med. Phys.* 18:681-691 (1990).

Mosleh-Shirazi M.A., Evans P.M., Swindell W., Webb S., and Partidge M., " A cone-beam Megavoltage CT Scanner for Treatment Verification in Conformal Radiotherapy", *Radiotherapy and Oncology*. 48: 319-328 (1998).

Munier B., Casagrande J-M, Koch A., Kaftandjian V., Duvauchelle P., and Babot D., "High resolution digital flat panel detector for NDT," *NDT.net* 7(12): 1-10 (2002).

Munro P., "Portal imaging technology: Past, present, and future," *Semin. Radiat. Oncol.* 5: 115-133 (1995).

Nakagawa K., Aoki Y., Akanuma A., Onogi Y., Terahara A., Sakata K., Muta N., Sasaki Y., Kawakami H., and Hanakawa K., "Real-time beam monitoring in dynamic conformation therapy," *Int. J. Radiation Oncology Biol. Phys.* 30: 1233-1238 (1994).

Persson S and Ostman E, "Use of computed tomography in nondestructive testing of polymeric materials," *Applied Optics* 24:4095-4104 (1985).

Rizzoni G., *Principles and Applications of Electrical Engineering,* 2rd ed. (IRWIN, 1996).

Ruchala K. J., Olivera G. H., Schloesser E. A., and Mackie T. R., " Megavoltage CT on a tomotherapy system," *Phys. Med. Biol.* 44: 2597-2621 (1999).

Sawant A., Zeman H., Samant S., Lovhoiden G., Weinberg B., and Dibianca F., "Theoretical analysis and experimental evaluation of a CsI(TI) based electronic portal imaging system," *Med. Phys.* 29: 1042-1053 (2002).

Seppi J., Munro P., Johnsen S. W., Shapiro G., Tognina C., Jones D., Pavkovich J., Webb C., Mollov I., Partain L. D., and Colbeth R. C., "Megavoltage cone-beam computed tomography using a high-efficiency image receptor," *Int. J. Radiation Oncology Biol. Phys.* 55: 793-803 (2003).

Shalev S., "Megavoltage portal imaging", in *Teletherapy: Present and Future*, edited by Mackie T. R and Palta J. R. (Advanced Medical Publishing, Madison, WI, 1996), pp.445-469.

Shepp L. A. and Logan, B. F., "The Fourier reconstruction of a head section," *IEEE Trans.Nucl.Sci.,* 21:21-43 (1974).

Simpson R. G., Chen C. T., Grubbs E. A, and Swindell W., "A 4-MV CT scanner for radiation therapy: the prototype system," *Med. Phys.* 9: 574-579 (1982).

Swindell W., Simpson R. G., and Oleson J. R., "Computed Tomography with a linear accelerator with radiotherapy applications," *Med. Phys.* 10: 416:420 (1983).

Van Dyk J., "Radiation oncology overview", in *The Modern Technology of Radiation Oncology*, edited by Van Dyk J. (Medical Physics Publishing, Madison, WI, 1999), pp.1-19.

van Eijk C. W. E., " Inorganic scintillators in medical imaging," *Phys. Med. Biol.* 47: R85-R106 (2002).

Vittori F., de Notaristefani F., Malatesta T., and Puertolas D., "A study on light collection of small scintillating crystals," *Nuclear Instuments and Methods in Physics Research, Section A* 452: 245-251 (2000).

Williams M. B., Mangiafico P. A., and Simoni P. U., "Noise power spectra of images from digital mammography detectors", *Med.Phys.*26: 1279-1293(1999).

www.bicron.com	[Manufacturer of crystal used in this study]
www.hamamatsu.com	[Manufacturer of the photodiodes used in this study]